Studies of $\eta' p$ photoproduction at the BGOOD experiment

Dissertation
zur
Erlangung des Doktorgrades (Dr. rer. nat.)
der
Mathematisch-Naturwissenschaftlichen Fakultät
der
Rheinischen Friedrich-Wilhelms-Universität Bonn

von
Stefan Alef
aus
Bonn

Bonn, 21.06.2021

Abstract

Recent beam asymmetry measurements indicate a narrow resonance hidden directly at threshold in η' photoproduction off the proton. To date these results have not been confirmed. The BGOOD experiment at the Electron-Stretcher-Anlage (ELSA) at the University of Bonn offers a unique setup for the analysis of the $\gamma p \to \eta' p$ reaction, consisting of a high resolution forward spectrometer and a central calorimeter. At threshold the whole range of polar angles in the center-of-mass frame is boosted into a narrow forward cone in the lab frame. Thus the recoil proton can be detected in the forward spectrometer, which offers high momentum and angular precision. η' decay products are detected in the central calorimeter.

The basis of the analysis in this thesis is the proton reconstruction in the forward direction, i.e. in the forward spectrometer. In principle, this fully determines the reaction kinematics, given the two-body final state and the known initial state. Nevertheless, the reaction was also reconstructed with increasing levels of exclusiveness, using in part the $\eta' \to \pi^0 \pi^0 \eta$ and, fully exclusive, the $\eta' \to \gamma\gamma$ decay modes. This is important to understand possible backgrounds in the inclusive reconstruction methods.

For the investigated reconstruction methods, the necessary amount of data is estimated to achieve a statistical precision sufficient to detect the expected impact of the hypothetical narrow resonance also in the differential cross section of the $\gamma p \to \eta' p$ reaction and discriminate between descriptions with and without said resonance. Based on the findings of this thesis, recommendations for future analyses and beam times are made.

Contents

Introduction

Humanity has always sought to understand the structure of matter and what rules govern it. Already in ancient Greece Leukipp and his student Demokrit had the idea that matter is not continuous but rather made up from indivisible smallest parts. They called those smallest parts "átomos", meaning "the indivisible" in Greek. Materials would be composed of different atoms with different properties giving them their individual characteristics.

Although those ideas took a backseat during the Middle Ages, they resurfaced in the late 18th century due to advances in chemistry. John Dalton realized that the amount of oxygen for different oxides of the same material always followed integer ratios. He proposed that chemical compounds are made up of a mixture of unique atoms, that can not be destroyed by chemical means [1].

About one hundred years later in the early 20th century, Ernest Rutherford conducted his famous "Rutherford experiment", where he bombarded a thin gold foil with α-particles and discovered that, unlike expected, most particles passed the foil without any deflection, while a small portion of the α-particles was scattered backwards. He concluded that the atom must consist of a small positively charged core surrounded by electrons [2].

In 1919 he observed that hydrogen nuclei were being ejected from nitrogen, while the latter was bombarded with α-particles. He reasoned that the nitrogen nucleus must be composed of hydrogen nuclei and that those must be building blocks of the atomic nucleus [3]. He proceeded to call the hydrogen nucleus "proton".

Rutherford further predicted the existence of another neutral particle in the atom. One he considered a combination of proton and electron. This neutral particle, we today know as neutron, was finally discovered by James Chadwick in 1932, when he shot α-radiation on a beryllium target and used the resulting neutral radiation to knock protons out of paraffin. He concluded that this neutral radiation was too energetic to be photons, thus leading to the discovery of neutrons [4].

In the decades following these important initial discoveries, a bevy of other particles was found, among them the muon in 1936 [5], the pion [6] and kaon [7] in 1947, the Delta-resonance in 1952 [8] and the ρ [9] and ω [10] in 1961. It was first believed that there was no order to all these particles but, independently, Murray Gell-Mann [11] and Yuval Ne'eman [12] developed an ordering scheme for the hadrons. According to this hadrons are objects composed of either a quark-antiquark pair (meson) or three quarks (baryon). Gell-Mann called this ordering scheme the Eigthfold-way and it ordered mesons and baryons in SU(3) flavor multiplets, namely singlets, octets and decuplets, shown in figures 1.1 and 1.2. At that time quarks were thought to be purely mathematical objects, but in 1969 they

were finally confirmed to exist in deep-inelastic-scattering experiments at SLAC [13, 14].
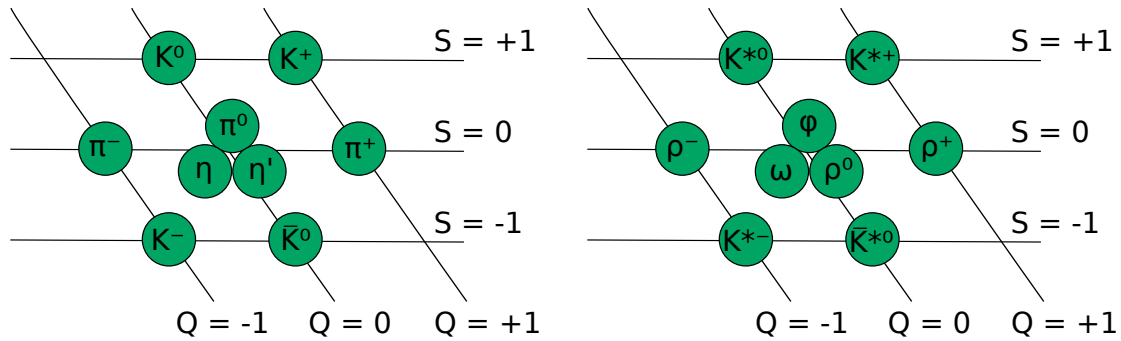

Figure 1.1: Meson SU(3) multiplets. S indicates the strangeness, while Q indicates the charge. The three particles in the center of each multiplet occupy the same spot. Based on [15].
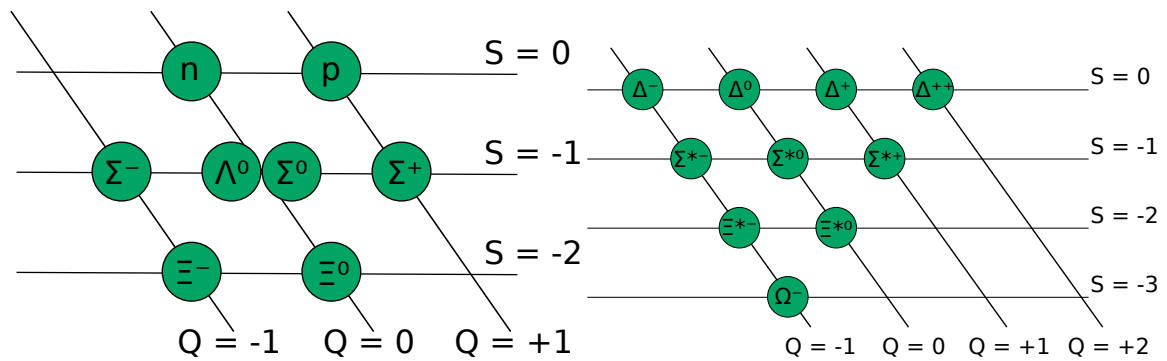

Figure 1.2: Baryon SU(3) multiplets. S indicates the strangeness, while Q indicates the charge. The two particles in the center of the left multiplet occupy the same spot at I_3. Based on [15].

In the following years additional particles were found. Among them gluons in 1979 at DESY [16], weak gauge bosons in 1983 at CERN [17, 18, 19, 20] and finally the Higgs boson in 2012 at CERN [21]. During this time the Standard Model of particle physics was developed. It accurately describes all fundamental forces except gravity and contains all currently known fundamental particles. Figure 1.3 shows an overview of the particles in the standard model.

The standard model is a great success in describing a plethora of subatomic phenomena. The Higgs particle is believed to lend mass to the matter particles and gauge bosons of the standard model. In addition to the bare quark masses, a significant, in the uds-sector the dominating fraction of the mass of hadrons, is not associated with the Higgs mechanism, but with the energy of the gluonic field inside the composite particle. The exact mechanism of this and the associated structure of such composite particles is still under investigation.

Using the quark model mentioned above, the hadronic groundstates can be well described and ordered, as shown in figures 1.1 and 1.2. Nevertheless, there are known problems concerning the excitation of those states. Those include the number of states at higher energies or the parity ordering of the lowest lying states. Since a long time this issues were speculated to hint at and be resolved by multi-quark structures beyond the simple three constituent quark model.

Since the recent discoveries in the c-quark sector [23, 24], candidates for tetra- and pentaquark systems
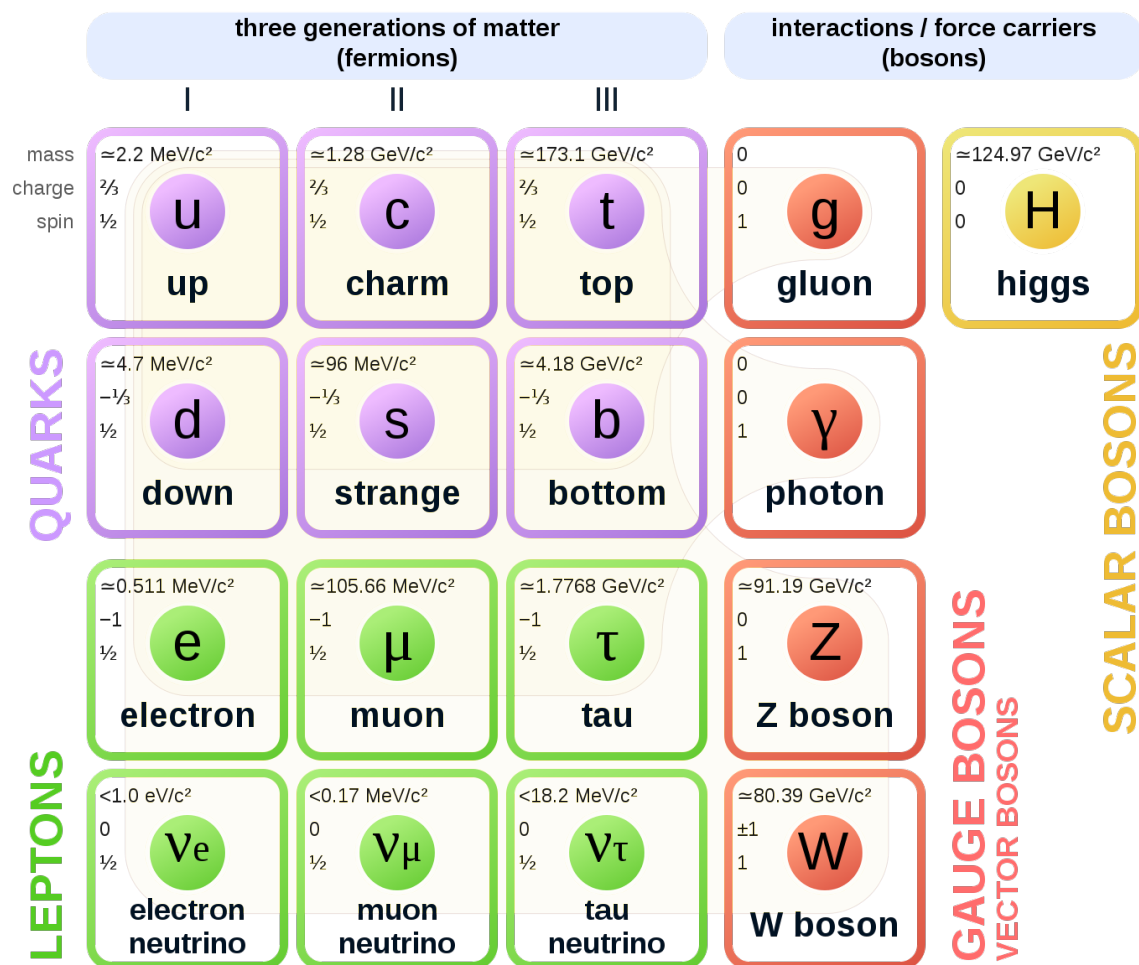
Figure 1.3: Particles in the standard model. The yellow boxes indicate which gauge bosons interact with which quarks/leptons. [22]

are known, likely realized as meson-meson or meson-baryon molecule like states. Also, in the light quark sector the $\Lambda(1405)$ is a candidate for such a molecule-like state. This is supported by lattice QCD results that show the $\Lambda(1405)$ to be predominantly a kaon nucleon system for realistic quark masses [25].

Since such unconventional molecule-like systems are expected to be loosely bound, they predominantly should be created at the respective 2-particle thresholds, where there is no kinetic energy between the particles. In meson photoproduction, resonances generally exhibit themselves in cross sections and through interference with other states, also in polarisation observables like the beam asymmetry Σ. Recently, an enigmatic signal has been reported by the GRAAL collaboration in the beam asymmetry of η' photoproduction [26]. It is located directly at threshold, exhibits a particularly narrow width and could be a candidate for such an unconventional system. The GRAAL findings will be explained in more detail in chapter 2.

So far this signal has not yet been confirmed by any other experiment. Due to its unique combination of central calorimeter and forward spectrometer, BGOOD [27] offers this possibility. Therefore this work undertakes an exploratory study of $\eta' p$ photoproduction directly at threshold. Of particular interest is the cross section at extreme forward and backward angles, because this is where the suspected resonance would manifest itself.

The goal is to estimate the statistical accuracy which can be obtained in analyses going in different levels from the entirely inclusive reaction $\gamma p \rightarrow p + X(\eta')$, where no decay products of the η' are determined, to fully exclusive $\gamma p \rightarrow p + \gamma\gamma(\eta')$, where the η' is reconstructed using its 2γ decay. Correlated with this is a significant decrease of statistics, but paired with a gain in signal purity without background contamination. The latter is estimated by comparing with parametrizations of the cross section in well measured angular regions.

Chapter 2 will give an overview of the current status of data on the η', with a special focus on the GRAAL results as well as more details on the scope of this work. This is followed by chapter 3 explaining the experimental setup of the BGOOD experiment and important analysis tools, and chapter 4, where the analysis performed in this work is laid out. In chapter 5 a recommendation on how to proceed on the η' analysis in the future will be given, based on the findings of chapter 4. Chapter 6 concludes this work.

Current status of η' photoproduction

In this chapter the current status regarding knowledge of η' photoproduction will be laid out. At first some general remarks will be made concerning photoproduction and excited baryonic states, followed by an overview over the current state of η' photoproduction. Afterwards a more in-depth look is given at the GRAAL results that are so important to verify as well as the experimental challenges that need to be overcome for the verification.

2.1 Basics of photoproduction and baryonic resonances

During photoproduction off the proton, a real photon hits a proton in the experimental target, which is typically made of liquid hydrogen. An intermediate state may be produced, which decays into a final state baryon and one or more mesons. Alternatively the final state baryon and mesons are produced directly. Figure 2.1 shows the Feynman diagram for $\eta'p$ photoproduction, i.e. $\gamma p \rightarrow \eta'p$.
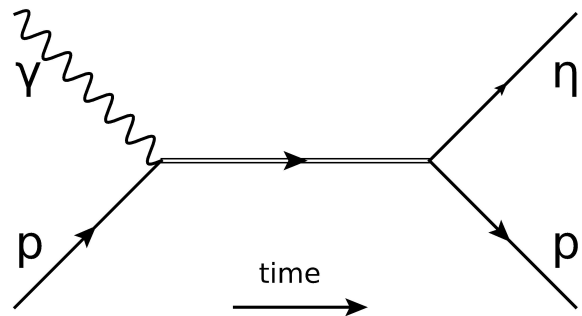
Figure 2.1: Feynman diagram for $\eta'p$ photoproduction. The double line in the middle indicates a possible intermediate state.

The possible intermediate states are baryonic resonances, for example the famous Δ-resonance. These resonances are labeled according to the incoming partial wave $L_{2I,2J}$, e.g. $\Delta(1232)\mathrm{P}_{33}$ or in a newer notation via the spin-parity J^P of the state, e.g. $\Delta(1232)3/2^+$ [15], with the number in brackets indicating the mass of the resonance. They are typically very broad, in the range of tens to hundreds of MeV. As a result the spectra of different resonances overlap significantly and need to be disentangled to gain information about the specific resonances. This is shown in figure 2.2 which shows the total

cross section for $\gamma p \rightarrow \pi^0 p$ as well as the individual resonances contributing.

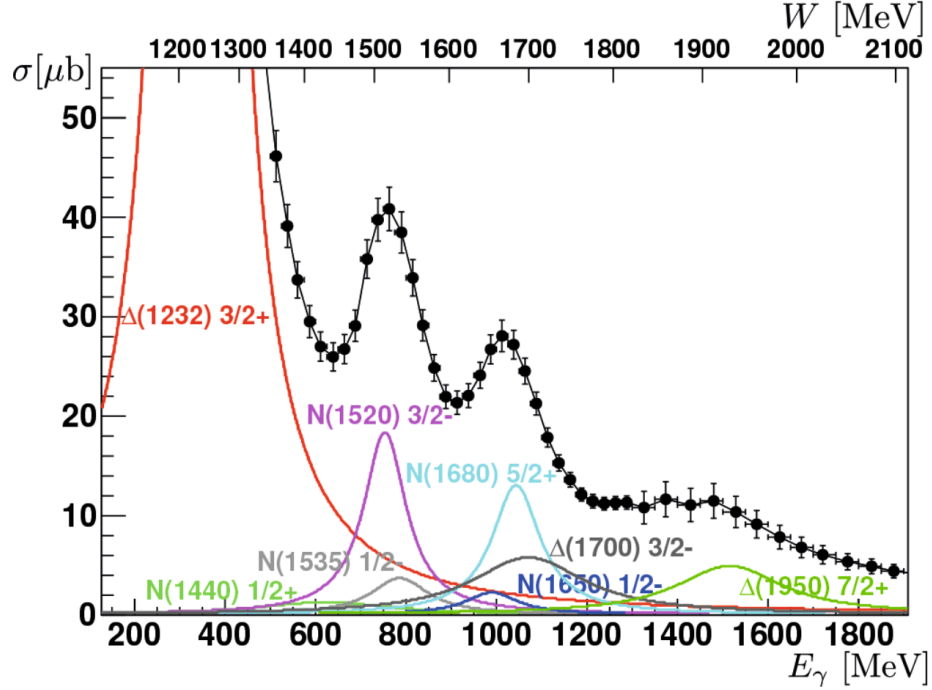Figure 2.2: Resonances contributing to the total $\gamma p \rightarrow \pi^0 p$ cross section [28]. The colored lines are the calculated Breit-Wigner distributions for the respective resonances.

One method of disentangling those states is the partial wave analysis, which splits up the total amplitude of a reaction into different partial waves with different angular momenta, i.e S-, P-, D- etc. waves, corresponding to an angular momentum of 0, 1, 2 etc. and solves the problem using boundary conditions.

2.2 Current data on η' photoproduction

The η' has a mass of (957.78 ± 0.06) MeV with quantum numbers of $J^{PC} = 0^{-+}$ [15]. Its most dominant decay channels can be found in table 2.1.

decay mode	branching ratio / %
$\pi^+\pi^-\eta$	42.5 ± 0.5
$\rho^0\gamma$ including non-resonant $\pi^+\pi^-\gamma$	29.5 ± 0.4
$\pi^0\pi^0\eta$	22.4 ± 0.5
$\omega\gamma$	2.52 ± 0.07
$\gamma\gamma$	2.307 ± 0.033

Table 2.1: Most dominant η' decay modes [15].

The η' is part of the pseudoscalar meson octet that also contains the η and π^0, see figure 1.1. η and η' are different combinations of the same non-physical states η_1 and η_8 [15]. They are related via

$$
\begin{pmatrix} \eta \\ \eta' \end{pmatrix} = \begin{pmatrix} \eta_8 \\ \eta_1 \end{pmatrix} \cdot \begin{pmatrix} \cos\Theta_p & -\sin\Theta_p \\ \sin\Theta_p & \cos\Theta_p \end{pmatrix},
\tag{2.1}
$$

where η_8 and η_1 are described using

$$
\eta_8 = \frac{1}{\sqrt{6}} \cdot \left(u\bar{u} + d\bar{d} - 2s\bar{s} \right),
\tag{2.2}
$$

$$
\eta_1 = \frac{1}{\sqrt{3}} \cdot \left(u\bar{u} + d\bar{d} + s\bar{s} \right).
\tag{2.3}
$$

Θ_p is the mixing angle between the two states with a value of $(-14.1 \pm 2.8)^\circ$ [15].

η' differential cross sections have already been measured by CBELSA/TAPS at ELSA [29], CLAS [30] and Crystal Ball/Taps at MAMI [31] (called A2MAMI from now on). Figure 2.3 shows the results from A2MAMI and CLAS as well as EtaMAID [32] parametrizations based on those two data sets. The beam asymmetry Σ has been measured by CLAS [33] and GRAAL [26], shown in figure Figure 2.4. The CLAS data exhibit a beam asymmetry that is consistent with zero close to threshold ($E_\gamma^{\text{threshold}} = 1\,446\,\text{MeV}$, $W^{\text{threshold}} = 1\,895\,\text{MeV}$). This is expected if there is no interference close to threshold. The GRAAL results are discussed in more detail in section 2.3.

2.3 GRAAL beam asymmetry results

As mentioned in section 2.2 the η' beam asymmetry has already been measured by the GRAAL collaboration. An unexpected nodal structure was observed in the $\Theta_{\eta'}^{\text{CMS}}$ dependency of the beam asymmetry very close to threshold, i.e. it vanishes within $20\,\text{MeV}$ from threshold. Figure 2.4 shows the $\Theta_{\eta'}^{\text{CMS}}$ dependency of the beam asymmetry in the two energy bins where the structure was observed. $\Theta_{\eta'}^{\text{CMS}}$ is the η' polar angle in the center-of-mass frame (CMS).

The observed behavior can be explained by a narrow resonance close to threshold. This is supported by theoretical calculations from the Bonn-Gatchina partial-wave-analysis group [35] and the EtaMAID group [34]. The former included a $D_{13}(1900)$ with a mass of $M_{\eta'p} = (1\,900 \pm 1)\,\text{MeV}$ and a width of $\Gamma_{\eta'p} < 3\,\text{MeV}$ and the latter a $S_{11}(1900)$ with a mass of $M_{\eta'p} = (1\,902.6 \pm 1.0)\,\text{MeV}$ and a width of $\Gamma_{\eta'p} = (2.1 \pm 0.5)\,\text{MeV}$ to much more accurately describe the experimental data. Figures 2.5 and 2.6 show fits to the GRAAL beam asymmetry with and without these resonances. Compared to the typical width of a hadronic resonance, mentioned in section 2.1, these $D_{13}(1900)$ and $S_{11}(1900)$ resonances are unusually small.
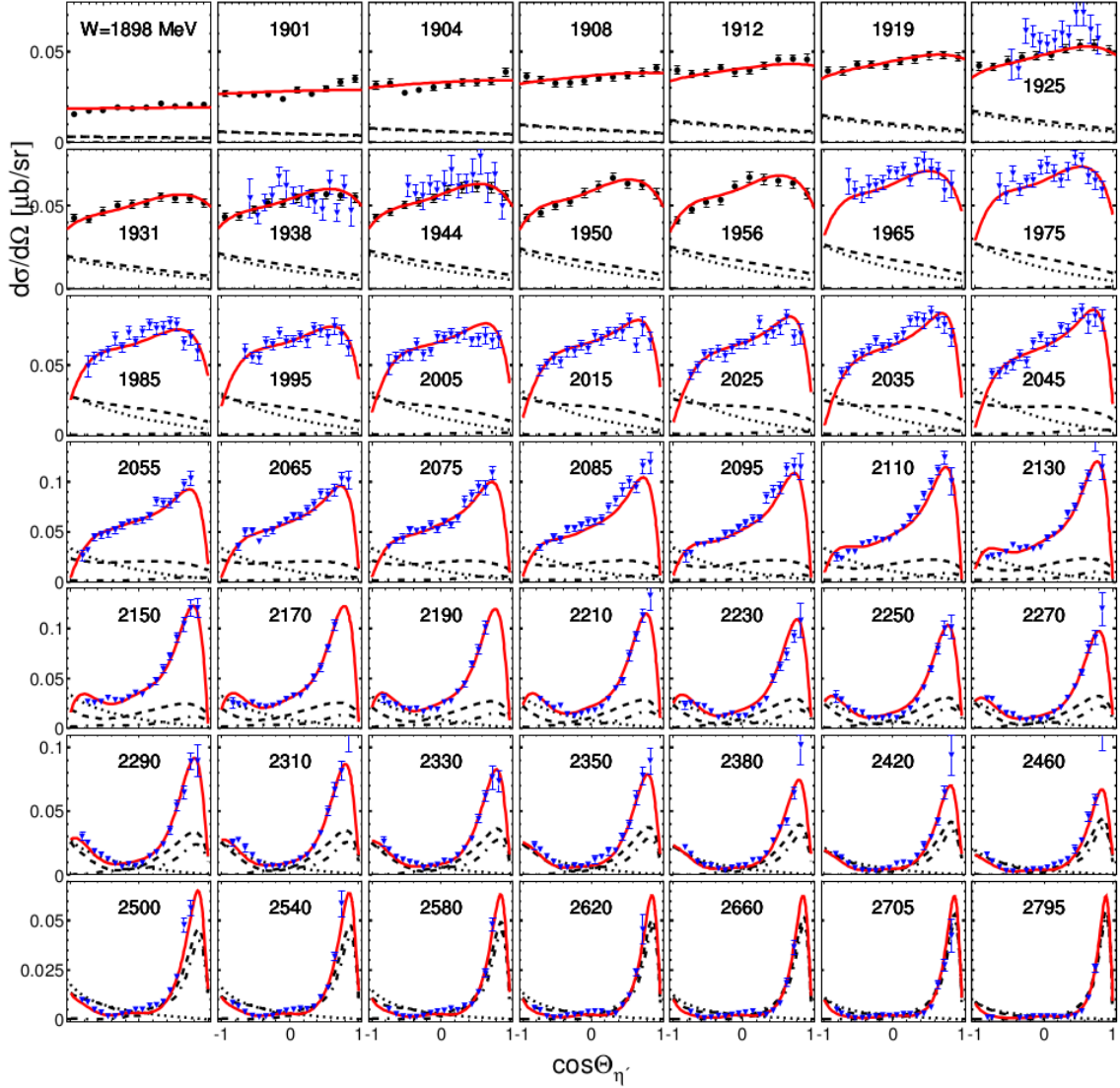
Figure 2.3: Differential cross section results from A2MAMI (black circles) and CLAS (blue triangles) [34]. The solid red lines show the respective EtaMAID parametrizations. The dashed lines are background terms. More details on the parametrizations can be found in the source.

Expanding the beam asymmetry $\Sigma(E_\gamma, \Theta_{\eta'}^{\text{CMS}})$ into partial waves up until F-waves ($L_{\max} = 3$) yields

$$\Sigma = \left(1 - x^2\right) \sum_{k=0}^{4} a_k x^k, \tag{2.4}$$

$$\text{with } x = \cos(\Theta). \tag{2.5}$$

For $k = 1$ this leads to the observed $\sin^2(\Theta) \cdot \cos(\Theta)$ modulation. The corresponding coefficient $a_1 = a_1^{SF} + a_1^{PD} + a_1^{DF}$ consists of interference terms between S-F, P-D and D-F waves [34].
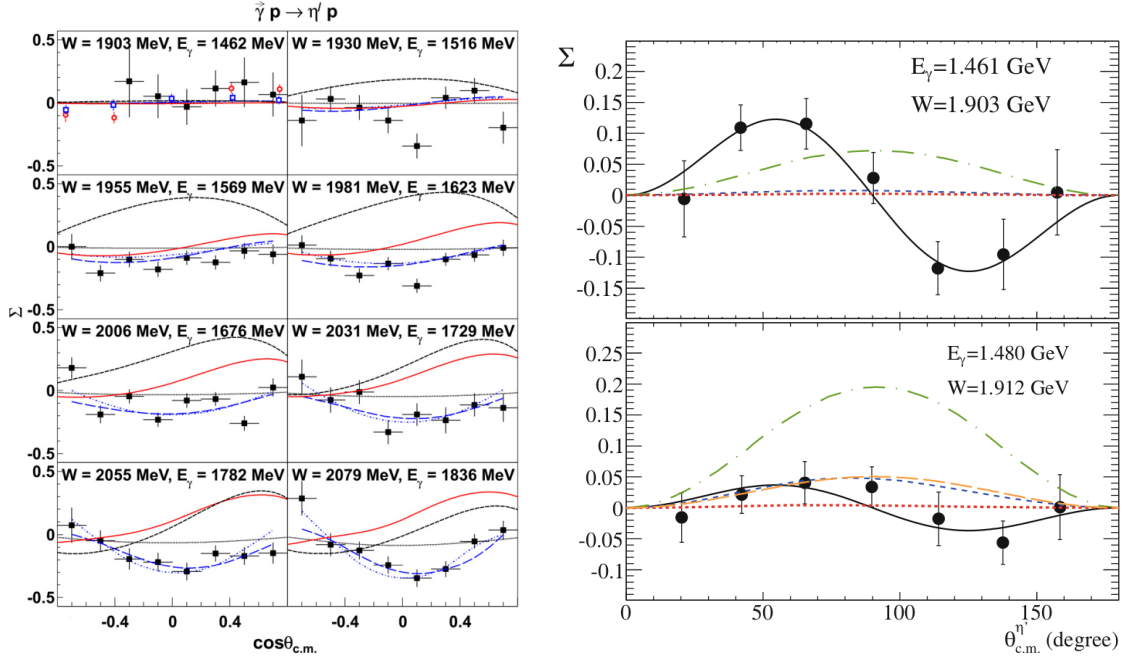
Figure 2.4: Beam asymmetry Σ results from CLAS [33] (left) and GRAAL [26] (right). Left: the GRAAL results are also shown as the open symbols ($E_\gamma = 1.461$ GeV in red and $E_\gamma = 1.480$ GeV in blue). The lines are different predictions, see [33] for more details. Right: the solid black line is a simple $f = a \cdot \sin^2(\Theta) \cdot \cos(\Theta)$ fit while the dotted lines are different theoretical calculations. See [26] and the references therein for full details. Note that there is a slight difference in notation, as $\Theta_{\eta'}^{\mathrm{CMS}}$ is labeled $\Theta_{\mathrm{c.m.}}^{\eta'}$ in [26].
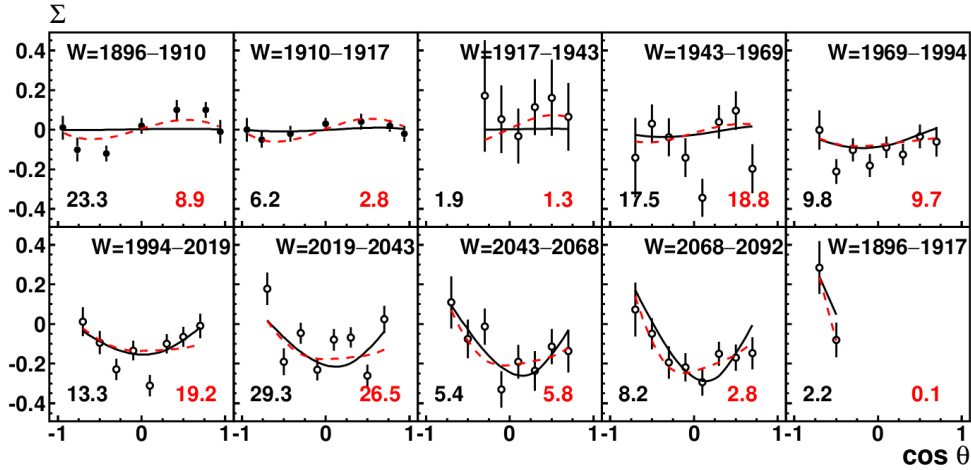

Figure 2.5: Bonn-Gatchina fits to the GRAAL (first two subfigures) and CLAS (last eight subfigures) beam asymmetry with (red dashed line) and without (black solid line) the D_{13} (1900) included in the fit [35]. The numbers at the bottom indicate the χ^2 for the respective fits.
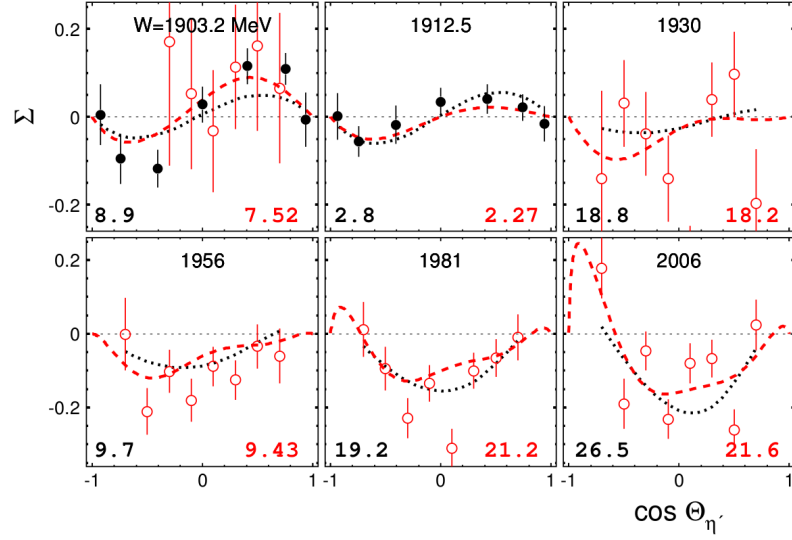
Figure 2.6: EtaMAID fits to the GRAAL (black data points) beam asymmetry [34]. Also shown are the CLAS data (red data points). The red lines are parametrizations including the S_{11} (1900), with the Bonn-Gatchina results shown by the black lines. The numbers at the bottom indicate the χ^2 for the respective fits.

Due to the higher spin states involved this effect is also visible in the differential cross section, especially at the edges of the $\cos(\Theta_{\eta'}^{\text{CMS}})$ distribution. The relation between the polarized cross section and the beam asymmetry is described using

$$\left(\frac{d\sigma}{d\Omega}\right)^{\text{pol}} = \left(\frac{d\sigma}{d\Omega}\right)^{\text{unpol}} \left(1 - P_\gamma(E_\gamma)\Sigma(E_\gamma, \Theta_{\eta'}^{\text{CMS}})\cos(2\phi_{\eta'})\right), \qquad (2.6)$$

where $P_\gamma(E_\gamma)$ is the photon beam polarization, $\Sigma(E_\gamma, \Theta_{\eta'}^{\text{CMS}})$ the beam asymmetry and $\phi_{\eta'}$ the azimuthal angle of the η'. Figures 2.7 and 2.8 show theoretical parametrizations for the differential cross sections from Bonn-Gatchina and EtaMAID, respectively.

2.4 Scope of this work

The BGOOD experiment (explained in more detail in chapter 3) is well suited for the analysis of such a reaction. The proton is expected to go in forward direction due to the Lorentz boost, where the BGOOD experiment offers a good acceptance for charged particles. The decay particles of the η', which are mostly photons, are expected in the central direction, where the BGOOD experiment has a good acceptance for neutral particles.

The goal of this work is to quantitatively investigate how well such an analysis can be performed and how the particular setup of the BGOOD experiment can best be made use of. For this three different decay modes of the η' are tested which show varying degrees of background and statistics. Section 4.1 explains the different modes in more detail. They are evaluated by comparing the resulting differential cross sections to existing theoretical EtaMAID results.

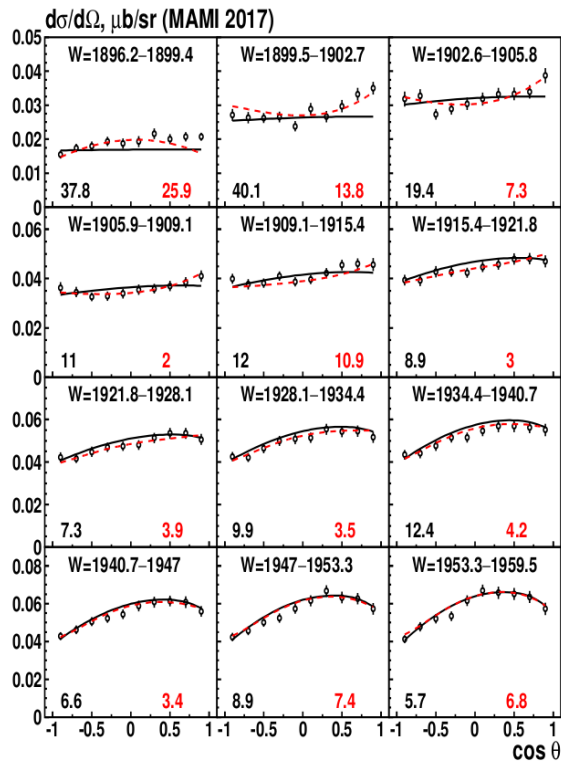Figure 2.7: Bonn-Gatchina fits to the A2MAMI differential cross sections [35]. The red line includes the narrow resonance whereas the black one does not. The numbers at the bottom indicate the χ^2 for the respective fits.
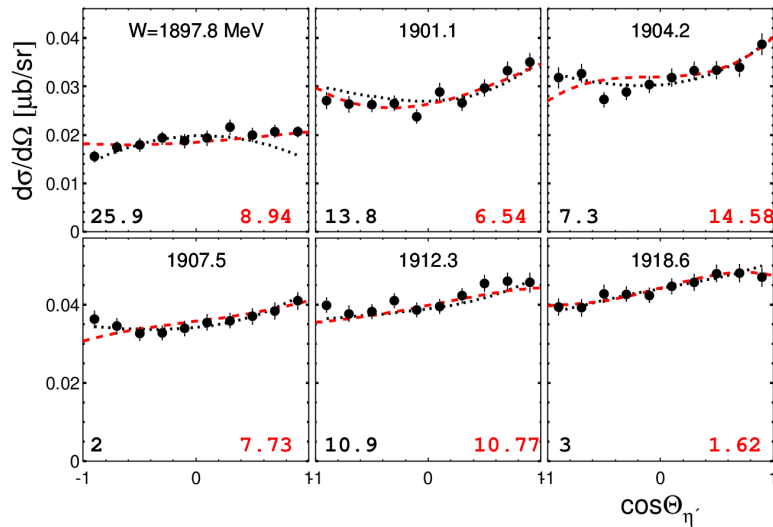

Figure 2.8: EtaMAID fits (red) to the A2MAMI differential cross sections [34]. The black lines are the Bonn-Gatchina fits. The numbers at the bottom indicate the χ^2 for the respective fits.

Based on this better understanding of the experimental possibilities a suggestion will be made on how to proceed with future analysis and data taking.

There are challenges when looking at this channel. First of the cross section is rather low and secondly the decays of the η' are complicated, see table 2.1. Furthermore it will be difficult to achieve the necessary precision in $\cos(\Theta_{\eta'}^{\mathrm{CMS}})$ to see the differences in the cross section between including and not including a narrow resonance. The reason for this difficulty is explained in section 2.5.

2.5 Kinematic focussing

At every threshold in meson photoproduction a peculiar feature occurs: both meson and baryon are produced in a narrow forward cone, since no transverse momentum is available. In the case of η' photoproduction this means that the proton will mostly be detected in a forward direction. Since the η' decays before it can reach any detector, only its decay products are detected. Due to their isotropic decay in the rest frame those are found in the central region of the experiment.

This means that in a spectrum with the number of protons in forward direction per energy the η' shows up as a peak at its threshold and then fades away.

This method leads to high statistics close to threshold. Signal and background can be well separated because the η' is the only reaction experiencing a peaking behavior in this energy region. For higher energies more transverse momentum is available, leading to a wider cone, such that this method quickly looses its value. Nonetheless the energy region, where it works well, covers exactly the region of interest of this work.

Additionally close to threshold all angles in the CMS can be detected in a forward direction. Thus the whole CMS range can be analyzed in this work. Since the large CMS angular region is transformed into a small angular region in the lab frame, small errors in the determination of the lab angle lead to large changes in the recalculated CMS angle. It is therefore necessary to determine the lab angle with a high precision. Due to the impact of the Lorentz boost on the lab angle, the same applies for the energy determination of the initial photon.

Experimental setup and analysis tools

The BGOOD experiment is a fixed target experiment located at the Electron-Stretcher-Anlage ELSA [36] at the physics institute of the University of Bonn. At BGOOD excited mesonic states and mesons are produced via photoproduction. The setup of the BGOOD experiment is ideally suited for the detection of such reactions.

This chapter contains a description of the ELSA facility followed by an in-depth look at the different detectors comprising the BGOOD experiment, followed by a section about analysis tools used in this work.

3.1 The ELSA accelerator

The ELSA accelerator is located at the physics institute of the University of Bonn. The schematics of the facility can be seen in picture 3.1.
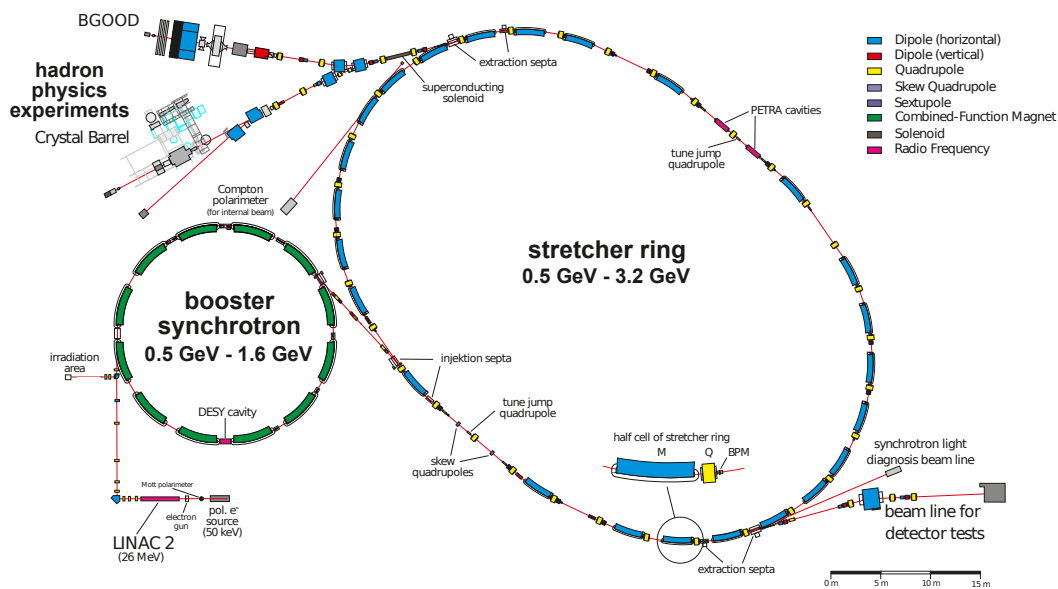

Figure 3.1: The ELSA accelerator facility at the physics institute of the University of Bonn [27].

13

Electrons are either produced using a laser and a Pockels cell (for polarized electrons) or a thermionic gun (for unpolarized electrons) and are subsequently fed into a linear accelerator.

Coming out of the linear accelerator the electrons are fed into the Booster Synchrotron in which they can be accelerated up to 1.6 GeV. They are subsequently injected into the stretcher ring where they reach their final energy of up to 3.5 GeV. The stretcher ring is filled completely using several (usually more than 18) injections of the booster synchrotron, which takes less than 1.5s. This allows for a quasi continuous beam during extraction, even though the electrons are still in separate bunches.

After the stretcher ring has been filled, the electrons are extracted into one of the two hadron physics experiments (BGOOD, Crystal Barrel) or into an area for detector tests. The experiments receive the electron beam for about five seconds before the filling period of the stretcher ring starts again [37].

3.2 The BGOOD experiment

The BGOOD experiment can be divided into three main parts: the tagging system, where real photons are produced via bremsstrahlung of the ELSA electrons and their energy is determined, the central detectors, that are ideally suited for the detection of neutral particles and the forward spectrometer offering a very good momentum resolution and particle identification for charged particles. Figure 3.2 shows the total experimental setup.
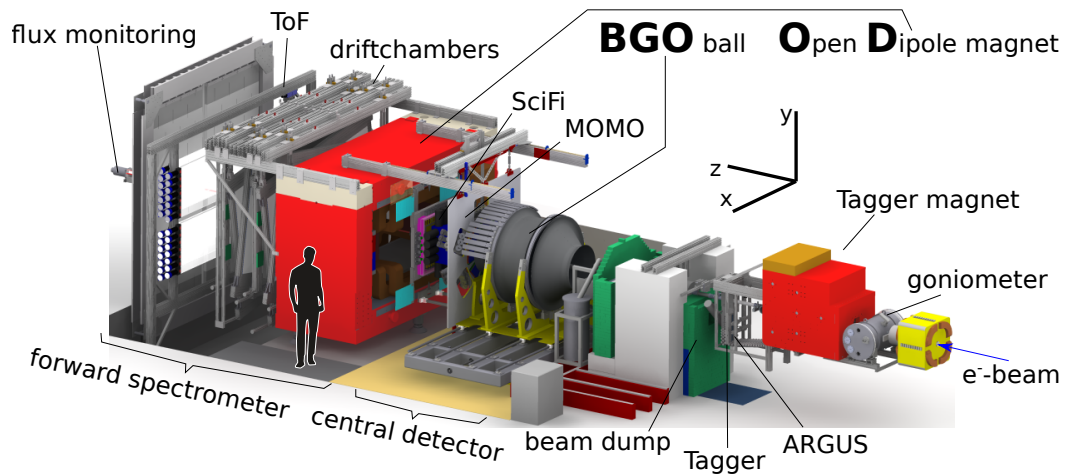

Figure 3.2: Overview over the BGOOD experimental setup [27].

Also shown in figure 3.2 is the x-y-z-coordinate system of the BGOOD experiment. The polar angle Θ is $0°$ for particles going in z-direction (forward) and $180°$ for particles going in negative z-direction (backwards). The azimuthal angle ϕ is $0°$ for particles in the x-z-plane with a positive x-coordinate, $90°$ for particles going in the z-y-plane with a positive y-component etc.

Each part of the experiment will be described in one of the following sections, starting with the tagging system. A more in-depth look into the experiment and its performance can be found in [27].

3.2.1 The tagging system

The tagging system is located at the beginning of the experiment. It is used to convert the incoming ELSA electron beam into a real photon beam via bremsstrahlung and determine the energy of the

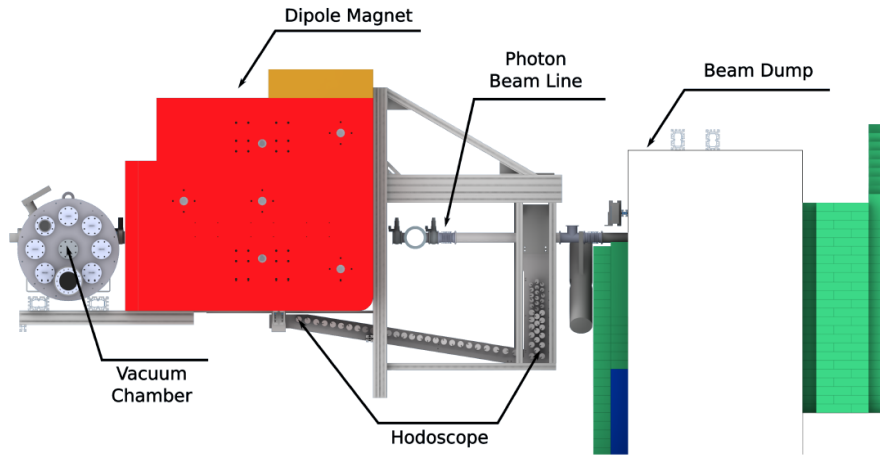produced photons. The tagging system can be seen in figure 3.3.

Figure 3.3: Sideview of the BGOOD tagging system [27]. The electron beam is coming from the left. The goniometer is located inside the vacuum chamber.

It consists of the goniometer which holds different radiators for the production of electrons via bremsstrahlung, the tagging magnet used to deflect the electrons after the goniometer and the two hodoscopes Tagger and ARGUS. The tagging process will be explained in more detail later.

Goniometer

The goniometer is located inside the vacuum chamber. It is used to bring different radiators into the beam. A diamond radiator is used to produce a linearly polarized photon beam using coherent bremsstrahlung, while copper radiators are used to produce incoherent bremsstrahlung. The $67\,\mu$m copper radiator is chosen such that it produces the same flux as the diamond radiator used for polarized photons. A Chromox plate is used for beam alignment, as are a vertical and a horizontal wire which allow the measurement of the beam position and shape by moving them through the beam.

Tagger and tagging principle

The Tagger hodoscope is used to determine the momentum of the post-bremsstrahlung electrons. This is done be measuring the position of the electrons in the Tagger after the trajectory curves in the magnetic field of a dipole magnet located between the Tagger and the goniometer. Figure 3.4 shows the operating principle of the tagging system.

Electrons that did not undergo bremsstrahlung, do not hit the Tagger and are absorbed by the beam dump. Those that underwent bremsstrahlung, hit the hodoscope where their position is measured. Using a calibration detailed in [38] the momentum of the electrons and thus their energy can be calculated from the measured position. With knowledge of the initial electron beam energy the energy of the bremsstrahlung photon can be calculated as the difference in electron energies.

The Tagger hodoscope consists of 120 scintillator bars read out by photomultipliers. 54 of the scintillators are arranged in the focal plane of the magnet covering 10 % to 32 % of the initial electron
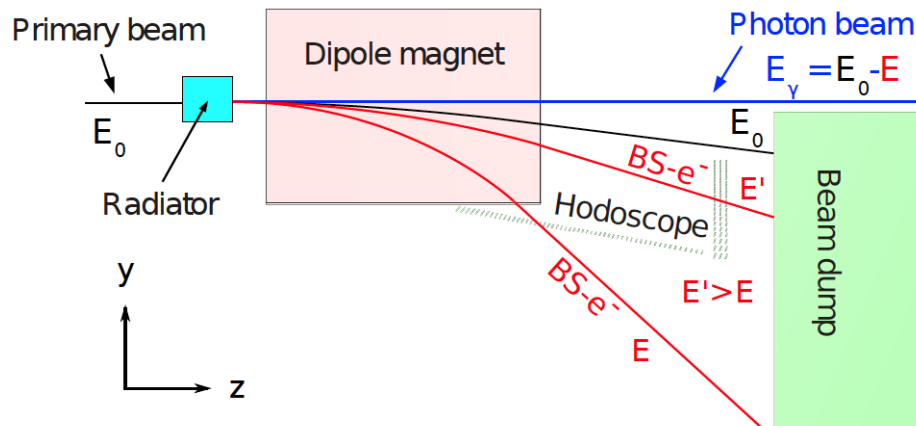
15

Figure 3.4: Schematics of the tagging system operating principle [27].

energy E_0 with an energy resolution of $0.4\,\% \cdot E_0$. Due to spatial limitations the other 66 scintillators are arranged vertically with a coverage of $32\,\% \cdot E_0$ to $90\,\% \cdot E_0$ and a resolution of $0.6\,\% \cdot E_0$ to $1.7\,\% \cdot E_0$.

The scintillators have an overlap of $55\,\%$ with their neighbor to reduce background and improve the resolution. The resulting energy channels, that will be used for the reminder of the analysis and determine the binning in beam energy, are created by the coincidence of two bars.

ARGUS

The ARGUS detector is a scintillating fiber detector located directly in front of the vertical part of the Tagger. ARGUS' purpose is to improve the energy resolution of the tagging system. ARGUS consists of 480 scintillating plastic fibers which are read out by photomultipliers. These fibers are closely stacked in three layers allowing for the reduction of background by demanding coincidences between fibers in different layers. ARGUS covers electron energies from $30\,\% \cdot E_0$ to $66\,\% \cdot E_0$ with a resolution of $0.08\,\% \cdot E_0$ to $0.45\,\% \cdot E_0$.

3.2.2 The central detectors and the target

After the bremsstrahlung-photons have passed the collimators in the beam dump, they enter the central part of the BGOOD experiment. It consists of the target surrounded by two cylindrical Mulit-Wire-Proportional-Chambers (MWPC), a scintillator barrel and the rugby ball calorimeter (also called the BGO ball). The central detectors are ideally suited for the detection of neutral particles via their decay into photons, but can also detect charged particles. A slice view of the central detectors can be seen in figure 3.5.

The target

The target is either filled with liquid hydrogen (LH2) or liquid deuterium (LD2). Two different target cells are available with a diameter of $4\,cm$, a wall thickness of $0.5\,mm$ and a length of either $6\,cm$ or
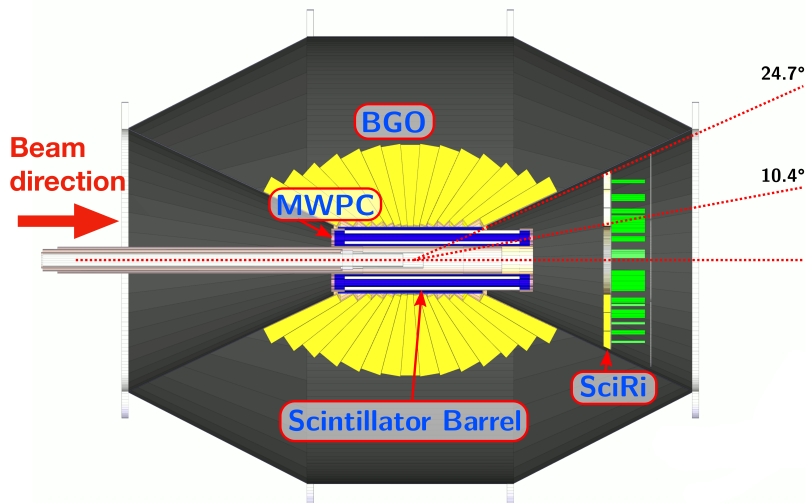
Figure 3.5: Slice trough the central detectors, based on [27]. On the right the SciRi detector which is located in the rugby ball holding structure can be seen, see subsection 3.2.3.

11 cm. The cell is made out of aluminum with the front and back window being made out of Mylar foil.

The MWPCs

Surrounding the target are two cylindrical MWPCs. They are used to track charged particles coming from the target and increase their angular resolution. They are not used for this work.

The barrel

The MWPCs are surrounded by a plastic scintillator barrel consisting of 32 strips each covering $11.25°$ in ϕ. It can be used to track charged particles and act as a veto for neutral particles since those do not deposit any energy in the barrel. Since a charged particle looses only a part ΔE of it's total kinetic energy E in the barrel, a $\frac{\Delta E}{E}$ measurement can be performed using the energy deposited in the rugby ball, which corresponds to the total kinetic energy. Figure 3.6 shows an example of this.
As can be seen, there are two distinct lines for protons and π^+ and they can be well separated. For higher deposited energies in the rugby ball the lines start to overlap and the particles can not be distinguished anymore.

The BGO rugby ball

The BGO rugby ball (called rugby ball from here on) is the outermost detector of the central detectors. It consist of 480 Bismuth-germanium-oxide crystals which cover all of ϕ and a Θ range from $25°$ to $155°$. The crystals are 24 cm (over 21 radiation length) long and are shaped such that each crystal covers between $6°$ and $10°$ in Θ and $11.25°$ in ϕ. Their length enables them to fully absorb the total energy of a photon through an electromagnetic shower. Charged particles will deposit their kinetic energy in the calorimeter although they will not be completely stopped if their kinetic energy is too high.
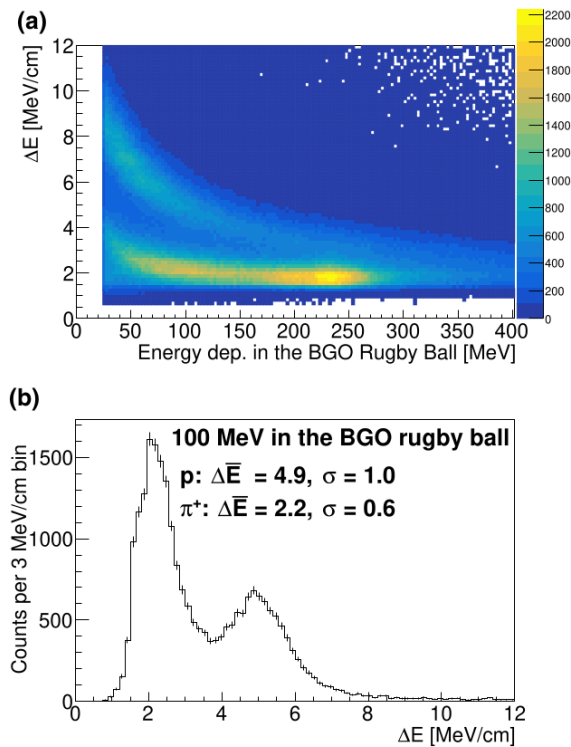
Figure 3.6: $\frac{\Delta E}{E}$ measurement using the barrel and the rugby ball. [27]. (a) shows the energy ΔE deposited in the barrel as a function of the energy deposited in the rugby ball, while (b) shows a projection of this plot at 100 MeV energy deposited in the rugby ball. The approximate gaussian mean and sigma values for the proton and π^+ peak are given in the plot.

3.2.3 Intermediate detectors

The two intermediate detectors SciRi (scintillating ring detector) and MRPC (Mulit-Resisitive-Plate-Chamber) cover the acceptance region between the central detectors and the forward spectrometer. Their location relative to the central detectors and the first detectors of the forward spectrometer can be seen in figure 3.7.

SciRi

SciRi consists of three rings of scintillators around the beam axis read out by avalanche-photodiods. It is located inside the holding structure of the rugby ball and covers a Θ range of $10°$ to $25°$ with a resolution of $5°$.

The MRPC

The MRPC covers the same angular region as the SciRi detector. As of the writing of this thesis it is still under commissioning and therefor not used in this work.
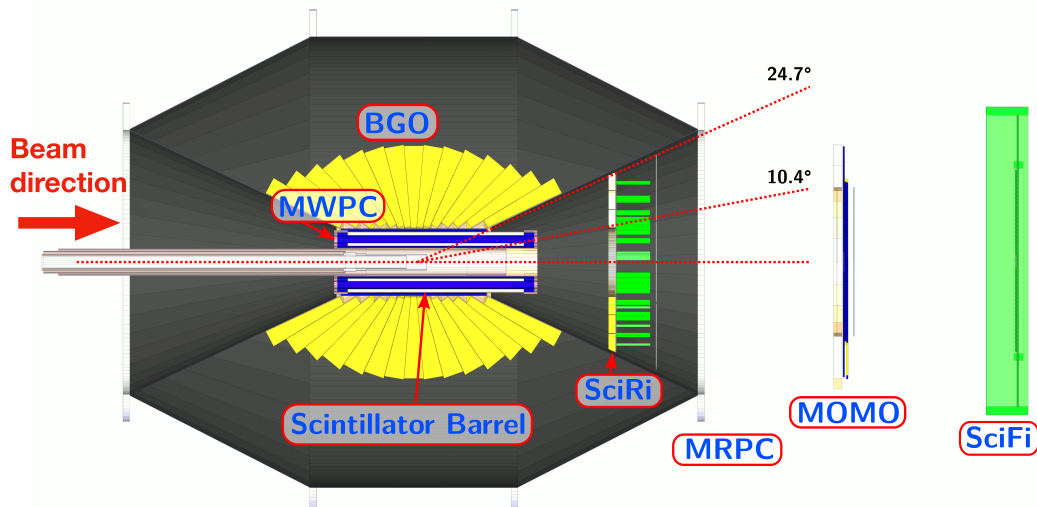
Figure 3.7: Location of the intermediate detectors relative to the central detectors (left) and the MOMO and SciFi2 detector which are part of the forward spectrometer [27].

3.2.4 The forward spectrometer

The forward spectrometer is ideally suited for the detection and identification of charged particles via the curvature of their trajectory in a magnetic field. The identification process is laid out in more detail later in this section. It consists of tracking detectors in front (MOMO and SciFi2) and behind (eight driftchambers and three Time-of-flight (ToF) walls) a large open dipole magnet. The ToF walls are also used to determine the particle β. Figure 3.8 shows the setup of the forward spectrometer. It covers Θ angles from $1.5\,^\circ$ to $8.2\,^\circ$ for the vertical plane and $12.1\,^\circ$ for the horizontal plane with an angular resolution of $0.3\,^\circ$, a momentum resolution of $3\,\%$ and a β resolution of $2.4\,\%$ over a momentum range of $400\,\mathrm{MeV}$ to $1\,100\,\mathrm{MeV}$.

MOMO and SciFi2

MOMO and SciFi2 are scintillating fibre detectors used to track charged particles in front of the open dipole magnet. There is a quadratic gap in the middle of the detectors to let the photon beam pass.

Magnet

The magnet is used to bent the trajectories of charged particles after the initial tracking detectors. It has a maximum integrated field strength of $0.71\,\mathrm{Tm}$, but was operated at $0.216\,\mathrm{Tm}$ for the data used in this work.

Drift chambers

The eight drift chambers are arranged in four different orientations to remove track finding ambiguities. There are two chambers with vertical (X) and horizontal (Y) wires respectively and two each with a tilt of $\pm 9\,^\circ$ (U/V) against the vertical plane. Like MOMO and SciFi2 the drift chambers have a dead spot in the center where the photon beam passes the detectors.

The chambers are filled with a mixture of Argon and carbon dioxide. They have a position resolution of better than $300\,\mu$m and are used to track the particles after they have been curved by the magnet.

Time-of-flight walls

The three time-of-flight walls are located at the end of the forward spectrometer. They consist of horizontal scintillating bars with a gap for the photon beam in the center and are used to determine the flight time of charged particles starting from the target with a time resolution of 0.34 ns. This information is used to calculate the β of a particle. Furthermore the ToF walls are also used to track particles after the driftchambers.

Tracking finding and performance

Tracking in the forward spectrometer is a multi-stage process. First tracks (see subsection 3.3.1) are created between the target and MOMO/SciFi2 as well as between clusters in the ToF walls. If these front- and back-tracks meet in the vertical plane where no deflection due to the Lorentzforce can be assumed, they are combined to a track running through the whole forward spectrometer. A first estimate of the particle trajectory in the horizontal plane and the momentum is made from this track, based on the assumption of a uniform field in the magnet without any fringe fields. After that, a correction to trajectory and momentum is made as a function of momentum using a 3D field-map, that includes fringe fields and non-uniformities. Subsequently all driftchamber clusters close to the corrected trajectory are added to the track. Tracks with less then three driftchamber clusters are discarded. Figure 3.8 shows these steps.
Finally the particle is traced step-wise from the target through the whole forward spectrometer. The initial direction is taken from the front-track while the initial momentum guess is taken from the before created track. The energy loss along the particle path is taken into account, meaning that the tracing has to be done individually for different particle hypothesis. The initial momentum is varied iteratively until the best agreement between the final particle trajectory and the clusters belonging to the track is found.
The β is calculated from the flight time of the particle taking into account the length of the final trajectory. Using the β and the momentum, the mass of the particle can be calculated. Figure 3.9 shows the performance of the forward spectrometer.

3.2.5 Detectors for photon-flux measurement

The photon-flux, the amount of photons that passed the collimator and hit the target cell, is measured by the two detectors GIM and FluMo behind the forward spectrometer.

FluMo

FluMo (Flux-monitor) is composed of five 0.5 cm thick scintillators, that detect electrons and positrons coming from photons, that did not interact with the target and underwent pair-production in the forward spectrometer. The scintillators are arranged behind each other and are used in coincidence to reduce background. Since not all photons undergo pair-production FluMo only measures a fraction of the total photon-flux. The total flux can be calculated with the known detection efficiency of FluMo which is determined in low rate runs, where the GIM detector can still measure the total flux.
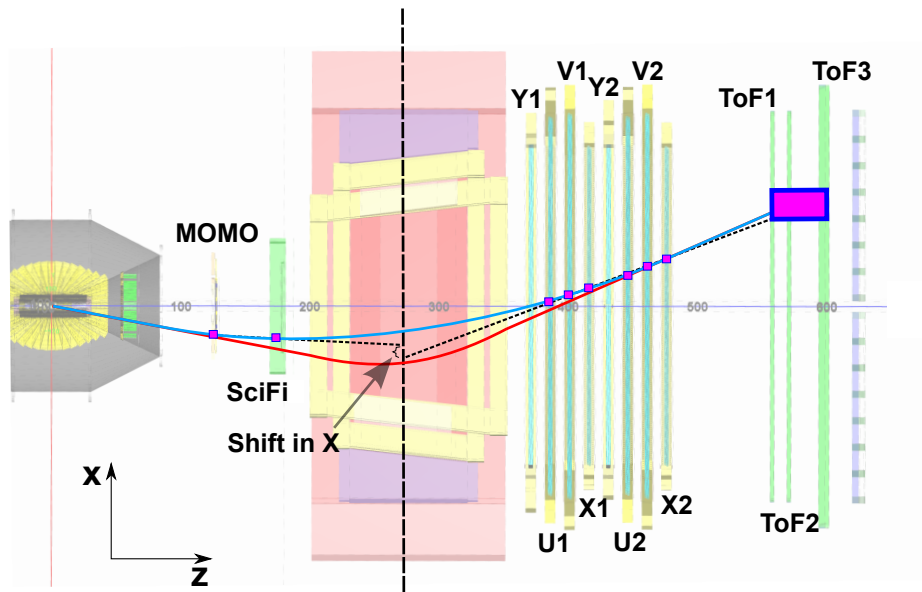
Figure 3.8: Setup of the forward spectrometer and first steps of the track finding in the horizontal plane [27]. X, Y, U and V indicate the different drift chamber orientations. The grey bar behind ToF3 (the third time-of-flight wall) represents the concrete wall at the end of the experimental area.

Purple squares indicate clusters in the different detectors. The two dotted lines are the initial front and back tracks, which are allowed to have a certain offset between them, indicated by the X. The solid red line is the first trajectory guess assuming a uniform field while the corrected trajectory is shown in blue. The strength of the correction is not to scale.

GIM

GIM (gamma-intensity-monitor) is the second detector used for flux measurement, located behind FluMo. It consists of a lead glass block that is 28 cm long, which allows for the total absorption of beam photons. For low photon rates GIM can measure the total photon-flux, whereas for higher rates the detector starts to saturate, such that FluMo has to be used for an accurate measurement.

3.3 Analysis tools

This section describes the most important analysis tools used for this work. It starts with a description of the Explora (Extended Pluggable Objectoriented ROOTified Analysis) framework [39], that is being used at the BGOOD experiment and how the information from detectors is processed in this framework. Later on the Root framework [40] is described.
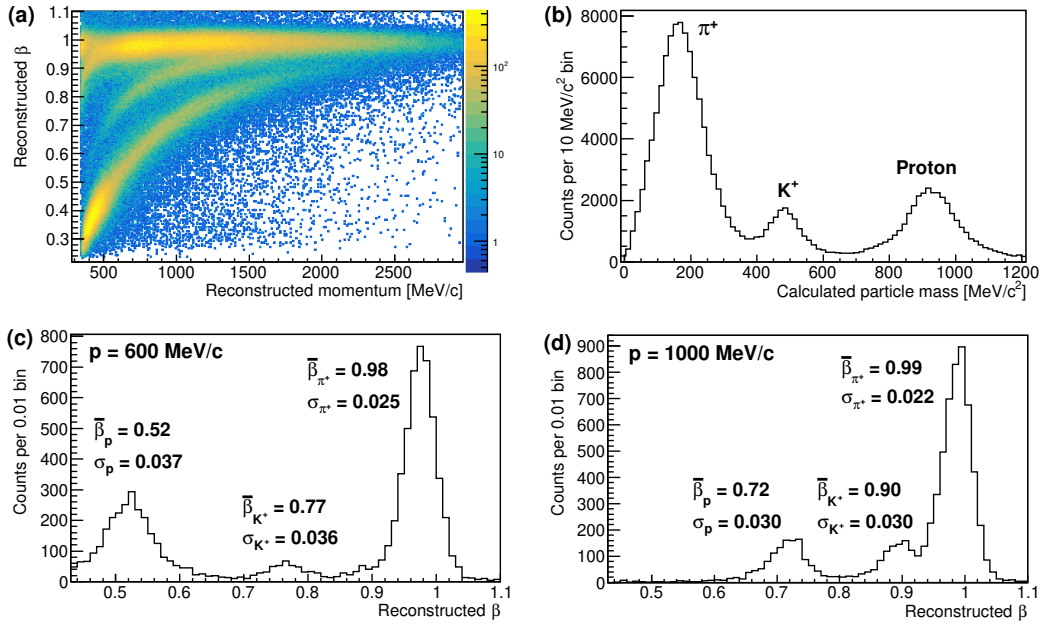
Figure 3.9: Performance of the forward spectrometer [27]. a) shows the particle β vs the particle momentum. A photon beam energy of over 900 MeV, an energy deposit of less then 250 MeV and a π^0 reconstructed in the rugby ball are required to improve the visibility of K^+. The visible lines correspond to π^+, K^+ and protons from top to bottom. For higher momenta these lines start to overlap making a distinction between the particles difficult. b) shows the calculated masses for particles with a momentum between 600 MeV and 1 000 MeV. c) and d) show the calculated particle β for momenta of 600 MeV and 1 000 MeV respectively. The numbers inset, show the gaussian means and widths of the respective particles peaks.

3.3.1 The Explora framework

The Explora framework [39] has been created for the CBELSA/TAPS at ELSA experiment [41], but has been subsequently adapted for the BGOOD experiment. It is written in C++ and XML and contains the necessary code to read in and analyze the data taken by the experiment. It allows users to create their own plugins and embed them into the existing framework.

Explora is further used for the simulation of reactions. The kinematics of the simulated reaction are calculated and the final state particles before their decays are created. The passage of the simulated particles through the experimental setup, which is implemented in the simulation, as well as their decays are simulated using Geant4 [42].

The rest of this subsection will explain the hit, cluster and track object, especially the forward track which is important for this analysis.

Hits

Hits correspond directly to an energy deposit in one element of a detector (e.g. one crystal of the rugby ball). A hit contains information about the amount of energy deposited, the position of the detector element and the time at which the deposit happened. Due to their different setups the exact information contained in a hit differs for the various detectors.

Clusters

Multiple nearby hits in a detector can be combined to form a cluster. Figure 3.10 shows an example of how clustering works. A cluster is created if different hits are adjacent in space and time. The exact algorithm is different for each detector, due to their differences in geometry.

Time and position of the cluster are given by the mean of the values of the individual hits composing the cluster. This results in a better resolution than for individual hits and reduces background, since accidental hits are not included in the cluster. The energy of the cluster is the sum of the energy of all hits.
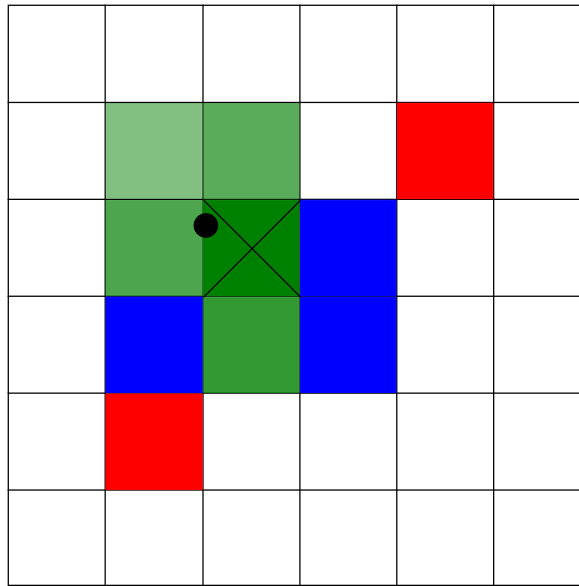
Figure 3.10: Clustering principle: a particle entered the detector in the segment denoted by the X and deposited energy. Hits in green are adjacent to this initial hit (they share an edge) and within time. Hits in blue are also adjacent but are not in time, whereas the hits in red are in time but not adjacent. Thus the cluster consists of the hits in green. The position is given by the weighted average of the energy deposits (the intensity of the color indicates the amount of energy deposited) in the cluster denoted by the filled black circle. The red hits are examples of accidentals being cut away by clustering.

Tracks

Tracks are created by combining clusters or hits from different detectors together, if they lie on a line and are within time. Figure 3.11 shows an example of how a track can be created.

There are three types of tracks being used for this analysis. The first one is the Tagger-track which combines the information from Tagger and ARGUS. The energy associated with this track is the energy of the post-bremsstrahlung photon and not the energy deposited in the detectors themselves. The central track combines the MWPC, barrel and rugby ball. Its energy information is given by the energy deposited in the rugby ball, while the direction of the particle is calculated through the position of the hits in the MWPC and barrel (both only for charged particles) and in the rugby ball. This requires a coincidence in ϕ as well es in time between MWPC/barrel and rugby ball. If there is no hit in the barrel, the particle can be assumed to be uncharged. The size of the rugby ball cluster can
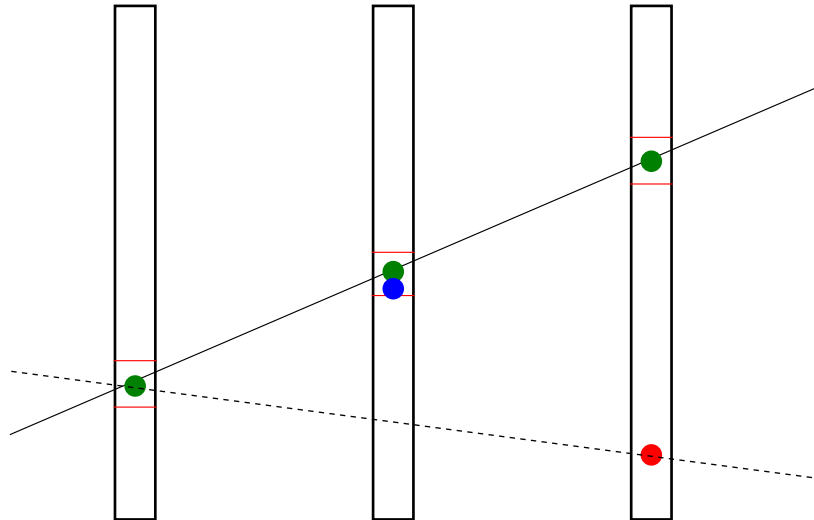
Figure 3.11: Tracking principle: a particle passes three detectors and deposits energy in them. The circles indicate the resulting clusters. The green clusters are in time and lie on a straight line. The blue cluster is close enough to be also considered for the track (indicated by the red lines), but it is not in time. The red cluster is also in time. If an energy deposit in all three detectors is required, the solid line is the only possible track. If a signal is only required in two detectors, the dotted line would also be a viable track. Assuming that the red cluster is an accidental, this shows how noise can be suppressed by tracking.

also be used to distinguish particles as photons will create much larger clusters (due to electromagnetic showers) than hadrons, that only deposit their kinetic energy through collisions.

The forward track combines all the detector in the forward spectrometer. Since a charged particle's trajectory is bend in the magnetic field, this track is not straight. There are only charged forward tracks, as the forward spectrometer can not detect neutral particles. For a more detailed explanation on the tracking in the forward spectrometer see subsection 3.2.4. The forward track contains information about the momentum as well as the mass of the particle.

The central and forward tracks both originate from the target center and can be evaluated under the hypothesis, that the track belongs to a specific particle (e.g. a proton). Using this hypothesis and the energy/momentum information available from the track, the complete four-momentum of the particle can be calculated taking into account the specific energy loss for this particle. A probability that the given hypothesis is correct can be calculated based on information from the clusters like charge, size etc.

These tracks are called fitted tracks. Every track mentioned in this work from now on is a fitted track.

3.3.2 Root

Root [40] was developed at CERN and is used in high-energy physics to handle large quantities of data. It also provides classes, that have a lot of utility like the TLorentzvector which is a 4-vector, that allows for easy calculation of the mass and angles of a 4-vector and can easily be boosted into different reference frames. Furthermore Root is used for the creation of all histograms found in this thesis.

Analysis

This chapter contains a detailed description of the analysis performed in this work. It starts with general remarks on the analysis, followed by an in depth look into the different η' decay modes, that are analyzed. At the end, the results from those decay modes are compared.

All reactions investigated in this analysis are photoproduction. For better readability they are only referred to by their final state from now on (e.g $\gamma p \to \eta' p$ is called $\eta' p$). The cross sections are determined in the first three Tagger energy bins above threshold, where there is a significant amount of $\eta' p$ events with a proton in the forward spectrometer. These bins are named 1450, 1477 and 1504 from now on, which is the central value of these energy bins in MeV.

4.1 Methodology

In this section some general aspects of the analysis are explained. The data set used for this analysis is presented, along with the proton reconstruction and a short overview over the different η' decay modes. Furthermore the relevant backgrounds are presented and the determination of statistical and systematic errors is shown.

4.1.1 Data set

The same data set is used for all analysis. It consists of data from four different beam times with differing electron beam energy E_0 and target length l_{target}. Table 4.1 shows the parameters of the individual beam times. All beam times used unpolarized electrons and a liquid hydrogen target. If not stated otherwise, data shown in this work always stems from the combination of all beam times.

beam time	E_0	l_{target}	integrated flux	beam hours
2015-06	2.9 GeV	6 cm	$4.9 \cdot 10^{12}$	284
2015-11	3.2 GeV	6 cm	$7.5 \cdot 10^{12}$	368
2017-04	3.2 GeV	6 cm	$1.5 \cdot 10^{13}$	345
2018-12	2.9 GeV	11 cm	$1.1 \cdot 10^{13}$	359

Table 4.1: Parameters of the different beam times used in this analysis.

Because the Tagger measures energies relative to E_0, beam times with differing E_0 have different Tagger energy binnings. To combine data, the binnings need to be converted. Figure 4.1 shows how different binnings are combined. The binning of the 2017-04 and 2015-11 beam times is used for this work.
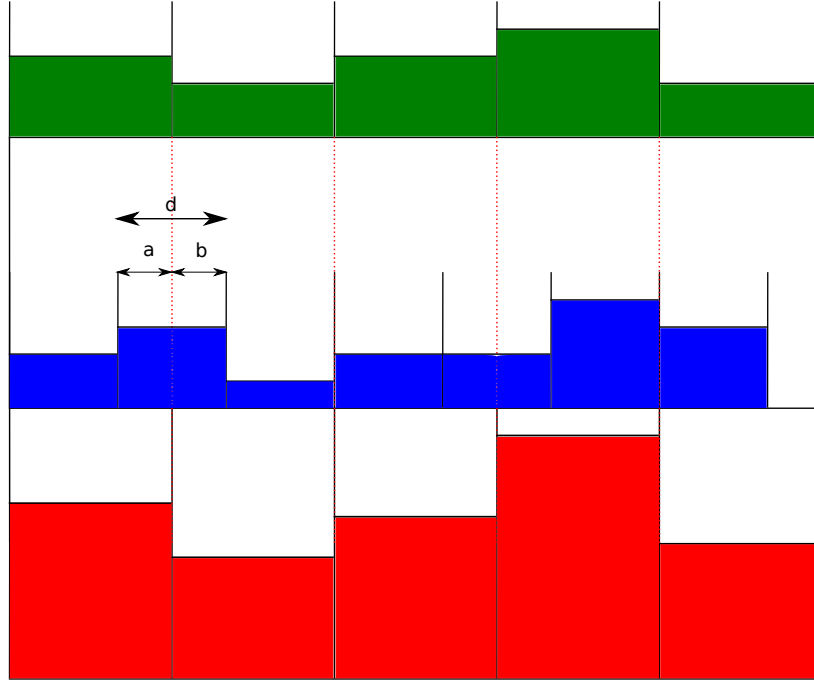

Figure 4.1: Events in blue are added to the green binning resulting in red. The red dotted lines show the overlap between green and blue. Blue bins that overlap with two different green bins are split to those two, depending on their overlap with each bin. With N being the number of events in the second blue bin, this means that $\frac{a}{d} \cdot N$ events go into the first green bin while $\frac{b}{d} \cdot N$ events go into the second green bin. This is done for each of the blue bins.

Due to the difference in target cell size, the 2018-12 beam time has slightly different resolutions than the other beam times. Whenever cuts are made, the same cut in terms of σ is applied to long and short target data.

4.1.2 Proton reconstruction

Due to kinematic focusing, close to threshold almost all protons from $\eta' p$ are going in forward direction in the lab frame, meaning that they will be detected in the forward spectrometer. Looking at all forward tracks (see subsection 3.3.1), only those with a positive charge as well as a mass $m_{\text{forward,positive}}$ within 2σ of the proton mass peak are selected. Figure 4.2 shows $m_{\text{forward,positive}}$, which is calculated from the particle β and momentum for all forward tracks with a positive charge.
As can be seen, there is a clear peak at the proton mass, as well as overlapping peaks for e^+ and π^+. There is a small background below the proton peak due to misidentified events.
Figure 4.3 shows the relation between $\cos(\Theta_{\eta'}^{\text{CMS}})$ and proton lab angle Θ_p^{lab} for the three energy bins. As can be seen all protons in the 1450 bin have lab angles of less than $8\,^\circ$, which is the vertical
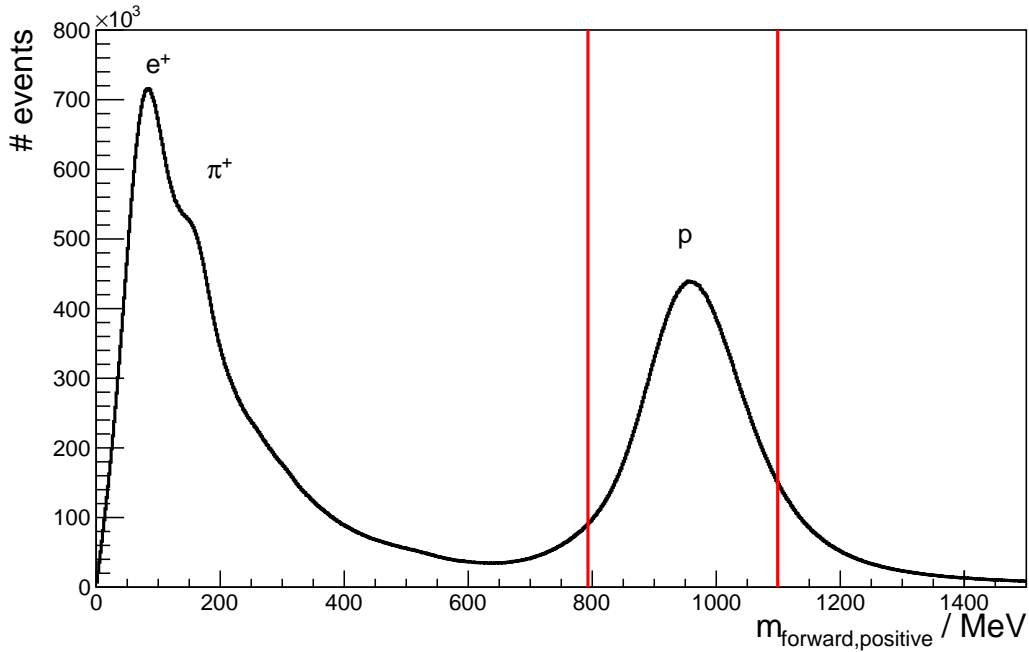
Figure 4.2: Calculated mass of forward going positive particles for all beam times: the e^+ and proton peaks are clearly visible, while the π^+ shows up as a shoulder. The red lines indicate the cuts applied for the short target beam times.

acceptance of the forward spectrometer [27]. Protons in the 1477 bin may have an angle exceeding this value, although their lab angles are still below $12°$, the horizontal acceptance of the forward spectrometer [27]. In the 1504 bin, proton lab angles can exceed this value.

Since proton and η' go back-to-back in the CMS, a $\cos(\Theta_{\eta'}^{CMS})$ value close to zero corresponds to a $\cos(\Theta_p^{CMS})$ value around zero. Thus the proton momentum in the CMS is mostly perpendicular to the beam axis for these events, resulting in large Θ_p^{lab} after the boost. Events more to the edges of the $\cos(\Theta_{\eta'}^{CMS})$ range have smaller transverse proton momenta and thus smaller Θ_p^{lab}. As can be seen in figure 4.3 the biggest Θ_p^{lab} correspond to a $\cos(\Theta_{\eta'}^{CMS})$ slightly above zero. Protons from those events are going slightly backwards in the CMS. Thus they not only have a large momentum perpendicular to the beam axis, but their momentum component parallel to the beam is opposite to the beam direction. This results in a smaller lab momentum in beam direction after the boost, as well as a large momentum perpendicular to the beam axis. As a result these protons have the largest lab angles. All distributions show a certain width in Θ_p^{lab}, due to the energy bins also having a certain width.

It can further be seen, that over a large range of $\cos(\Theta_{\eta'}^{CMS})$ protons have very similar lab angles. These events can only be distinguished and ordered into the proper CMS angular bins, using their momentum. This differs with $\cos(\Theta_{\eta'}^{CMS})$, because for different $\cos(\Theta_{\eta'}^{CMS})$ the momentum component parallel or anti-parallel to the beam axis changes, resulting in changes in the lab momentum.

Thus it is crucial to ensure a proper determination of the proton momentum. For that, the relation between the measured proton momentum and the generated proton momentum is checked using
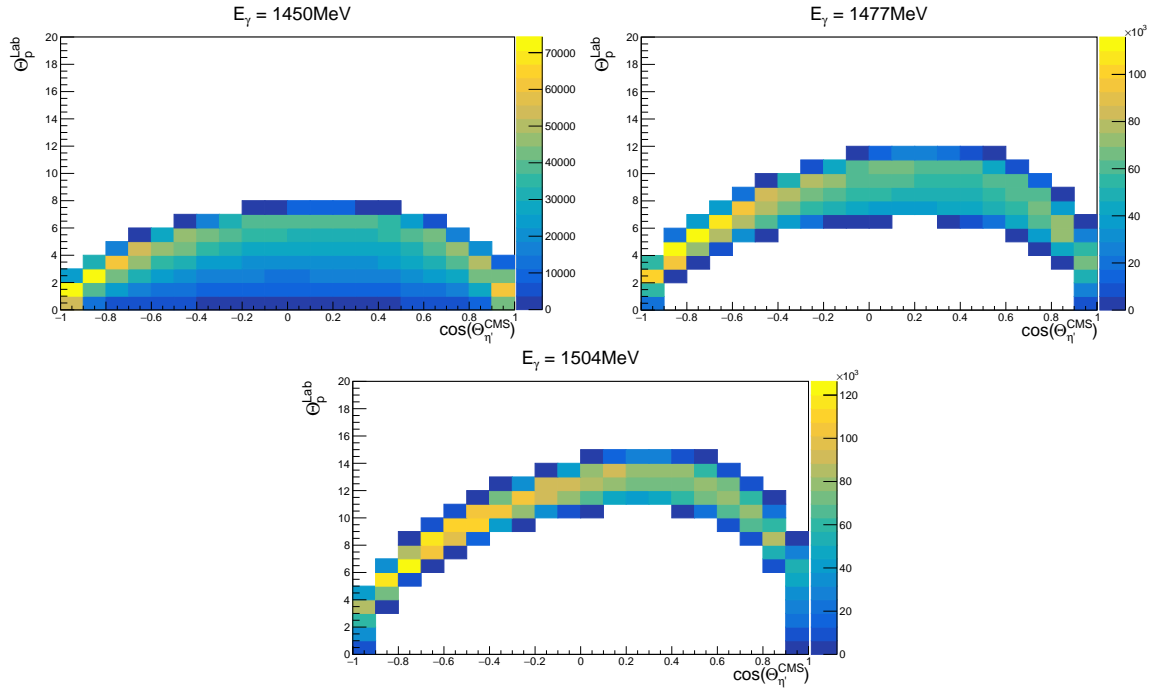
Figure 4.3: Correlation between $\cos(\Theta_{\eta'}^{CMS})$ and Θ_p^{lab} for $\eta' p$ for the three investigated Tagger energy bins. The results shown are the generated parameters from simulation. The respective photon energy is given in the title of each plot.

simulated $\eta' p$ events. The simulation was performed using only phase space. As shown in figure 4.4 there is a systematic linear offset between the two.

This offset depends on the lab momentum of the proton and on its direction in the CMS. This is evident in the 1477 and 1504 bin in figure 4.4, where there are two lines corresponding to protons going forwards (right line, high momentum) and backwards (left line, low momentum) in the CMS. This split is not visible in the 1450 bin, since the proton CMS momentum is small close to threshold and does not hugely influence the proton lab momentum. This difference between forwards and backwards arises, because the correction does not only depend on the momentum, but also on the position in the forward spectrometer. Since protons with the same lab momentum have different lab angles, depending on their direction in the CMS, their corrections look different.

There are on-going efforts to make a proton momentum correction, that is reaction-independent and takes into account the direction of the proton in addition to the absolute value of the momentum. For this work a correction to the proton momentum is determined only as a function of momentum, by fitting a gaussian function to 10 MeV wide slices in momentum and determining the central value. The central values of all fitted gaussians as a function of proton momentum are shown in figure 4.5. As already seen in figure 4.4, there is a linear offset between the measured and the generated proton momentum. This can clearly be seen in the 1450 bin in figure 4.5. In the 1477 and 1504 bin, this offset is different for forward and backward going protons, i.e. high and low momentum protons. This results in two different linear corrections with a region between them, where both types of protons overlap. In the 1477 bin this overlap lead to a bump-like structure in the ratio between measured and generated proton momentum. In the 1504 bin no proper fits can be made in this region, leading to
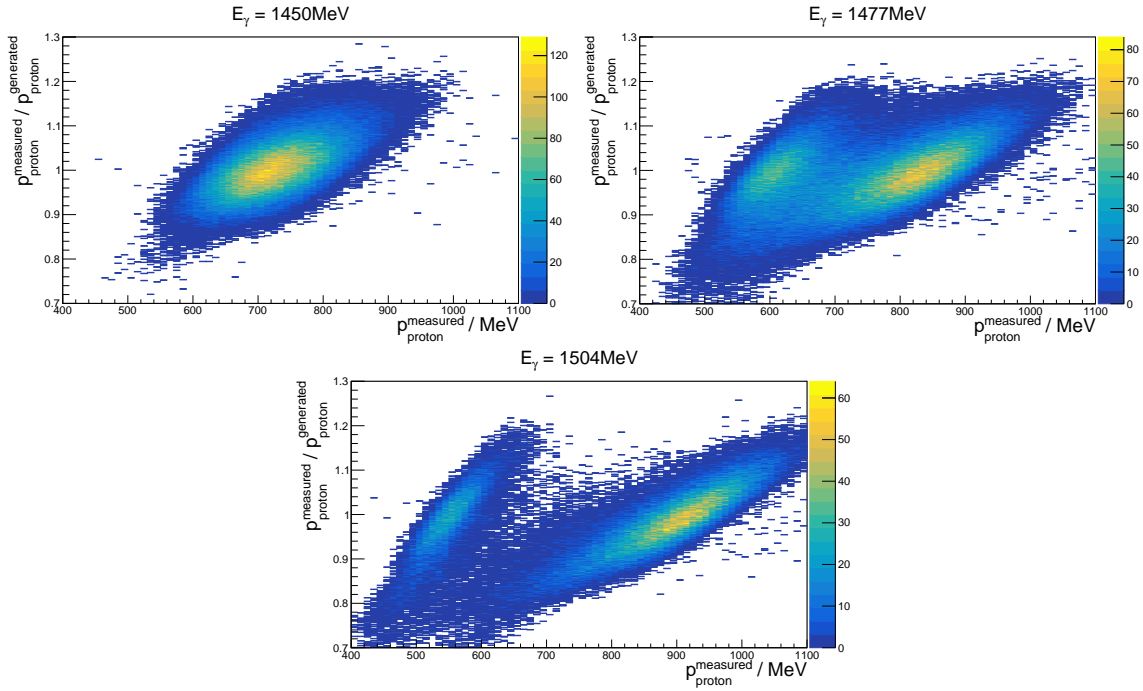
Figure 4.4: Ratio between measured and generated proton momentum as a function of the measured momentum for $\eta' p$. The results shown are from simulation. The respective energy is given in the title of each plot.
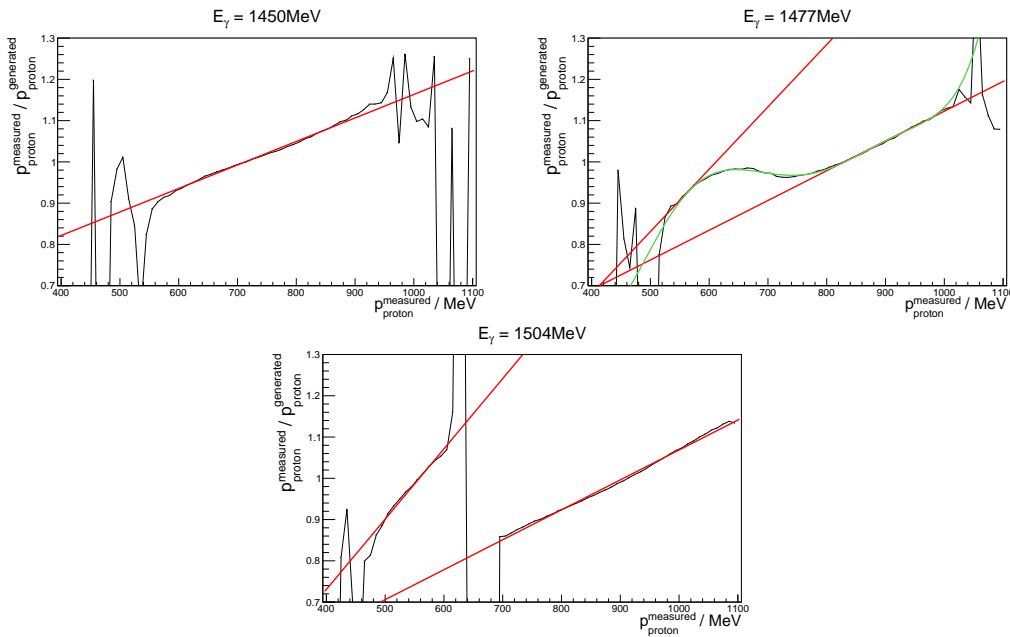

Figure 4.5: Mean value of the ratio between measured and generated proton momentum as a function of the measured momentum for $\eta' p$. The ratio is taken from gaussian fits to the plots in 4.4 in 10 MeV slices. The red fits are linear, while the green one is of sixth degree.

arbitrary values, which can be seen by the graph jumping up and down.

Very small and high momenta correspond to the proton going nearly against or in beam direction in the CMS, respectively. This results in very small lab angles, such that these events may hit the acceptance hole in the forward spectrometer. This results in limited statistics for these momenta and thus the gaussian fits do not work reliably anymore. This results in the strong fluctuations seen in figure 4.5 for high and low momenta.

To determine the correction factor, a linear function was fitted to the graphs in the linear region and used to extrapolate into those regions with limited statistics. The overlap region in the 1477 bin was additionally fitted using a polynomial of sixth degrees, while the overlap region in the 1504 bin was not fitted at all. Events from this region are corrected with the average of the two linear corrections. By dividing the measured momentum by the respective value taken from the fits shown in figure 4.5, the actual momentum for each proton is determined. The resulting ratios between measured and generated proton momentum are shown in figure 4.6.
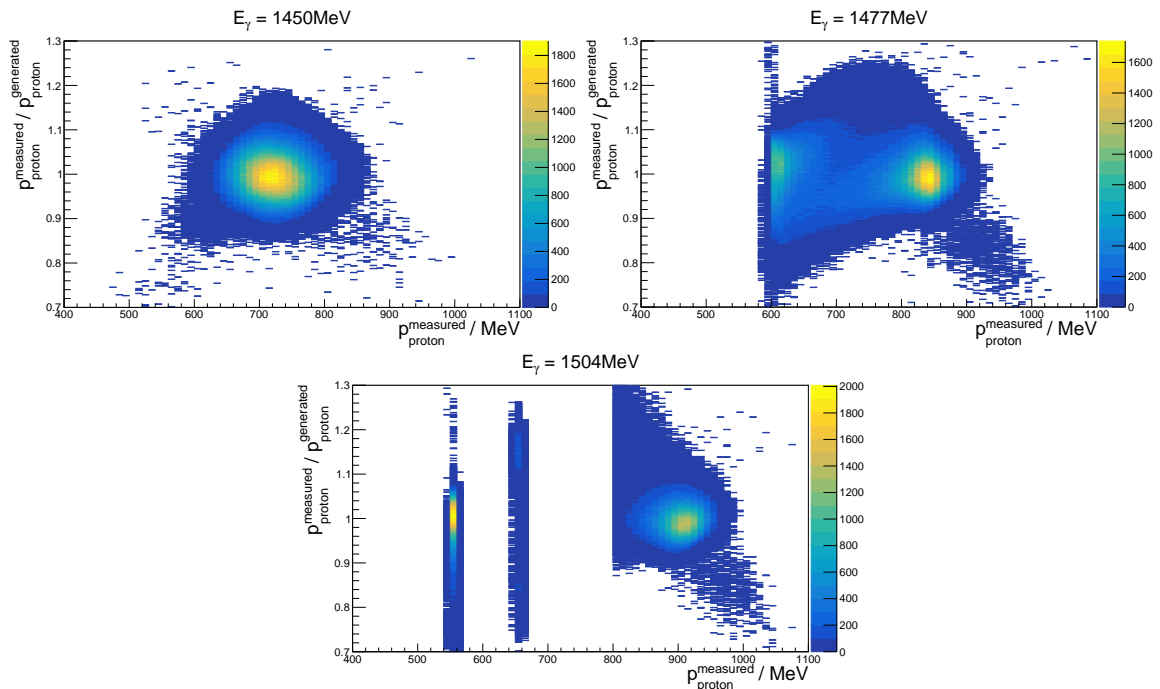

Figure 4.6: Ratio between measured and generated proton momentum as a function of the measured momentum for $\eta' p$, with the proton momentum correction applied. The results shown are from simulation. The respective energy is given in the title of each plot.

For the 1450 bin all events are now centered along one. For the 1477 bin this is the case for high and low momentum protons, but in the region between them two slight linear offsets can still be seen. As mentioned above this is the region, where forward and backward going protons overlap, such that an ideal correction is not possible. This is also the reason for the downward tail seen towards higher momenta.

In the 1504 bin, a gap is visible between the high and low momentum protons. Events with a momentum within this gap have larger proton lab angles than the acceptance of the forward spectrometer and as a result can not be detected. Events that were previously measured here, have been moved to their

correct momenta, which are either higher or lower. A small amount of events is still left in this region. These are protons from the overlap region, that were corrected with the average of the forward and backward correction. With a proper momentum correction these events can be separated and properly corrected. The downward tail at higher momenta is again visible.

As mentioned before, there are on-going efforts to make a proton momentum correction, that is reaction-independent and also takes into account the direction of the proton in addition to the absolute value of the momentum. With this more precise correction implemented these artifacts will disappear. For now, the poorly corrected events in the 1504 bin are removed from the analysis, as they do not have a correct momentum and do not heavily contribute to the overall statistics.

Looking at figure 4.6 it can further be seen, that all simulated events have a proton momentum between 400 MeV and 1 100 MeV. The momentum region of optimal performance for the forward spectrometer is 400 MeV to 1 100 MeV [27] and as shown in figure 3.9 protons, kaons and pions can be well separated there. Thus a cut from 400 MeV to 1 100 MeV is placed on the momentum of detected protons, as this ensures a good resolution and background reduction, without cutting away any signal. Thus forward tracks with a positive charge, a calculated mass consistent with the proton mass and a momentum between 400 MeV and 1 100 MeV are considered protons. If no proton can be identified under these conditions the event is discarded.

Figure 4.8 shows the number of protons in the forward spectrometer per Tagger energy bin, normalized by the integrated flux (shown in figure 4.7), over the whole angular range. The flux is plotted per Tagger energy bin and, since the Tagger energy bins have differing sizes, does not follow a $1/E_\gamma$ shape. Dividing the number of protons in the forward spectrometer per Tagger energy bin by the integrated flux shown in figure 4.7, the effects of the Tagger geometry, as well as effects from variations in the efficiencies of the different coincidence channels, cancel out.

As can be seen in figure 4.8 different reaction channels are visible as peaks close to their respective thresholds, due to kinematic focusing. The proton momentum correction is not applied to this plot to showcase what the spectrum looks like. As will be seen later, the fact that the proton momentum correction is only applied to three energy bins, changes the appearance of the spectrum.

Thus by just requiring the proton in the forward spectrometer, a clear $\eta' p$ peak is visible above background with very good statistics. Nonetheless this totally inclusive method (called $\eta' \to X$ from now on) has a substantial background, leading to a poor S/N.

The S/N can be improved by requiring some or all of the η' decay products. These more exclusive analysis methods suppress background, but also decrease the available statistics. Subsection 4.1.3 shows the different η' decay modes, that were analyzed in this work in addition to the totally inclusive case.

4.1.3 η' reconstruction and decay channels

As mentioned in subsection 4.1.2, the background can be reduced by requiring some or all of the η' decay products. Since these decay products are largely detected in the rugby ball, which is ideally suited for the detection of photons, neutral decays are best analyzed.

Photons can be distinguished from other particles in the rugby ball due to two characteristics: they produce a large cluster (see subsection 3.3.1) in the rugby ball due to the electromagnetic shower they produce, which spreads to multiple crystals. Figure 4.9 shows the cluster size for photons in comparison to protons. As can be seen protons exhibit a cluster size of mostly one, while clusters stemming from
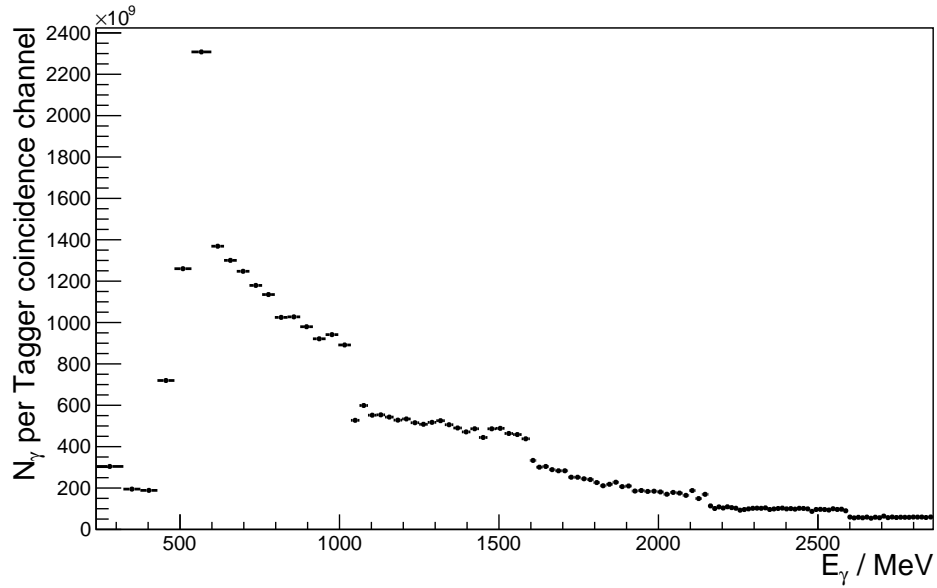
Figure 4.7: Integrated flux for all beam times combined: the sudden jumps at 1 000 MeV, 1 600 MeV and 2 150 MeV are due to changes in the size of the Tagger scintillators. The binning is again the Tagger energy binning.
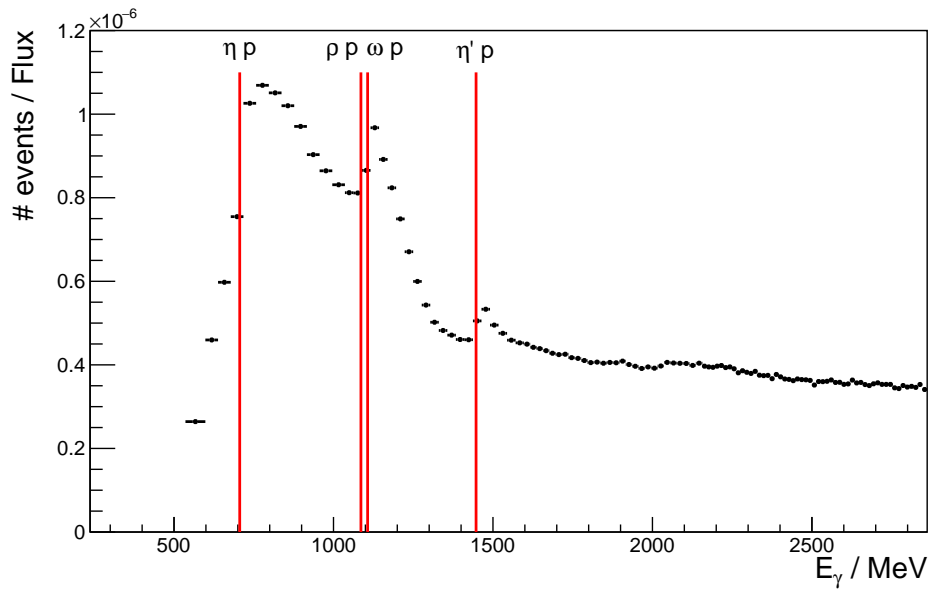

Figure 4.8: Number of protons in the forward spectrometer for each Tagger bin divided by the integrated flux. The red lines indicate the thresholds of different reactions. The horizontal error bars indicate the width of the energy bins.

photons are more extensive, as expected. This is because in contrast to the electromagnetic shower, protons mostly lose their energy through collisions and as such only deposit them in the one crystal they are traversing. With increasing energy of the particles the difference in cluster size increases.
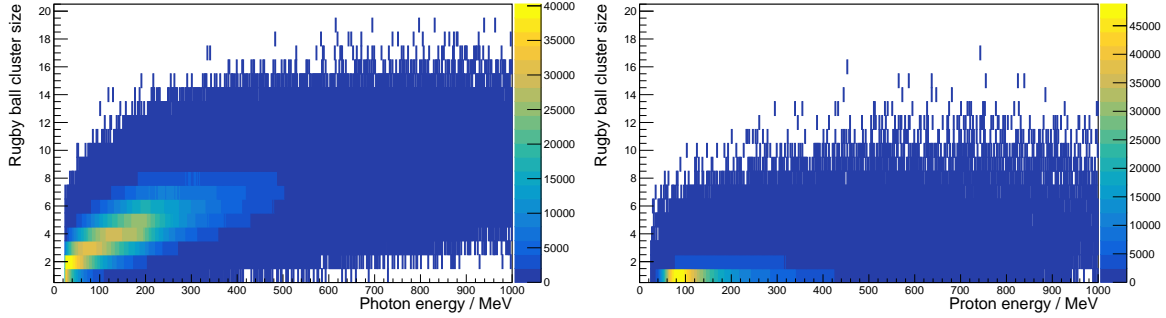

Figure 4.9: Cluster size in the rugby ball for photons (left) and protons (right) with respect to the energy of the photon/proton. The cluster size corresponds to the crystal multiplicity. The data shown is simulated data.

Neutrons can only interact hadronically with the target material. Charged particles produced during this interaction will subsequently loose their kinetic energy through Bethe-Bloch-ionization. This happens mostly in the crystal the original neutron was traversing and thus leads to a small cluster size. Secondly photons mostly do not produce a hit in the scintillator barrel and the rugby ball simultaneously, as they can only interact with the scintillator material by being absorbed or through Compton scattering, which is much less likely. As a result only central tracks (see subsection 3.3.1) without a scintillator barrel hit and a rugby ball cluster size bigger than one are accepted as photons. More details on how the decay products of the η' are reconstructed from the photons can be found in subsections 4.2.1 to 4.2.3.

Given their branching ratios, cf. table 2.1, $\eta' \to \pi^0 \pi^0 \eta$ with both π^0 and η decaying into two photons and $\eta' \to \gamma\gamma$ are the ideal decay channels for an analysis. The $\eta' \to \pi^0 \pi^0 \eta$ decay channel is analyzed in two ways, with increasing exclusiveness. First $\eta' \to (\pi^0 \pi^0)\eta$, where the η is reconstructed from its two-photon decay and the $\pi^0 \pi^0$ are determined as the missing mass to the ηp system. Secondly $\eta' \to \pi^0 \pi^0 (\eta)$, where the two π^0 are reconstructed from their two-photon decays and the η is reconstructed through the missing mass to $\pi^0 \pi^0 p$ system.

For the totally exclusive reconstruction the $\eta' \to \gamma\gamma$ decay is used, where the η' is explicitly reconstructed from its decay into two photons. Due to the reconstruction, little background is left, but the statistics are also heavily reduced due to the low reconstruction efficiency and branching ratio. Table 4.2 shows the combined branching ratios for these three decay modes, including the branching ratios for $\pi^0 \to \gamma\gamma$ $((98.823 \pm 0.034) \%$ [15]) and $\eta \to \gamma\gamma$ $((39.41 \pm 0.20) \%$ [15]).

analyzed decay mode	combined branching ratio / %
$\eta' \to (\pi^0 \pi^0)\eta$	16.7
$\eta' \to \pi^0 \pi^0 (\eta)$	28.8
$\eta' \to \gamma\gamma$	2.3

Table 4.2: Combined branching ratios for $\eta' \to (\pi^0 \pi^0)\eta$, $\eta' \to \pi^0 \pi^0 (\eta)$ and $\eta' \to \gamma\gamma$, including the branching ratios for $\pi^0 \to \gamma\gamma$ and $\eta \to \gamma\gamma$ [15]. The errors are omitted.

Regardless of reconstruction method, there is still background under the $\eta' p$ peak, that needs to be removed. This process is explained in more detail in 4.1.4.

4.1.4 Background subtraction

The background below the $\eta' p$ peak seen in figure 4.8 is subtracted using simulated data. All relevant background channels are simulated and put through the same analysis as the real data. To get the relative ratios between the different backgrounds right, each channel is scaled with an individual parameter

$$S' = \frac{\sigma(E_{\text{ref}}) \cdot \epsilon(E_{\text{ref}})}{\sigma_{\text{sum}}}, \tag{4.1}$$

where $\sigma(E_{\text{ref}})$ is the total cross section for the specific background channel, $\epsilon(E_{\text{ref}})$ is the reconstruction efficiency for the background channel and σ_{sum} is the reconstruction efficiency weighted sum of all background channel cross sections. E_{ref} refers to the beam energy at which the parameters are determined. For most background channels this is 1 400 MeV, since this energy is sufficiently below the $\eta' p$ threshold, such that the real data is free from any $\eta' p$ events. Some background reactions have a threshold higher than 1 400 MeV. These are scaled according to their parameters at their threshold. Values from all reference points are added together for σ_{sum} to make the fitting routine easier, even though they are at different beam energies. This inconsistency is resolved later in the fit.
Table 4.3 shows the S' values for all analyzed background channels for the different reconstruction methods. $2 \cdot 10^8$ events are simulated for each reaction. Multi-pion backgrounds are composed of all possible combinations of charged and uncharged pions, with $2 \cdot 10^8$ events simulated for each combination.
Not all backgrounds are used for every η' decay channel, since the reconstruction of η' decay products highly suppresses certain reactions. If S' is below 0.01, meaning that this channel contributes less than 1% to the background, it is not used in the fit. This is done to help the fitting routine, since there are fewer free parameters.
As mentioned in table 4.3, some cross sections are only estimated. Any inconsistencies arising from these estimates are resolved later in the fit.
Table 4.3 already nicely demonstrates how performing an increasingly more exclusive reconstruction removes backgrounds until only two are left. It also shows that the dominant backgrounds are multi-pion and π^0-η backgrounds, while the meson and strangeness channels only play a small role for the more inclusive methods.
S' takes care of the relative weight of the different backgrounds. By using

$$S = \frac{N_{\text{real}}(E_{\text{ref}})}{N_{\text{sim}}(E_{\text{ref}})} \cdot S', \tag{4.2}$$

the backgrounds are scaled such that the initial sum of all backgrounds agrees to the real data at 1 400 MeV. $N_{\text{real}}(E_{\text{ref}})$ is the number of real data events at E_{ref} and $N_{\text{sim}}(E_{\text{ref}})$ is the number of events for the respective background channel.
The fit varies the initial S scaling parameters of each background in 1000 steps. At each step the scaling parameters can be decreased or increased by 0.033 %. The direction that improves the agreement in the

Reaction channel	source	$\eta' \to X$	$\eta' \to (\pi^0\pi^0)\eta$	$\eta' \to \pi^0\pi^0(\eta)$	$\eta' \to \gamma\gamma$
$2\pi p$	[43]	0.2035	0.2879	0.0000	0.8784
$3\pi p$	[44]	0.2335	0.3231	0.0011	0.0000
$4\pi p$	[44]	0.1269	0.0374	0.0644	0.0000
$5\pi p$	[44]	0.1951	0.0044	0.5799	0.0000
$\eta\pi^0 p$	[45]	0.0266	0.0110	0.0122	0.1216
$\eta\pi^0\pi^0 p$	[45]	0.0895	0.3319	0.3401	0.0000
ηp	[29]	0.0001	0.0000	0.0000	0.0000
ωp	[46]	0.0056	0.0000	0.0000	0.0000
ρp	[43]	0.0861	0.0022	0.0000	0.0000
ϕp	[47]	0.0029	0.0000	0.0008	0.0000
$K^0\Sigma^+$	[48]	0.0033	0.0022	0.0000	0.0000
$K^+\Lambda^0$	[49]	0.0017	0.0000	0.0000	0.0000
$K^+\Lambda(1405)$	[50]	0.0052	0.0000	0.0008	0.0000
$K^+\Lambda(1520)$	[51]	0.0009	0.0000	0.0000	0.0000
$K^+\Sigma^0$	[49]	0.0072	0.0000	0.0000	0.0000
$K^+\Sigma(1385)$	[50]	0.0117	0.0000	0.0004	0.0000

Table 4.3: Relevant backgrounds for a fit with simulated data to the real data for the different reconstruction methods, including the respective S' values. If the numbers do not add up to one, this is due to rounding errors. If S' is green that channel is used for the specific reconstruction. Channels colored red are not used.
The cross section for $\eta\pi^0\pi^0$ is estimated to be slightly lower than that of $\eta\pi^0$. Cross sections for $4\pi p$ and $5\pi p$ are extrapolated to $1\,400\,\text{MeV}$ from the lowest available beam energy in [44] assuming the ratio to $3\pi p$ stays roughly the same. The cross section for ϕp is taken at $1\,700\,\text{MeV}$, while $K^+\Lambda(1405)$ and $K^+\Sigma(1385)$ cross sections values are taken at threshold. For $K^+\Lambda(1520)$ the cross section at $1\,738\,\text{MeV}$ is used, averaged from the differential cross sections. All inconsistencies arising from these extrapolations will be resolved later in the fit.

sidebands from $1\,304\,\text{MeV}$ to $1\,437\,\text{MeV}$ and $1\,597\,\text{MeV}$ to $1\,797\,\text{MeV}$ is chosen. Thus a maximum change of the initial S value of $33\,\%$ can be achieved.

The variations of the initial S values ensure the best agreement between the fit and real data, by accounting for a few effects: firstly some backgrounds are scaled with their parameters at a higher value than $1\,400\,\text{MeV}$. Furthermore, as mentioned in table 4.3 some background cross sections are only roughly estimated. Additionally S is based on the total cross sections for the background channels, while the fits are performed in different angular bins. Thus ideally the differential cross sections should be used.

The basic fitting algorithm code was written by Georg Scheluchin [52] and expanded on for this work.

4.1.5 Cross section

The differential cross section is determined using

$$\frac{d\sigma}{d\Omega} = \frac{N_{\eta' p}}{\Delta\Omega \cdot \rho_{\text{target}} \cdot \epsilon \cdot F_\gamma}, \tag{4.3}$$

where $N_{\eta'p}$ is the number of reconstructed $\eta'p$ events, $\Delta\Omega$ is the solid angle, $\rho_{\text{target}} = 2.53 \times 10^{-7}\,\mu\text{b}^{-1}$ is the target area density, ϵ is the reconstruction efficiency associated with the specific η' reconstruction and F_γ the flux.

The reconstruction efficiency is determined by simulating $\eta'p$, reconstructing the events through the same analysis as the real data and dividing the number of reconstructed events by the number of simulated events for every energy/$\cos(\Theta_{\eta'}^{\text{CMS}})$ bin. This is done for each analyzed η' decay channel individually.

4.1.6 Statistical and systematic uncertainties

The statistical errors $\Delta^{\text{stat}}\frac{d\sigma}{d\Omega}$ for each cross section data point are determined using

$$\Delta^{\text{stat}}\frac{d\sigma}{d\Omega} = \frac{\sqrt{\sqrt{N_{\text{after subtraction}}}^2 + (\frac{\sqrt{\chi^2}}{N_{\text{real data}}} \cdot N_{\text{after subtraction}})^2}}{\Delta\Omega \cdot \rho_{\text{target}} \cdot \epsilon \cdot F_\gamma}, \tag{4.4}$$

where $N_{\text{after subtraction}}$ is the number of events left after background subtraction, χ^2 is the summed in quadrature difference between the fit and the real data in all sideband bins and $N_{\text{real data}}$ is the sum of all real data entries in the sidebands. The parameters in the denominator are the same as in equation 4.3. For a well working fit the statistical error is dominated by its first component.

The systematic errors are composed of multiple components, that are all a constant fraction of the extracted differential cross section.

Table 4.4 shows the systematic errors stemming from the experimental side. These errors are independent of which analysis is used and are taken from [53]. For more details on the determination of the errors see the reference.

Source	% error
Beam spot alignment	4.0
Flux	4.0
SciFi2 efficiency	3.0
Target wall contribution	2.0
Track time selection	2.0
Target length	1.7
ToF efficiency	1.5
MOMO efficiency	1.0
Drift chamber efficiency	1.0
Beam energy calibration	1.0
Modeling of hardware triggers	1.0
Forward track geometric selection	1.0
Summed in quadrature	7.7

Table 4.4: Systematic uncertainties from the experiment, which apply to all analysis methods, and their sum. [53]

Additionally there are errors related to the different reconstruction methods. These are determined by

swapping each 2σ cut with a 1σ cut and vice versa, while all $\frac{1}{2}\sigma$ cuts are changed to 1σ cuts. The same analysis is performed with the new cuts and the yield from real data is divided by the yield from simulated $\eta'p$. This ratio is compared to the ratio with the original cuts and the percentage difference is taken as the systematic uncertainty. The values for these errors are shown in table 4.12 in subsection 4.3.3.

Furthermore there are systematic errors on the modeling of the backgrounds. These errors can be estimated by looking at the difference between the results from this work and the EtaMAID results [34, 54], using

$$\Delta_{\text{bg}}^{\text{sys}} \frac{d\sigma}{d\Omega} = \frac{\sqrt{\Delta}}{\frac{d\sigma}{d\Omega}_{\text{this work}}}, \tag{4.5}$$

where Δ is the summed in quadrature difference between results from this work and the average of the two EtaMAID parametrizations with and without a narrow resonance included, and $\frac{d\sigma}{d\Omega}_{\text{this work}}$ is the result from this work. These errors indicate how well the background is extrapolated from the sidebands to the signal region. Naturally, they will increase if the results from this work show a bigger discrepancy to the EtaMAID parametrizations.

The resulting systematic uncertainties due to the background description are shown in table 4.13 in subsection 4.3.3.

4.2 Reconstruction results

In this section the specifics of the four different reconstruction methods are explained. Angular resolutions, reconstruction efficiencies and differential cross sections are shown.

4.2.1 $\eta' \to X$

$\eta' \to X$ is the totally inclusive reconstruction, where only the recoil proton is detected in the forward spectrometer. With the proton reconstructed, the missing mass to the proton $m_{\text{miss, }p}$ can be calculated using

$$m_{\text{miss, }p} = \sqrt{\left(p_\gamma + p_{\text{target}} - p_p\right)^2}, \tag{4.6}$$

where p_γ is the four-momentum of the initial photon, p_{target} is the four-momentum of the target proton (i.e. a proton at rest) and p_p is the reconstructed four-momentum of the proton in the forward spectrometer.

For a two-body reaction $m_{\text{miss, }p}$ corresponds to the missing particle, e.g the η' for $\eta'p$. This gives, within the resolution, a sharp peak in the missing mass spectrum. The missing mass spectra for multi-body reactions are washed out, since the missing mass does not correspond to a single particle and arbitrary kinetic energies are involved. For a multi-body reaction cutting in the missing mass spectrum thus selects a specific kinematic range. For this range, there is only a specific range in beam energy, where the proton can hit the forward spectrometer. This results in a peak like structure, that can be seen in figure 4.10, which shows the spectrum from figure 4.8 with a missing mass cut around

the η' mass. As can be seen a proper fit to the background is no longer possible, since signal and background can not be distinguished. Thus no cut on the missing mass is applied.
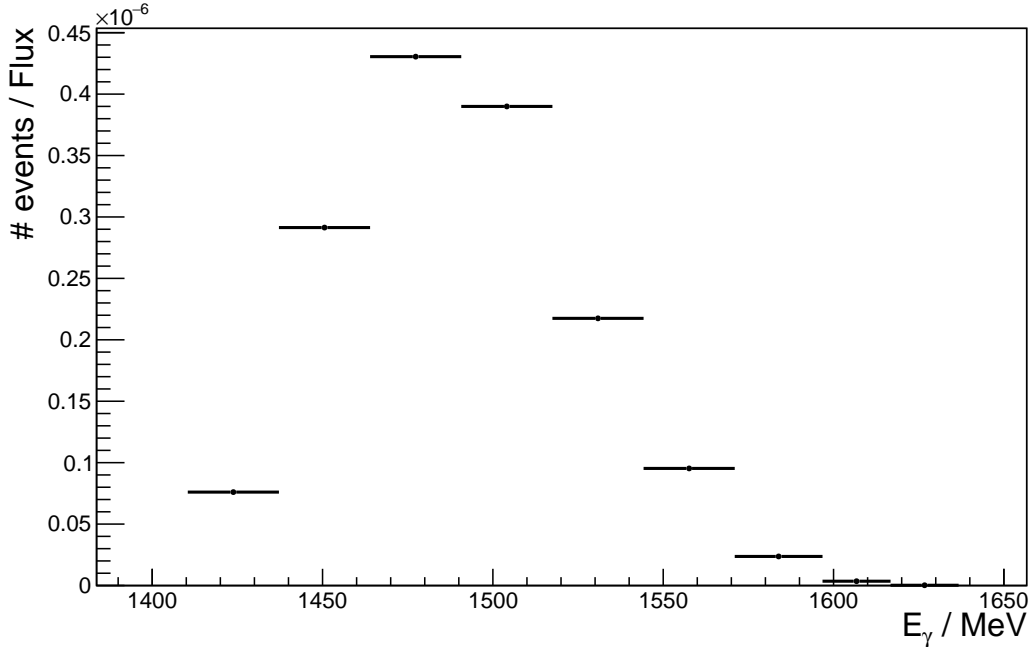

Figure 4.10: Number of protons in the forward spectrometer per Tagger energy bin normalized by the integrated flux and including a cut on the missing mass to the proton $940\,\mathrm{MeV} < m_{\mathrm{miss},\,p} < 980\,\mathrm{MeV}$.

Once all background has been removed from under the signal peak, the differential cross sections can be determined. Since these depend on the angles of the η' in the CMS, $\cos(\Theta_{\eta'}^{\mathrm{CMS}})$, it is crucial to know the resolution of $\cos(\Theta_{\eta'}^{\mathrm{CMS}})$. It depends on Θ_p^{lab}, the proton momentum and the beam energy E_γ. While Θ_p^{lab}- and momentum resolution are constant over the acceptance of the forward spectrometer and in the chosen momentum range, this is not necessarily the case for the $\cos(\Theta_{\eta'}^{\mathrm{CMS}})$ resolution. To determine this resolution, $\eta' p$ events are simulated and put through the same analysis as the real data. Subsequently the difference $\Delta\cos(\Theta_{\eta'}^{\mathrm{CMS}})$ between the measured and the generated $\cos(\Theta_{\eta'}^{\mathrm{CMS}})$ is determined as a function of $\cos(\Theta_{\eta'}^{\mathrm{CMS}})$ for each analyzed Tagger energy bin, shown in figure 4.11. As can be seen from figure 4.11 most of these distributions are not gaussian. Those distributions at the edges of the $\cos(\Theta_{\eta'}^{\mathrm{CMS}})$ range are highly asymmetric, since the difference in one direction is limited by the $\cos(\Theta_{\eta'}^{\mathrm{CMS}})$ range. Distributions from the center are more symmetric. For higher beam energies these distributions develop a plateau-like structure, see the green distribution in figure 4.11, as a result of the not perfect proton momentum correction. As mentioned before, events going forward and backward in the CMS can not be properly distinguished in a certain overlap region, see figure 4.4. Hence the same correction has to be applied to all events, leading to a slightly incorrect momentum and the observed plateau in figure 4.11.
Thus the standard deviation of the distribution is used as a measure for the resolution. Figure 4.12 shows the such determined resolution and the number of reconstructed events, each as a function of
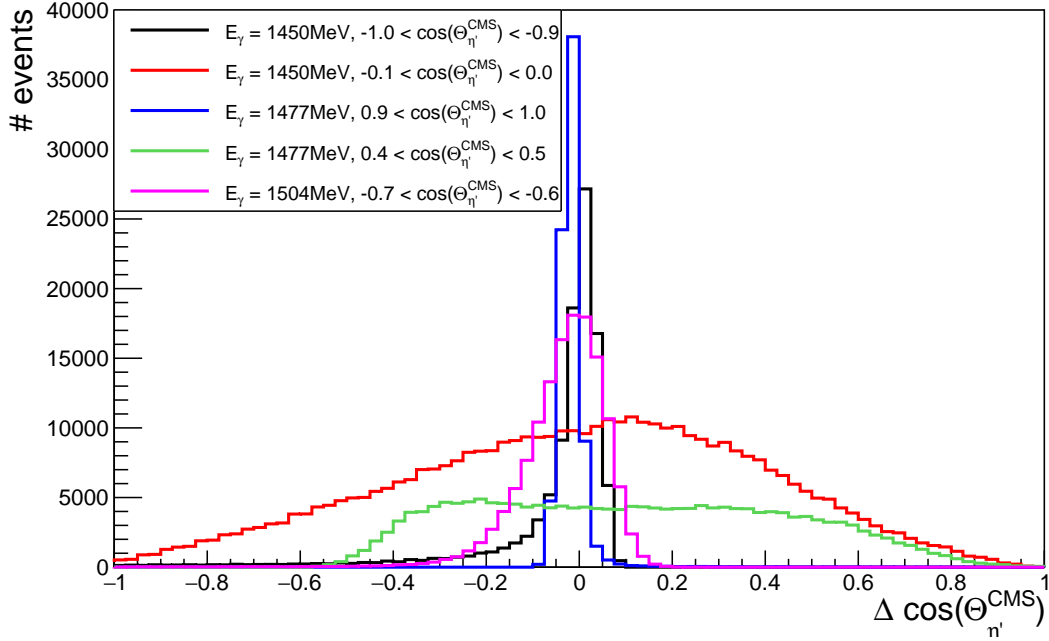
Figure 4.11: Exemplary differences $\Delta\cos(\Theta_{\eta'}^{CMS})$ between measured and generated $\cos(\Theta_{\eta'}^{CMS})$ for different $\cos(\Theta_{\eta'}^{CMS})$ and E_γ for $\eta' \to X$. The respective beam energy and angular range are given in the legend.
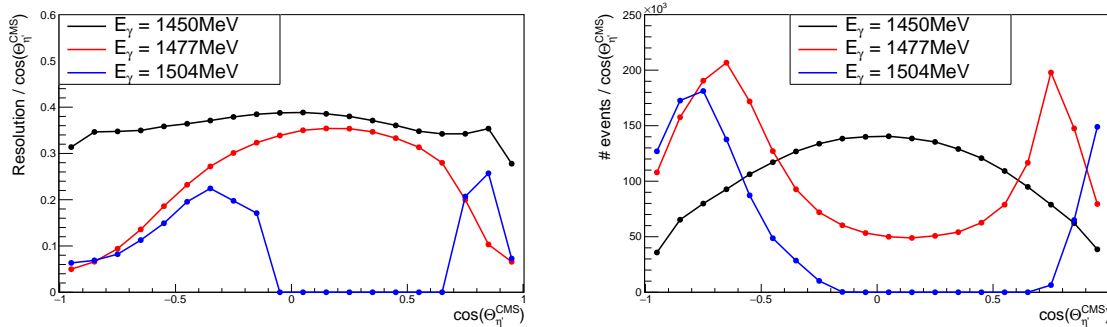
$\cos(\Theta_{\eta'}^{CMS})$.

Figure 4.12: Resolution (left) and number of events (right) as a function of $\cos(\Theta_{\eta'}^{CMS})$ for $\eta' \to X$. Entries at zero for the 1504 bin are a result of the momentum correction.

The resolution in the 1450 bin is roughly constant over $\cos(\Theta_{\eta'}^{CMS})$, while the number of detected events is highest in the central region. Protons going in forward or backward direction, which corresponds to the η' going in the opposite direction, have very little momentum perpendicular to the beam axis and therefor a small lab angle. As a result they are likely to hit the small hole in the center of the forward spectrometer, where the photon beam passes.

In the 1477 bin the resolution shows a clear peak for central $\cos(\Theta_{\eta'}^{CMS})$ values. Figure 4.3 demon-

strates, that in this region different $\cos(\Theta_{\eta'}^{\text{CMS}})$ lead to very similar Θ_p^{lab}, smearing out the resolution. Furthermore the figure shows, that lab angles in the central region can get larger than the vertical acceptance of the forward spectrometer, which leads to the decrease in the number of events seen in figure 4.12 on the right.

The gap in measurable momentum seen in figure 4.6 translates into a gap in the $\cos(\Theta_{\eta'}^{\text{CMS}})$ range for the 1504 bin. The resolution decreases at the edges of this gap, since the events in the center usually responsible for the ambiguities, are now removed. As for the 1477 bin, events in the central regions can have lab angles higher than the acceptance of the forward spectrometer. Due to the higher beam energy this effect is more pronounced, leading to a larger reduction of events than for the 1477 bin.

The $\cos(\Theta_{\eta'}^{\text{CMS}})$ bins are created such, that their size is equal to twice the weighted average resolution over the range of the bin, where the weight is the number of events per $\cos(\Theta_{\eta'}^{\text{CMS}})$. This weighting is performed to ensure that a few events with a poor resolution do not increase the bin size too much. Table 4.5 shows the resulting bin borders. As expected from figure 4.12 the bins get wider towards the center of the $\cos(\Theta_{\eta'}^{\text{CMS}})$ range.

Energy bin							
1450	-1.0	-0.286	1.0				
1477	-1.0	-0.898	-0.744	-0.414	0.300	0.820	1.0
1504	-1.0	-0.870	-0.714	-0.454	-0.038	0.650	0.966	1.0

Table 4.5: Borders of the $\cos(\Theta_{\eta'}^{\text{CMS}})$ bins for the different energy bins for $\eta' \rightarrow X$.

This binning in $\cos(\Theta_{\eta'}^{\text{CMS}})$ is much more coarse, than the one A2MAMI could achieve, seen in figure 2.3. Given that the angular resolution for the proton in forward direction is similar for A2MAMI and BGOOD ($\sigma_\Theta^{\text{A2MAMI}} < 1\,°$[55] and $\sigma_\Theta^{\text{BGOOD}} = 0.3\,°$[27]), this difference in CMS resolution must be a result of the resolution of the initial photon energy. Since the whole CMS angular range is boosted in a small lab angular range, changes in the determined energy of the initial photon, can have a large impact on the resulting lab angles.

The energy resolution at A2MAMI for the analyzed region is of the order of 2 MeV [56], while the Tagger at BGOOD provides an energy resolution of about 25 MeV in the region of interest [27]. To improve this, the ARGUS detector can be used in a future analysis. It covers the analyzed energy region and provides a resolution of about 7 MeV [27]. As a result a much finer binning in $\cos(\Theta_{\eta'}^{\text{CMS}})$ should be obtained.

The reconstruction efficiency is determined as mentioned in subsection 4.1.5, using these $\cos(\Theta_{\eta'}^{\text{CMS}})$ bins. The reconstruction efficiencies for all energy bins are shown in figure 4.13.

Since the reconstruction efficiencies are based on the number of measured events, they follow the patterns seen in figure 4.12 on the right. Not all details of those patterns are visible here, as the binning in figure 4.13 is more coarse than for figure 4.12. At best, a better than 80 % reconstruction efficiency is reached. As non of the η' decay products are observed this corresponds to the chance of identifying the proton in the forward spectrometer.

For the determination of the differential cross sections, the background needs to be subtracted from under the signal peak. Since the real data is normalized by the integrated flux, the simulated data
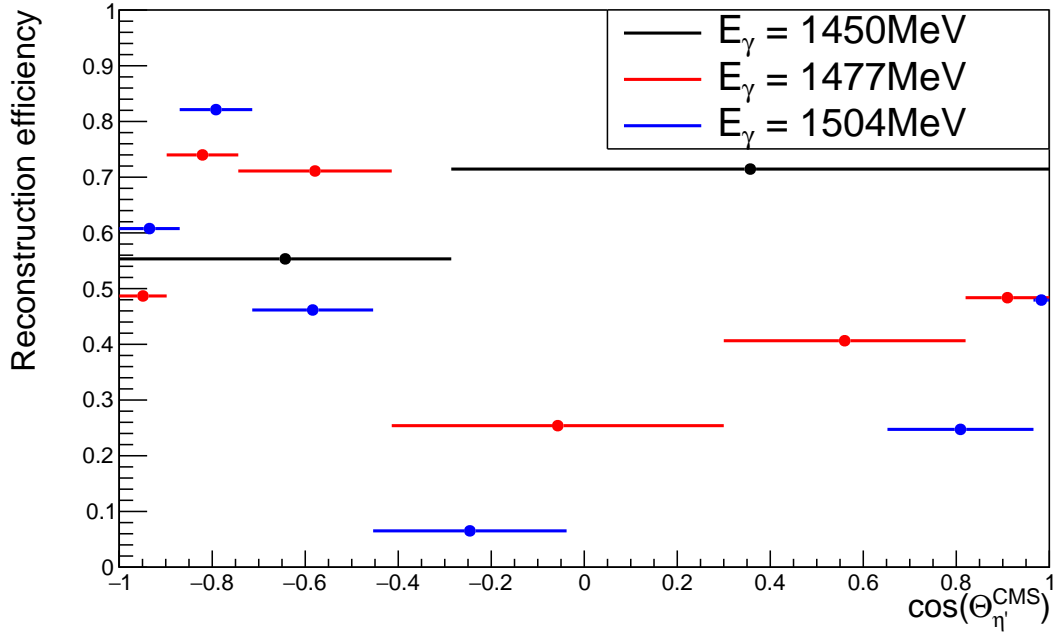
Figure 4.13: Reconstruction efficiencies for the different energy bins for $\eta' \rightarrow X$.

needs to be normalized by a realistic simulated flux as well, that contains all the properties of the real integrated flux. Since the heights of the simulated background contributions are fixed by the fit, see subsection 4.1.4, the absolute scale of this flux for the simulation is not important. What matters is the shape of the distribution.

This simulated flux is created by plotting the number of protons in the forward spectrometer per Tagger energy bin for all multi-meson background channels combined. These spectra are used, because they include the effects of the different sizes of the Tagger energy channels, as well as their respective efficiencies. Single-meson background channels are not taken into account, since their thresholds are too close to the fitting region and as a result they introduce spikes into the summed spectrum. The cut on the proton momentum is omitted, since proton momentum and photon energy are correlated and no photon energies should be cut away. Figure 4.14 shows the resulting flux for the simulation around the fitting region. As can be seen it exhibits similar properties to the real integrated flux shown in figure 4.7. The sudden drops in the spectrum due to changes in the Tagger geometry are present.

All contributing background channels are simulated, put through the same analysis as the real data and normalized as mentioned above. Table 4.3 shows all contributing backgrounds for this reconstruction method. They are fitted to the real data in the different angular bins over a photon energy range from 1 304 MeV to 1 797 MeV, using the technique mentioned in 4.1.4. To avoid any interference from $\eta' p$ the region from 1 437 MeV to 1 597 MeV is excluded from the fit. It includes the three analyzed energy bins, as well as three more energy bins containing a significant amount of $\eta' p$ events with the proton in the forward spectrometer.

Some exemplary fits are shown in figure 4.15 while all fits can be found in appendix A.1. As visible
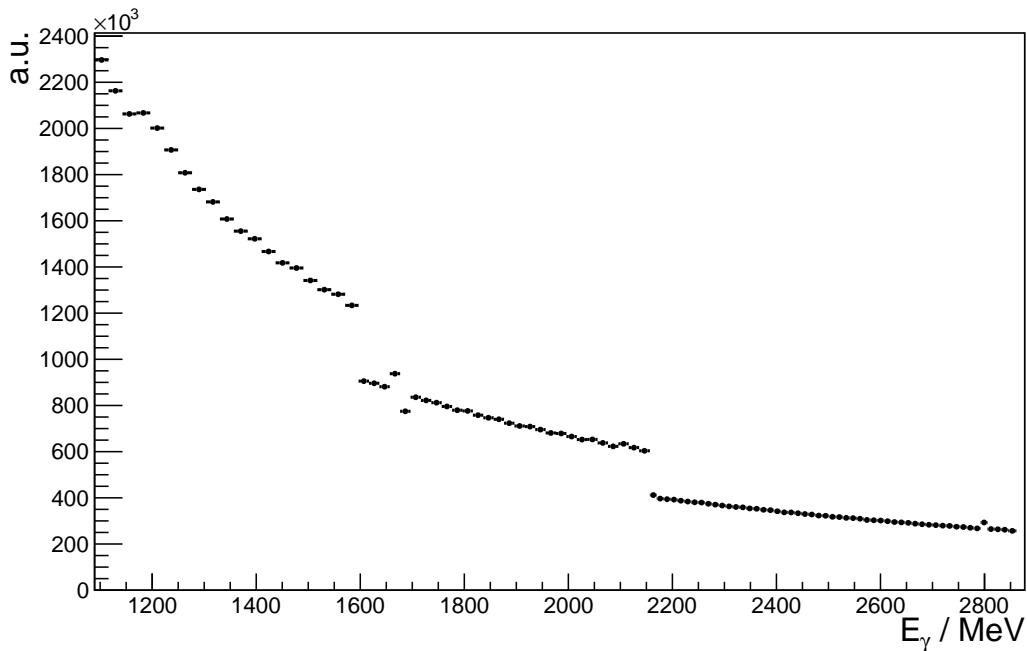
Figure 4.14: Flux created for the simulation by plotting the number of protons in the forward spectrometer per Tagger energy bin for all multi-meson background channels combined.

in the top right plot from figure 4.15, one energy bin in the signal region is well below the rest of all bins. This is a result of the proton momentum correction. It was only performed on the three analyzed energy bins and as shown before, changes the $\cos(\Theta_{\eta'}^{CMS})$ of events. Thus events are moved between different angular bins, leading to the dip seen in figure 4.15 on the right. Correspondingly an enhancement can be seen in the top left plot. If the proton momentum correction was also performed on all other energy bins, the spectra would appear more continuous again, as events in the sidebands would be moved to different angles as well. This can be done in a future analysis.

While this makes the spectra look less intuitive, it does not pose a problem for the fitting, since the simulated backgrounds are subject to the same correction and thus exhibit the same feature, see figure 4.15.

Within the statistical errors, there is a good agreement between the fit and the real data in the right sideband, especially for the more backward bins. The agreement in the left sideband is less good, as the fit under- or overestimates the real data, depending on the different angular bins. Possible reasons for this are a non-perfect flux normalization in the simulation as well as the missing of differential cross sections, as only phase space was used for the simulated backgrounds.

It should be noted, that the difference between the real data and the fit in each analyzed energy bin, directly gives the yield of $\eta' p$ events for that specific energy and angle. Thus a change of this difference of e.g. 10 %, directly results in a 10 % change of the cross section. As a result the cross section is very susceptible to small changes in the fit. This is already visible looking at the top two plots. They show the two angular bins for the 1450 cross section bin, and it can be seen, that the fits are higher than the real data, for the respective energy. Hence no cross section can be determined here.
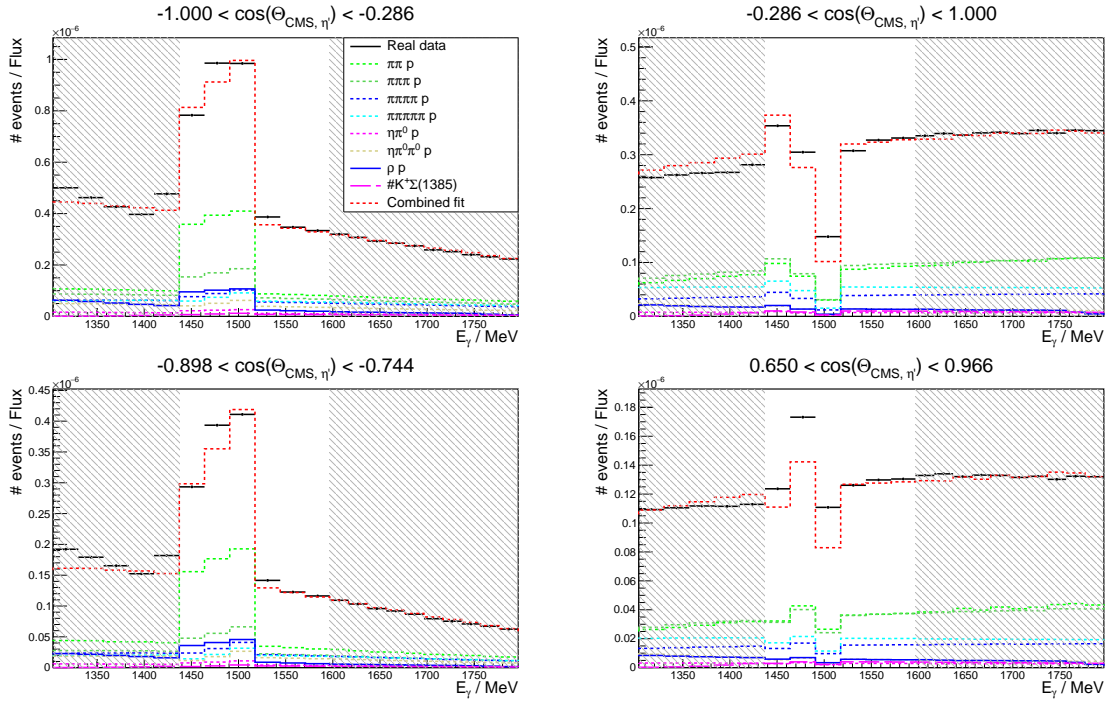
Figure 4.15: Exemplary fits for $\eta' \to X$: the shaded areas indicate the two sidebands. The respective $\cos(\Theta_{\eta'}^{\text{CMS}})$ bin is given in the title of each plot, while the legend is shown in the top left plot.

The background is subsequently subtracted using the simulated data fit. The differential cross sections for the different energy bins are determined using formula 4.3. The solid angle $\Delta\Omega$ is given by the size of the $\cos(\Theta_{\eta'}^{\text{CMS}})$ bins multiplied by 2π. The resulting cross sections are shown in figure 4.16. The formula for calculating the statistical error is given in subsection 4.1.6. The experimental systematic errors are given in table 4.4 in subsection 4.1.6, while the errors related to the reconstruction and background modeling are given in tables 4.12 and 4.13 in subsection 4.3.3.

As mentioned above there are no results for the 1450 energy bin, due to the fit overestimating the background. In the 1477 bin the results from this work do not agree to the two different EtaMAID parametrizations within the statistical errors and as a result the systematic errors are large. This disagreement increases at the edges of the $\cos(\Theta_{\eta'}^{\text{CMS}})$ range and is especially big for backwards going η'. Those correspond to protons going in forward direction in the CMS, which results in a very high momentum in the lab frame. The fact that the discrepancy worsens with increasing proton momentum indicates, that a correct proton momentum plays an important role in the description of the background under the signal. Hence the proton momentum correction needs to be understood in more detail. As previously mentioned, there are on-going efforts to make a proton momentum correction, that is reaction-independent and also takes into account the direction of the proton in addition to the absolute value of the momentum. With these corrections implemented the background description under the signal peak should improve.

The results in the 1504 bin are consistently too high as well. In addition some fits are not working due to the same issue mentioned for the 1450 bin. The gap between $\cos(\Theta_{\eta'}^{\text{CMS}}) \approx -0.1$ rad and 0.65 rad is
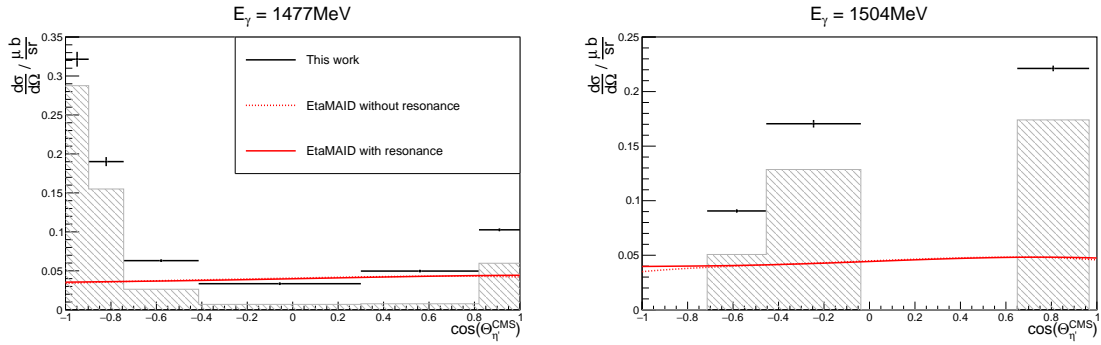
Figure 4.16: Resulting differential cross sections for $\eta' \to X$ (black data points) for the chosen energy bins as well as the corresponding EtaMAID parametrizations [34, 54] with and without the S_{11} (1900) included (solid and dashed red line, respectively). The error bars indicate the statistical errors, while the shaded areas show the systematic uncertainties. The missing cross section data points are due to the fit with simulated data being higher than the real data, see figure 4.15. The legend for both plots is shown in the left plot.

the acceptance gap already mentioned previously.

The statistical errors in the central region of the 1477 bin, where the agreement to EtaMAID is best, are of the necessary size to distinguish the two EtaMAID parametrizations. With further improvements concerning the background description, the systematic error, which is dominated by the error concerning the background modeling, will also reach a sufficient size.

Due to the large difference between results from this work and EtaMAID, the systematic errors are mostly large. The only exception being the fourth and fifth data point in the 1477 bin, which are close to EtaMAID.

These results already prove, that with a totally inclusive analysis of the $\eta' p$ channel, where just the proton is detected in the forward spectrometer, differential cross section results can be obtained over the full CMS angular range close to threshold. For higher energies an acceptance gap appears in the central region, which is a result of the physical acceptance of the forward spectrometer. This method is quite simple and it results in great statistics, that can be used to differentiate different EtaMAID parametrizations.

Nonetheless it turns out, that the background can not be accurately described at the moment. Since there is a sizeable amount of background below the signal, this limits the accuracy of this method. Thus it is crucial to remove more background from the real data, before attempting a fit to the background. This can be done by looking at a more exclusive reconstruction of the η'.

4.2.2 $\eta' \rightarrow \pi^0 \pi^0 \eta$

$\eta' \rightarrow \pi^0 \pi^0 \eta$ provides the possibility for a more exclusive analysis of $\eta' p$, by reconstructing some of the η' decay products. η' decays into this decay mode with a branching ratio of 0.224, while the π^0 and η decay into two photons with a 98.8 % and 39.3 % probability, respectively. As mentioned in subsection 4.1.3, this work will make use of these two photon decays to identify π^0 and η in the rugby ball.

This decay channel is first analyzed by only reconstructing the η ($\eta' \rightarrow (\pi^0 \pi^0)\eta$) and then by reconstructing the two π^0 ($\eta' \rightarrow \pi^0 \pi^0(\eta)$) which provides a higher degree of exclusiveness.

$\eta' \rightarrow (\pi^0 \pi^0)\eta$

In addition to the proton in the forward spectrometer at least two additional photons in the rugby ball are required. There is no cut on the type or number of decay particles coming from the two π^0.

All possible combinations of two photons are tried and if their combined invariant mass $m_{\text{inv}, \gamma\gamma}$ is within 2σ of the η mass peak, the photons are combined to η candidates by adding their four-momenta. If there are multiple candidates, the one with its invariant mass closest to the nominal η mass is chosen. If no suitable η candidate is found, the event is discarded. Figure 4.17 shows the invariant mass of all two photon combinations.
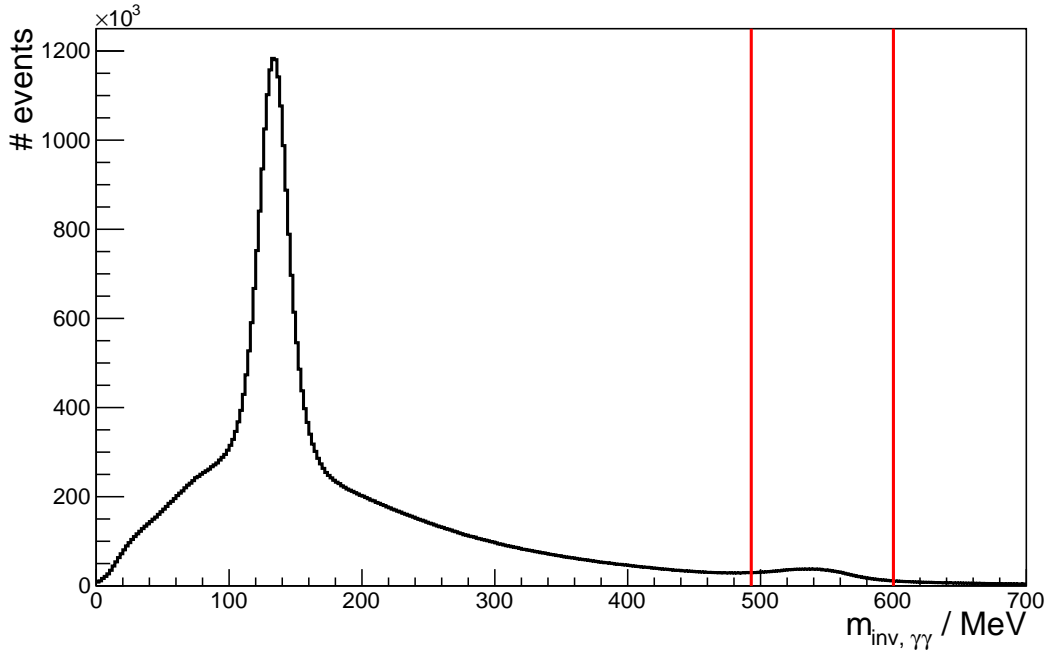
Figure 4.17: Invariant mass of two photons for $\eta' \rightarrow (\pi^0 \pi^0)\eta$. The red lines indicate the cuts applied to short target data.

As can be seen in figure 4.17, there is a prominent peak at the π^0 mass as well as a smaller peak at the η mass. This is to be expected, as requiring at least two photons does not cut away events where a single or multiple π^0 are produced freely. The background below the two peaks is combinatorical.

A cut is performed on the missing mass to the η-proton system, $m_{\text{miss},\,\eta p}$, to reduce background. $m_{\text{miss},\,\eta p}$ is given by

$$m_{\text{miss},\,\eta p} = \sqrt{\left(p_\gamma + p_{\text{target}} - p_p - p_\eta\right)^2}, \tag{4.7}$$

where p_γ is the four-momentum of the initial photon, p_{target} is the four-momentum of the target proton (i.e. a proton at rest), p_p is the reconstructed four-momentum of the proton in the forward spectrometer and p_η is the four-momentum of the reconstructed η. Figure 4.18 shows the $m_{\text{miss},\,\eta p}$ distribution for real data, simulated $\eta' p$ and simulations of the important backgrounds.
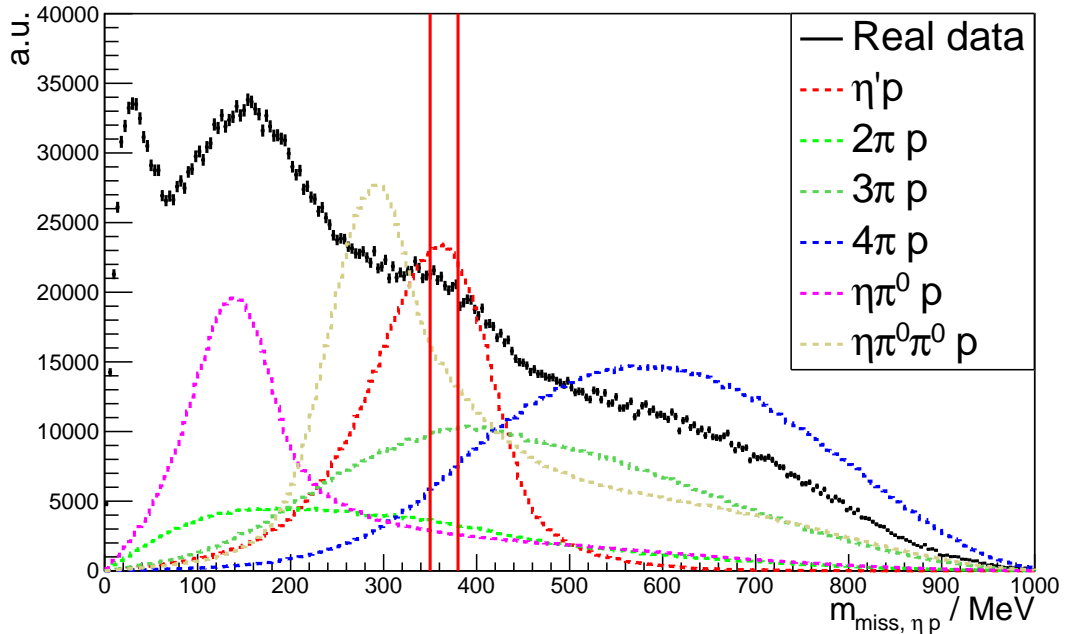
Figure 4.18: $m_{\text{miss},\,\eta p}$ for real and simulated data. The two solid red lines indicate the cut that was applied for the short target beam times. Distributions are scaled for better visibility, their relative heights do not represent their relative strength.

All backgrounds exhibit a peak in the $m_{\text{miss},\,\eta p}$ spectrum. This peak is smeared out for the multi-pion backgrounds, as they do not contain a proper η. Since none of those backgrounds peak around the same value as $\eta' p$ a cut can be placed on $m_{\text{miss},\,\eta p}$ to effectively reduce background. The S/N is determined by linearly extrapolating the background under the signal peak and dividing the peak integral by the background integral. This is done over the whole angular range. Different cuts on $m_{\text{miss},\,\eta p}$ are tried and the best S/N is achieved for an asymmetric $\frac{\sigma}{2}$ cut. σ and central value of the $\eta' p$ distribution are determined using a gaussian fit. Asymmetric meaning that the cut starts from the center of the $\eta' p$ distribution's peak towards higher $m_{\text{miss},\,\eta p}$. The different cut values and their respective S/N are shown in table 4.6.

As mentioned, this cut was chosen, since it provides the best S/N. Due to the difficulties in describing

Cut in σ	$\frac{1}{2}$	**1**	$\mathbf{\frac{3}{2}}$	**2**	$\frac{1}{2}$	$\frac{2}{3}$	1	2
S/N	0.90	0.77	0.57	0.48	0.75	0.68	0.59	0.40

Table 4.6: Different cut values for $m_{\text{miss},\,\eta p}$, given in σ of the $\eta' p$ peak. Cuts shown in bold are asymmetric.

the background, shown in subsection 4.2.1, the goal is to remove as much background as possible with this cut. In a future analysis with improved background description it can be loosened. Subsection 4.3.4 demonstrates the effects a more loose cut can have on the resulting statistics.

Figure 4.18 further shows, that the peak in $m_{\text{miss},\,\eta p}$ lies significantly above the two-π^0 mass for $\eta' p$. Thus the two π^0 must have a significant kinetic energy, larger than that of the π^0 from $\pi^0\pi^0\eta$ free production, whose peak is at a lower $m_{\text{miss},\,\eta p}$ value. This difference leads to differing angles between the η' decay products. Since the other backgrounds do not have the same final state as $\eta' p \to \pi^0\pi^0\eta p$, a difference in those angles compared to $\eta' p$ is also expected. Figure 4.19, shows the angles Ω (in the lab frame) between η and $m_{\text{miss},\,\eta p}$, η' and $m_{\text{miss},\,\eta p}$ as well as η' and η, after the cut to $m_{\text{miss},\,\eta p}$ has already been applied.
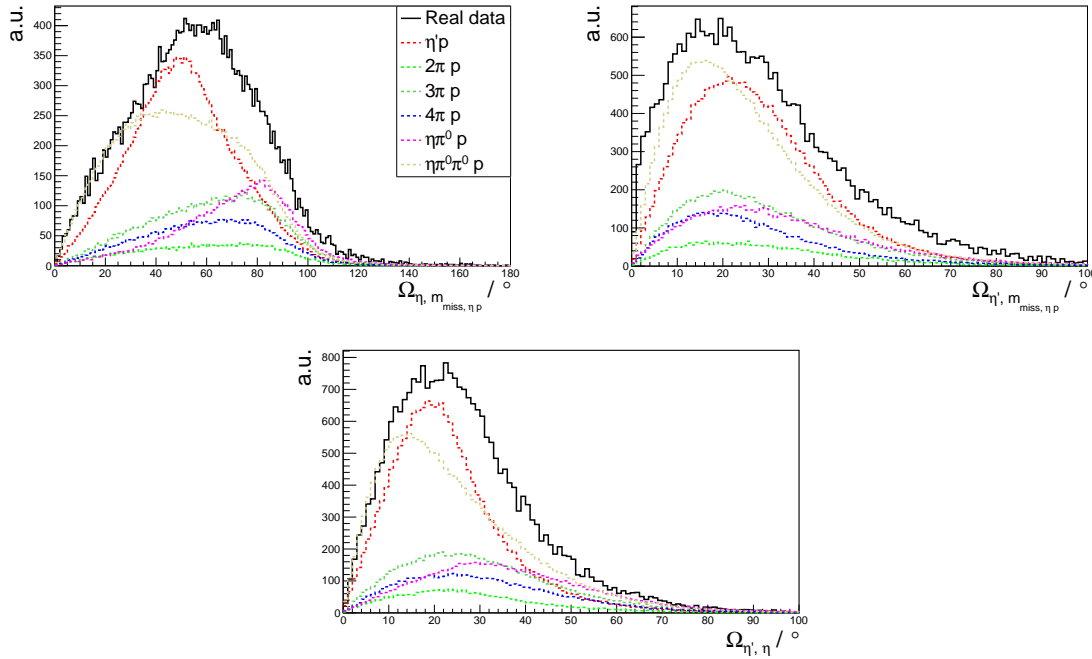
Figure 4.19: Angles Ω (in the lab frame) between η', η and $m_{\text{miss},\,\eta p}$. Distributions are scaled for better visibility, their relative heights do not represent their relative strength. The legend for all plots is given in the top left.

All three plots in figure 4.19, show peaking structures, where the distribution from $\eta' p$ peaks at different angles than the backgrounds. Henceforth these three angles can be used to further reduce background in a future analysis.

Due to changes in the reconstruction of the η', it can not be assumed that the resolution in $\cos(\Theta_{\eta'}^{CMS})$ stays the same as for $\eta' \rightarrow X$. Thus it is again determined, analogous to subsection 4.2.1. Figure 4.20 shows the resolution as well as the number of events as a function of $\cos(\Theta_{\eta'}^{CMS})$.
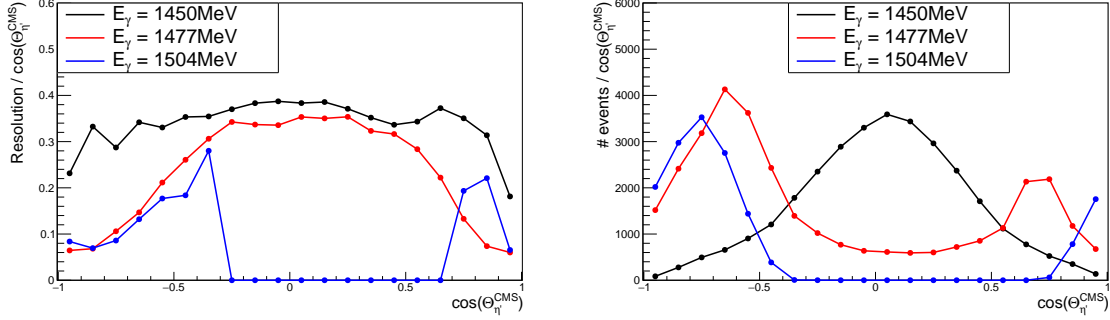
Figure 4.20: Resolution (left) and number of events (right) as a function of $\cos(\Theta_{\eta'}^{CMS})$ for $\eta' \rightarrow (\pi^0\pi^0)\eta$. Entries at zero for the 1504 bin are a result of the momentum correction.

The distributions look mostly similar to those seen in figure 4.12, except for the more forward peak in the number of events spectrum for the 1477 and 1504 bin. This is suppressed, since an η' in forward direction in the CMS has on average a smaller lab angle than one going backwards. As a result the η' decay products also have on average smaller angles and are thus more likely to hit the forward hole in the rugby ball.

Overall the curves are not as smooth as previously due to more limited statistics. Since the bin sizes are created by averaging the resolution this is not a problem. The resulting bins have slightly different sizes than the previously determined ones, but the number of angular bins for each energy bin does not change compared to the totally inclusive method. The resulting bin borders are shown in table 4.7.

Energy bin							
1450	-1.0	-0.262	1.0				
1477	-1.0	-0.868	-0.652	-0.172	0.508	0.872	1.0
1504	-1.0	-0.842	-0.656	-0.330	-0.106	0.650	0.952	1.0

Table 4.7: Borders of the $\cos(\Theta_{\eta'}^{CMS})$ bins for the different energy bins for $\eta' \rightarrow (\pi^0\pi^0)\eta$.

The reconstruction efficiencies for the different energy bins are calculated as mentioned in subsection 4.1.5 and shown in figure 4.21. Due to the necessity of reconstructing an η from two photons and the additional cut on $m_{\text{miss}, \eta p}$, the reconstruction efficiency is greatly reduced compared to the fully inclusive case, with the maximum lying below 1.5 %. As before the shape of the reconstruction efficiency mirrors the shape seen in figure 4.20 on the right.

The real data is fitted with simulated backgrounds using the method outlined in subsection 4.2.1, with the contributing background channels shown in table 4.3. The fit ranges from 1 304 MeV to 1 797 MeV, while the region from 1 437 MeV to 1 597 MeV is excluded. Some exemplary fits are shown in figure 4.22. All fits are found in appendix A.2.

For more backward angular bins there is a good agreement between the fit and the real data in the right sideband. In the left sideband the fit overestimates the background. For the more forward bins shown
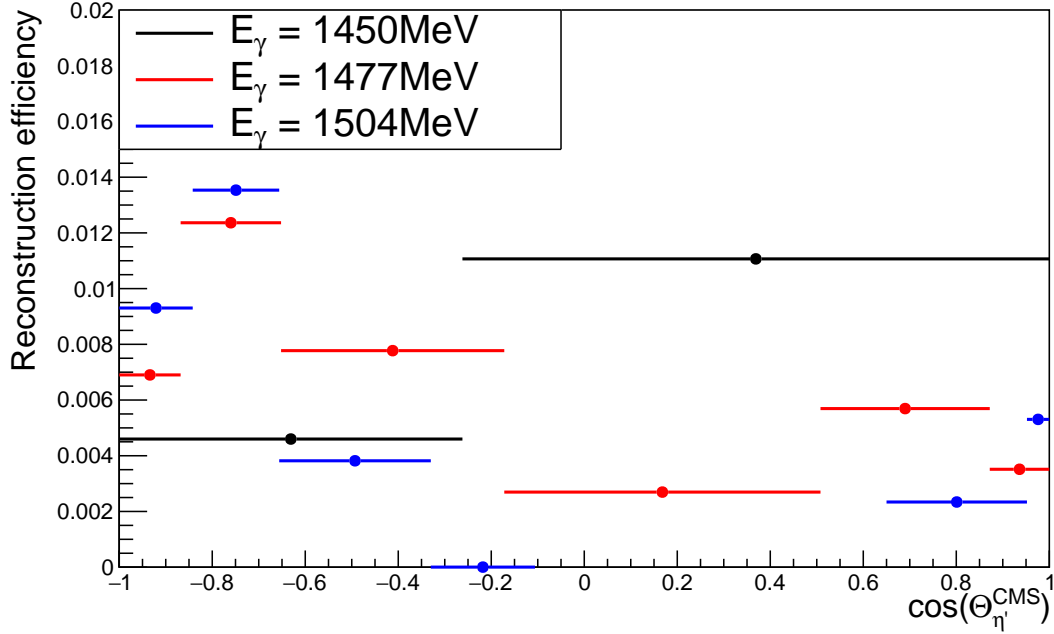
Figure 4.21: Reconstruction efficiencies for the different energy bins for $\eta' \to (\pi^0\pi^0)\eta$.

on the right, the agreement in the left sideband is better within the statistical errors, although the background is still overestimated. In the right sideband the fit strongly underestimates the real data. These discrepancies again are most likely a result of a non-perfect modeling of the background, which can be improved with a better normalization of the simulation, the addition of proper differential cross-sections to the simulation, as well as an improved proton momentum correction. A missing background channel is unlikely as all relevant reactions this close to threshold have been checked.

The background is subtracted using the simulated data fit and the differential cross sections for the different energy bins are determined using formula 4.3. They are shown in figure 4.23. The systematic errors can be found in subsection 4.3.3, while the statistical errors are calculated in the same way as for $\eta' \to X$, see equation 4.4 for details.

As can be seen most of the results from this thesis are significantly above the two EtaMAID parametrizations and do not agree within the statistical errors. Although the difference is smaller than for $\eta' \to X$. Furthermore the same pattern observed in figure 4.16 is visible, where the disagreement increases with more backward going η'. As mentioned in subsection 4.2.1, this is most likely a result of a slightly incorrect proton momentum. This is especially interesting, since those are the bins, where the agreement between simulation and real data is best in the sidebands, see figure 4.22. This indicates that the background, while working reasonably well in the sidebands, is not well modeled in the signal region.

The statistical errors are significantly bigger than the difference between the two EtaMAID parametrizations. Thus more data is needed to distinguish the two. This can be achieved by taking more data, but also through loosening the $m_{\text{miss},\eta p}$ cut. Due to the above-mentioned issues with the description
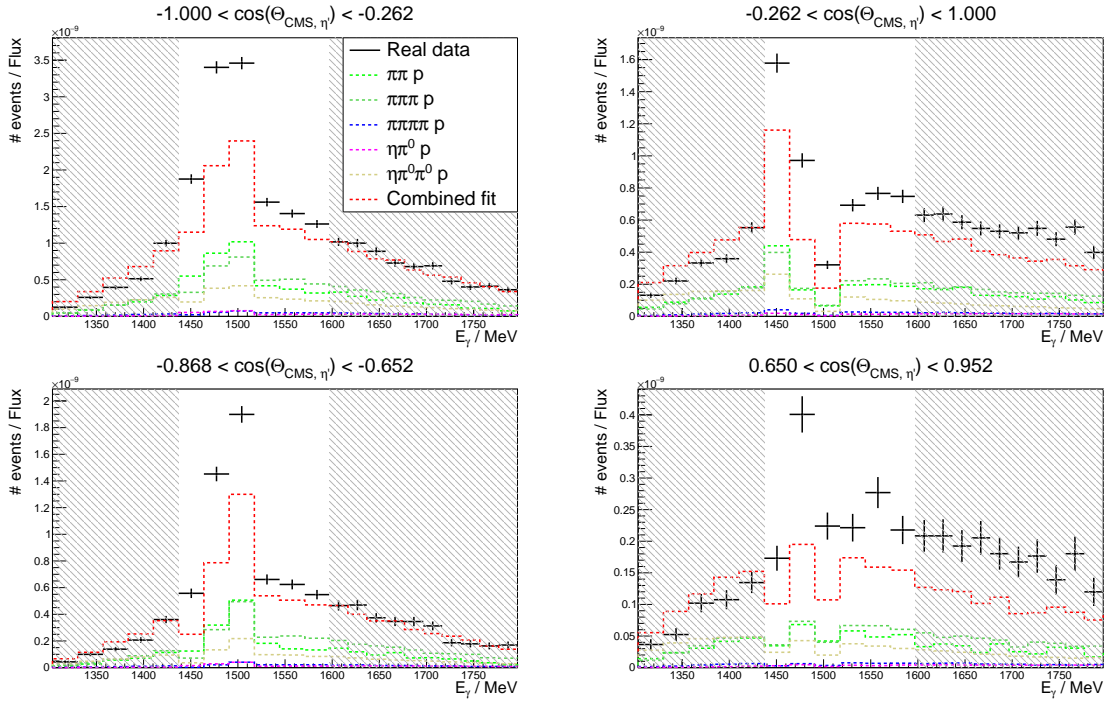
Figure 4.22: Exemplary fits for $\eta' \to (\pi^0\pi^0)\eta$: the shaded areas indicate the two sidebands. The respective $\cos(\Theta_{\eta'}^{\text{CMS}})$ bin is given in the title of each plot, while the legend is shown in the top left plot.

of the background, loosening the cut requires a better agreement between simulation and real data first. The statistical effects of additional data taking and a more loose cut are described in detail in subsection 4.3.4.

The second data point in the 1450 bin has errors closest to the difference between the two EtaMAID parametrizations. Unfortunately in this bin the average difference between the two parametrizations is roughly zero.

Due to the large difference between results from this work and EtaMAID, the systematic errors are mostly large. The only exception being the second data point in the 1450 bin, which shows a good agreement.

Overall this reconstruction method proves, that by increasing the exclusiveness of the analysis, the agreement to EtaMAID can be improved. This is due to a reduction of the background, whose behavior under the η' peak is not fully understood. Thus an even more exclusive reconstruction is useful to further reduce the background. This is done by reconstructing the two π^0 from $\eta' \to \pi^0\pi^0\eta$ explicitly and reconstructing the η through the missing mass.
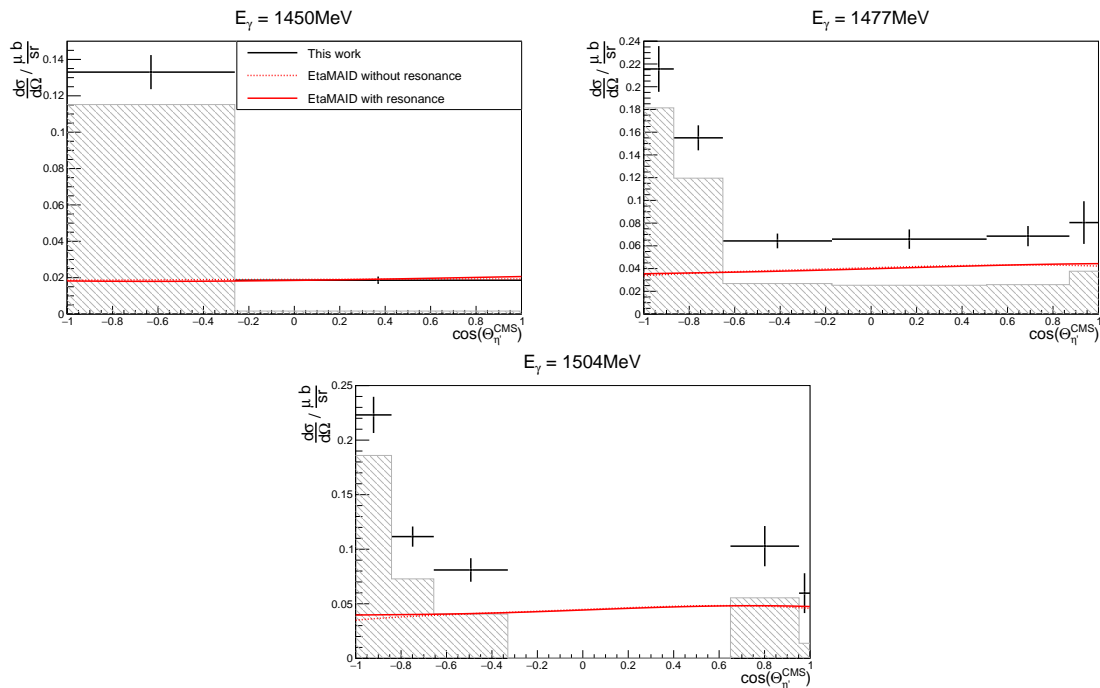
Figure 4.23: Resulting differential cross sections for $\eta' \to (\pi^0 \pi^0)\eta$ (black data points) for the chosen energy bins as well as the corresponding EtaMAID parametrizations [34, 54] with and without the S_{11} (1900) included (solid and dashed red line, respectively). The error bars indicate the statistical errors, while the shaded areas show the systematic uncertainties. The legend for all plots is shown in the left plot.

$\eta' \to \pi^0\pi^0(\eta)$

At least four photons are required to be detected in the rugby ball in addition to the proton in the forward spectrometer. There is no cut on the number or type of η decay products.

Two photons are combined to a π^0 candidate by adding their four-momenta and checking, that the invariant mass $m_{\text{inv}, \gamma\gamma}$ is within 2σ of the π^0 mass peak. This is done for all possible combinations of photons. All events with less than two π^0 candidates are discarded. If two or more π^0 candidates are found in an event, sets of two independent π^0 are created. Independent meaning, that no photon is used for both candidates at the same time. If no such set is found, the event is discarded. If more than one set is found, the set who's mass is overall closest to the nominal mass of two π^0 is taken. Figure 4.24 shows the invariant mass spectrum of two photons as well as the 2σ cut on $m_{\text{inv}, \gamma\gamma}$.
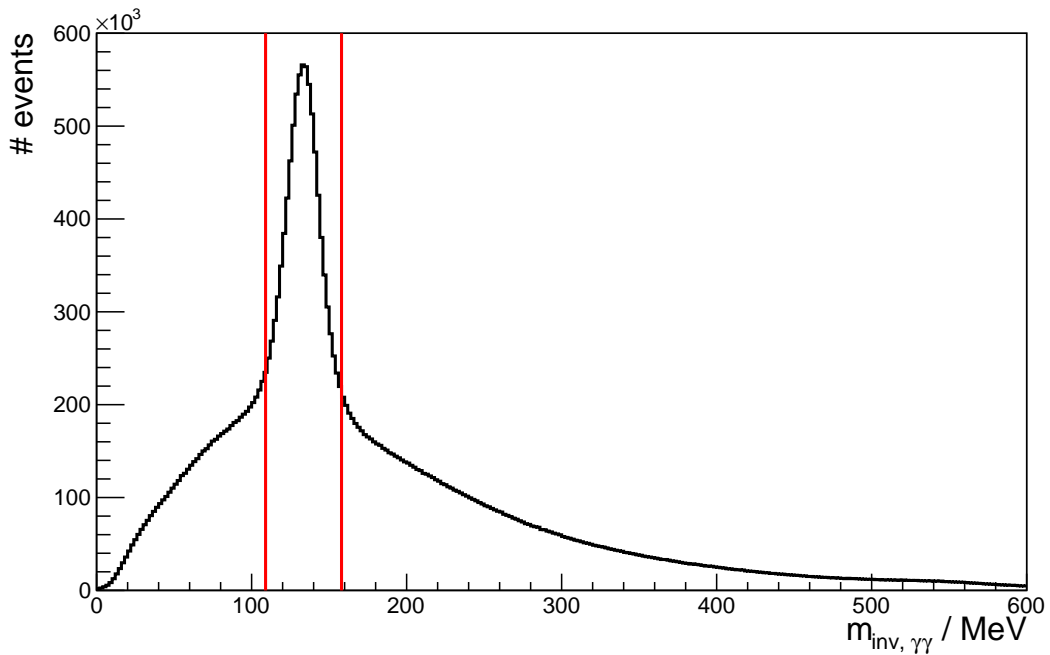
Figure 4.24: Invariant mass of two photons for $\eta' \to \pi^0\pi^0(\eta)$. The red lines indicate the cut values for the short target beam times.

As can be seen in figure 4.24 there is a clear π^0 peak on top of combinatorical background. In contrast to figure 4.17 the η peak is heavily suppressed as a result of the four-photon requirement.

To reduce background a cut is placed on the missing mass to the $\pi^0\pi^0 p$-system which is given by

$$m_{\text{miss}, \pi^0\pi^0 p} = \sqrt{\left(p_\gamma + p_{\text{target}} - p_p - p_{\pi_1^0} - p_{\pi_2^0}\right)^2},\tag{4.8}$$

where $m_{\text{miss}, \pi^0\pi^0 p}$ is the missing mass to the $\pi^0\pi^0 p$-system, p_γ is the four-momentum of the initial photon, p_{target} is the four-momentum of the target proton (i.e. a proton at rest), p_p is the reconstructed four-momentum of the proton in the forward spectrometer and $p_{\pi_{1/2}^0}$ are the reconstructed four-momenta

of the two π^0. Figure 4.25 shows the distribution of $m_{\text{miss}, \pi^0\pi^0 p}$ for real data, simulated $\eta'p$ and simulations of all relevant backgrounds.
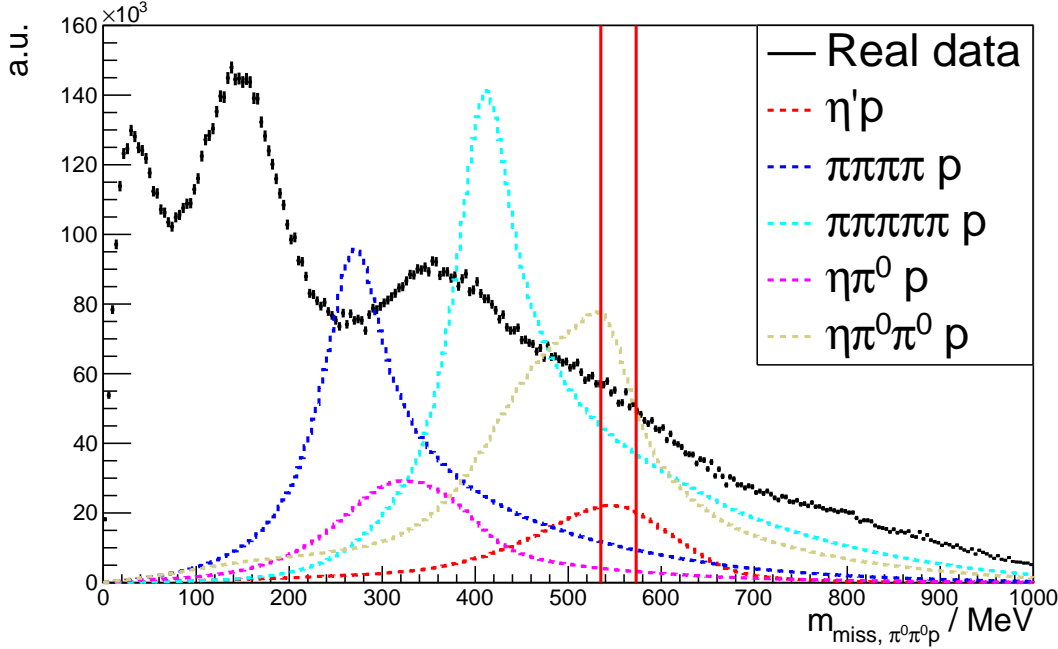
Figure 4.25: $m_{\text{miss}, \pi^0\pi^0 p}$ for real and simulated data. The two solid red lines indicate the cut, that was applied to the short target beam times. Distributions are scaled for better visibility, their relative heights do not represent their relative strength.

As expected all distributions show a peak in the $m_{\text{miss}, \pi^0\pi^0 p}$ spectrum. Since most backgrounds contain two π^0, the peaks are not as smeared out as they were for $m_{\text{miss}, \eta p}$, shown in figure 4.18. Most backgrounds peak far away from $\eta'p$, with the exception of $\eta\pi^0\pi^0 p$, which has the same final state. This makes reducing $\eta\pi^0\pi^0 p$ more difficult, but due to the more broad distribution and the slightly lower central value of the peak, it is still feasible.

The S/N is determined by linearly extrapolating the background under the signal peak and dividing the peak integral by the background integral. This is done over the whole angular range. Different cuts on $m_{\text{miss}, \pi^0\pi^0 p}$ were tried and the best S/N is achieved for an asymmetric $\frac{1}{2}\sigma$ cut. The different cut values and their respective S/N are shown in table 4.8.

Cut in σ	$\frac{1}{2}$	**1**	$\frac{3}{2}$	**2**	$\frac{1}{2}$	$\frac{2}{3}$	1	2
S/N	0.76	0.74	0.74	0.68	0.57	0.58	0.54	0.39

Table 4.8: Different cut values for $m_{\text{miss}, \pi^0\pi^0 p}$. Cuts shown in bold are asymmetric.

As for the previous analysis method the cut with the highest S/N is not necessarily the best, since it heavily reduces the available statistics. It was chosen, to get as clean of a data set as possible for this reconstruction method. In a future analysis, this cut can be loosened for better statistics, see subsection 4.3.4 for details.

The resolution and binning are determined analogous to the previous subsections. Figure 4.26 shows the resolution as well as the number of events as a function of $\cos(\Theta_{\eta'}^{CMS})$ while table 4.9 shows the resulting binning.
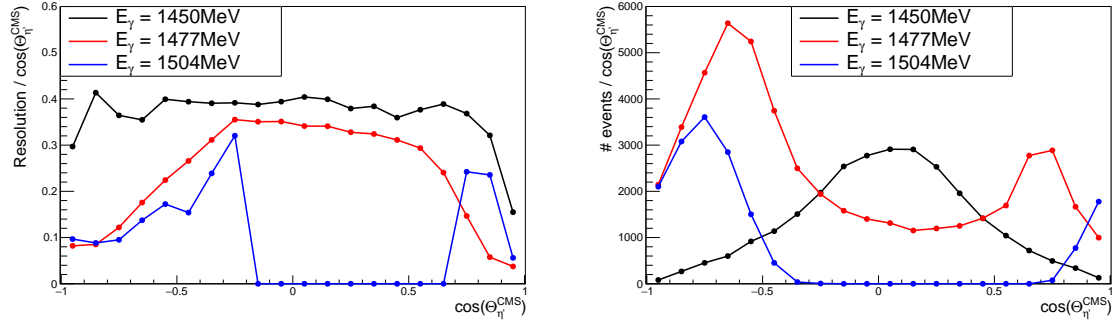
Figure 4.26: Resolution (left) and number of events (right) as a function of $\cos(\Theta_{\eta'}^{CMS})$ for $\eta' \rightarrow \pi^0\pi^0(\eta)$. Entries at zero for the 1504 bin are a result of the momentum correction.

The distributions shown in figure 4.26 show the same features already observed in figure 4.20, which is to be expected due to the same final state. There are again slight changes in the sizes of the angular bins, resulting in an additional $\cos(\Theta_{\eta'}^{CMS})$ bin for the 1504 energy bin.

Energy bin								
1450	-1.0	-0.174	1.0					
1477	-1.0	-0.832	-0.484	0.158	0.722	0.928	1.0	
1504	-1.0	-0.814	-0.580	-0.240	0.142	0.650	0.958	0.988	1.0

Table 4.9: Borders of the $\cos(\Theta_{\eta'}^{CMS})$ bins for the different energy bins for $\eta' \rightarrow \pi^0\pi^0(\eta)$.

Thereafter the reconstruction efficiency is determined, shown in figure 4.27. It follows the same pattern observed in figure 4.26 on the right, with the exception of the most forward data point of the 1504 bin. Since the $\cos(\Theta_{\eta'}^{CMS})$ bins in 4.26 are 0.1 wide, they are wider than the last $\cos(\Theta_{\eta'}^{CMS})$ bin of the 1504 energy bin in figure 4.27. Thus the drop in the number of events, leading to the drop in the reconstruction efficiency for the most forward data point of the 1504 bin, can not be seen in figure 4.26. In general the reconstruction efficiency increases slightly with respect to $\eta' \rightarrow (\pi^0\pi^0)\eta$, even though more photons are required in the rugby ball. This is because the π^0 decays into two photons with a 98.8 % probability [15] while the η only does so with a 39.3 % probability [15].

As in the previous sections, the simulated spectra are fitted to the real data from 1 304 MeV to 1 797 MeV, while excluding the region from 1 437 MeV to 1 597 MeV. Some exemplary fits are shown in figure 4.28. All fits are found in appendix A.3.
As can be seen, there is no good agreement between the simulated data fit and the real data within the statistical errors. In the right sideband the fit lies consistently below the real data, while it overestimates the background in the left sideband. This holds true for all angular bins. As mentioned for the previous analysis, improvements need to be made on the normalization of the simulation, as well as the proton
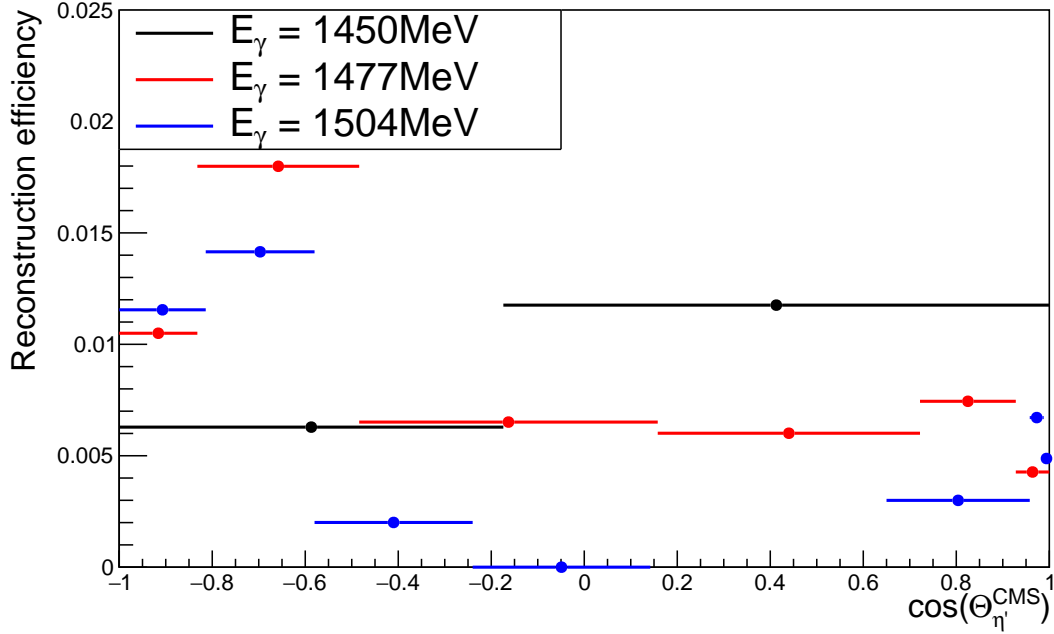
Figure 4.27: Reconstruction efficiencies for the different energy bins for $\eta' \to \pi^0\pi^0(\eta)$.

momentum correction. Furthermore proper differential cross sections can be included for the different backgrounds in the simulation.

Overall the agreement between simulation and real data is worse than for $\eta' \to (\pi^0\pi^0)\eta$, even though this reconstruction is more exclusive. This is likely a result of requiring two π^0, which has a higher reconstruction efficiency also for the background. Thus more background is reconstructed than for $\eta' \to (\pi^0\pi^0)\eta$.

After subtracting the background using the simulated data fit, the differential cross sections are determined, shown in figure 4.29. An explanation of the systematic errors is found in subsection 4.3.3, while the statistical errors are calculated using formula 4.4.

Even though the agreement between real data and the simulated data fit is worse, as shown in figure 4.28, the resulting cross sections show a better agreement to EtaMAID. This underlines the issue mentioned before, that the behavior of the background under the peak is not fully understood.

Again the discrepancy between the results from this work and the two EtaMAID parametrizations is highest for backward going η' in the CMS. This points to the proton momentum as a source of the discrepancy.

The statistical errors are of the same order as for $\eta' \to (\pi^0\pi^0)\eta$, meaning that they are significantly larger than any difference between the two EtaMAID parametrizations. Thus more data needs to be taken, or the cut on $m_{\text{miss}, \pi^0\pi^0 p}$ needs to be loosened. Subsection 4.3.4 describes the effects those two actions have on the available statistics in more detail.

The systematic errors in those bins, where there is an agreement between the results from this work and EtaMAID within the statistical errors, are small and of the order of the difference between the two
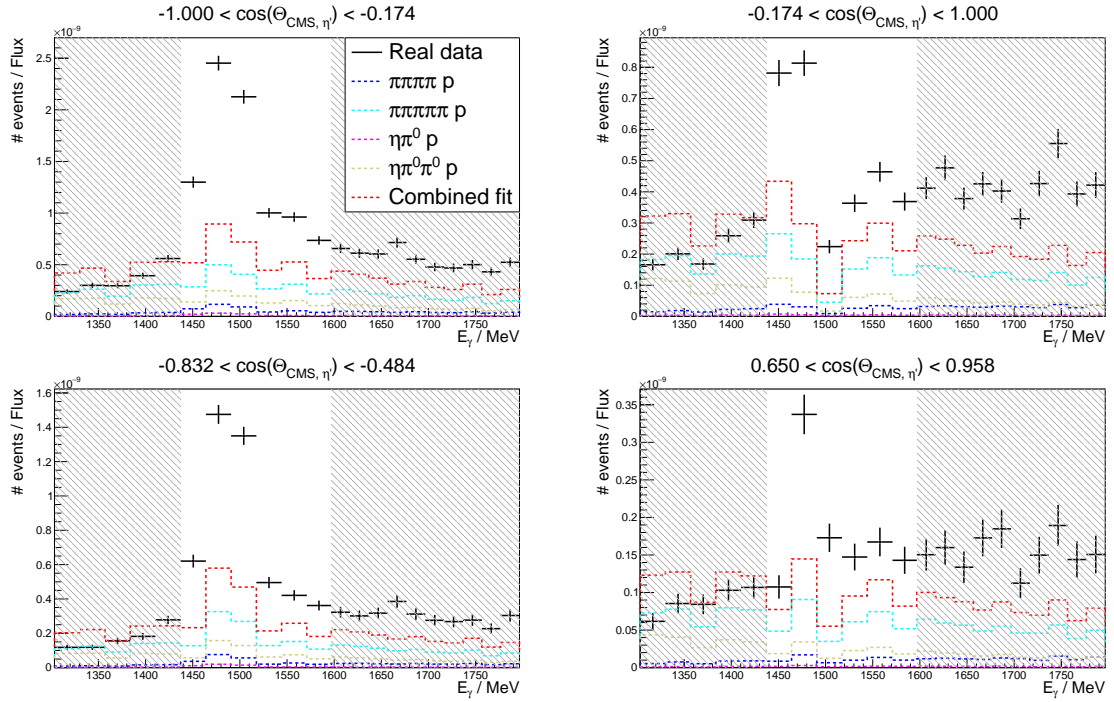
Figure 4.28: Exemplary fits for $\eta' \to \pi^0 \pi^0 (\eta)$: the shaded areas indicate the two sidebands. The respective $\cos(\Theta_{\eta'}^{CMS})$ bin is given in the title of each plot, while the legend is shown in the top left plot.

EtaMAID parametrizations. In the other bins, due to the large difference, the systematic errors are much larger.

This reconstruction method proves, that even by being more exclusive, the $\eta' \to \pi^0 \pi^0 \eta$ decay channel does not provide the necessary amount of background reduction to reproduce the two EtaMAID parametrizations. Thus the background needs to be removed as much as possible, which is achieved with the totally exclusive $\eta' \to \gamma\gamma$ reconstruction, where the η' is reconstructed directly from its two photon decay. This provides a very clean sample for the analysis.
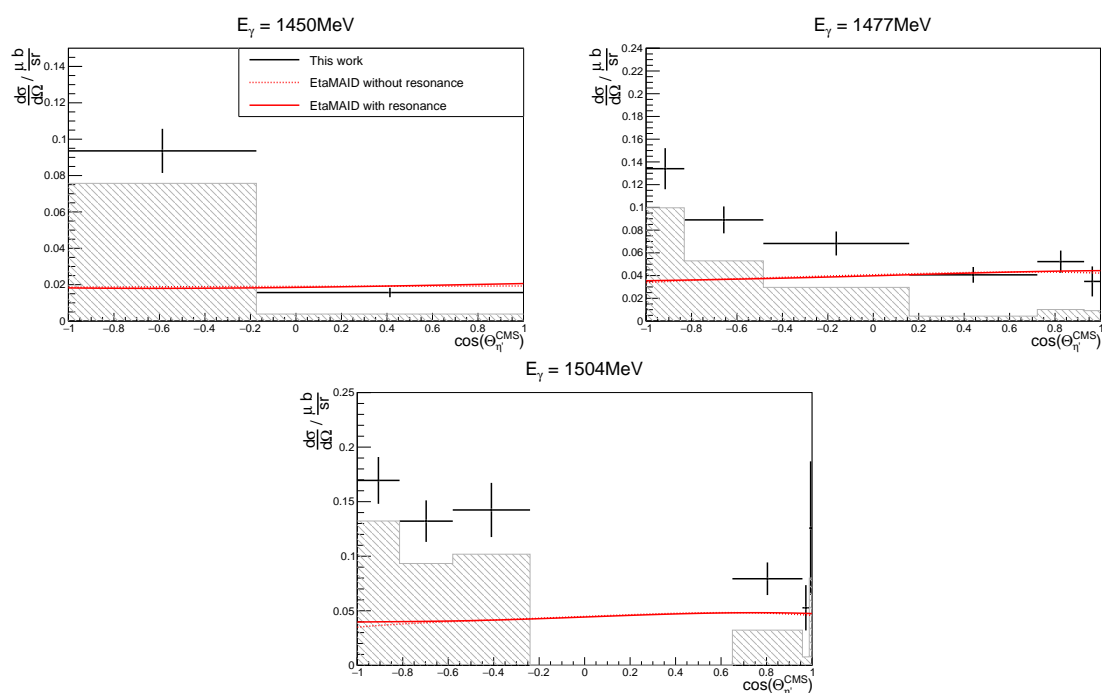
Figure 4.29: Resulting differential cross sections for $\eta' \to \pi^0\pi^0(\eta)$ (black data points) for the chosen energy bins as well as the corresponding EtaMAID parametrizations [34, 54] with and without the S_{11} (1900) included (solid and dashed red line, respectively). The error bars indicate the statistical errors, while the shaded areas show the systematic uncertainties. The legend for all plots is shown in the left plot.

4.2.3 $\eta' \to \gamma\gamma$

In addition to the proton in the forward spectrometer two photons in the rugby ball are required. If there are any further particles, the event is discarded.

The four-momenta of the two photons are combined and if their invariant mass is within 1σ of the η' mass peak, the resulting four-vector is considered to be an η'. The invariant mass distribution is shown in figure 4.30.
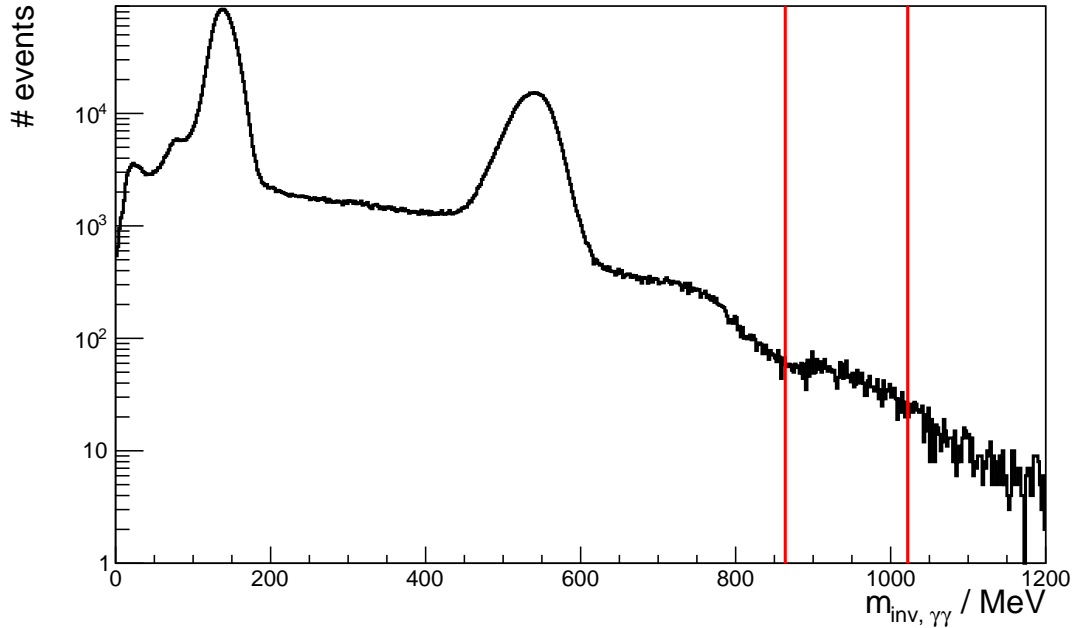
Figure 4.30: Invariant mass $m_{\text{inv, }\gamma\gamma}$ of the two photons for $\eta' \to \gamma\gamma$. For better visibility the plot is shown logarithmicly. The red lines indicate the short target cuts.

The π^0 and η peak are clearly visible on top of the background. Due to its small branching ratio into two photons and small cross section, the η' peak is small. Thus only a 1σ cut was used, since a 2σ cut picks up a significant amount of the rising background under the signal peak and the goal of this reconstruction method is to remove as much background as possible. If better statistics are desired in a future analysis, this cut can be loosened. If no η' is reconstructed, the event is discarded.

With the η' identified the missing mass to the η' is determined using

$$m_{\text{miss, }\eta'} = \sqrt{\left(p_\gamma + p_{\text{target}} - p_{\eta'}\right)^2}, \tag{4.9}$$

where $m_{\text{miss, }\eta'}$ is the missing mass to the η', p_γ is the four-momentum of the initial photon, p_{target} is the four-momentum of the target (i.e. a proton at rest) and $p_{\eta'}$ the four-momentum of the reconstructed η'.

To remove background a cut is placed on the difference Δp between the missing momentum and the momentum of the reconstructed proton, as well as the angle Ω between them. The respective

distributions for real data, simulated $\eta' p$ and simulations of the relevant backgrounds (see table 4.3) are shown in figure 4.31.
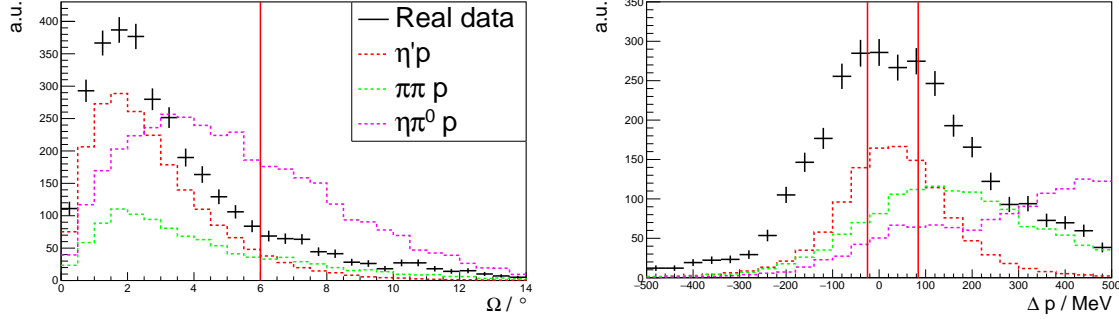
Figure 4.31: Angle Ω between the reconstructed proton and $m_{\mathrm{miss},\,\eta'}$ for real data and simulation (left) and difference between the missing momentum and the reconstructed proton momentum Δp for real data and simulation (right). The solid red lines indicate the performed cuts for the short target beam times. In the left plot all events with an angle bigger than the red line are removed. Distributions are scaled for better visibility, their relative heights do not represent their relative strength. The legend is shown in the left plot.

Only for $\eta' p$ does $m_{\mathrm{miss},\,\eta'}$ actually correspond to the measured proton. As a result Ω and Δp peak closer to zero compared to the background channels. Furthermore those backgrounds are not two-body reactions, resulting in more smeared out distributions. Thus a cut can be placed on each parameter to further reduce background. For Ω there is only one cut value, that excludes all higher angles. The cut on Δp is applied after the Ω cut.

To determine the best values, the S/N is calculated by extrapolating the background under the signal peak in the spectrum shown in figure 4.8, using a polynomial of third order and comparing its integral of the peak above that background. This is done over the whole angular range. In contrast to the previous determinations of best cut values a polynomial was chosen instead of a linear extrapolation, since it is more reliable with the limited statistics present.

The best S/N is achieved for a $\Omega < 6\,^\circ$ cut and a $\frac{1}{2}\sigma$ cut on Δ. The different cut values and their respective S/N are shown in table 4.10.

Cut in $^\circ$	4	6	8	10	12	14	16
S/N	2.42	2.57	2.34	2.40	2.42	2.44	2.40
Cut in σ	$\frac{1}{2}$	$\frac{1}{2}$	1				
S/N	3.65	5.34	2.30				

Table 4.10: Different cut values for Ω (top) and Δp (bottom). Cuts shown in bold are asymmetric. The cuts on Δp were performed with the chosen Ω cut already applied.

As done previously these cuts are chosen for their highest S/N, to reduce as much background as possible. In a future analysis the cuts can be loosened to acquire more statistics.

The resolution and binning are determined analogous to previous sections. Figure 4.32 shows the resolution as well as the number of events as a function of $\cos(\Theta_{\eta'}^{\mathrm{CMS}})$, while table 4.11 shows the resulting binning.
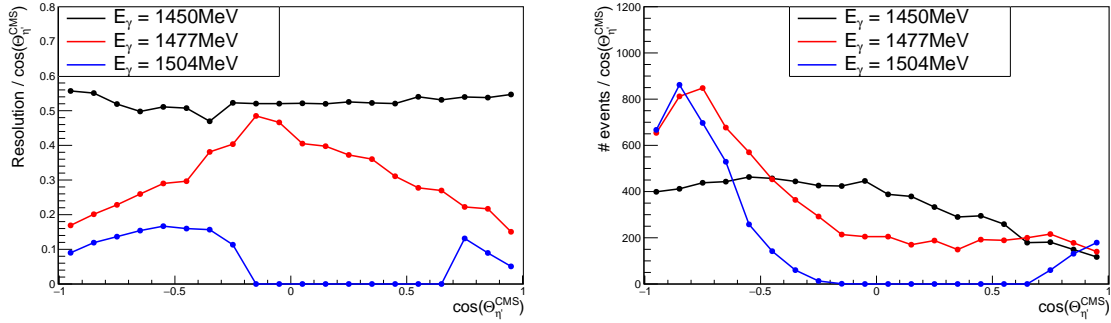
Figure 4.32: Resolution (left) and number of events (right) as a function of $\cos(\Theta_{\eta'}^{CMS})$ for $\eta' \to \gamma\gamma$. Entries at zero for the 1504 bin are a result of the momentum correction.

The distributions of the different resolutions are similar to before, with the 1450 distribution being more flat and the 1477 distribution having a more pronounced peak, compared to previous reconstruction methods. Generally, the resolution is worse for this reconstruction method in the first two energy bins. This is because the $\cos(\Theta_{\eta'}^{CMS})$ is now determined through the lab angles of its two decay photons in the rugby ball, while it was previously determined through the lab angle of the proton in the forward spectrometer. As shown in section 3.2, the angular resolution of the forward spectrometer is much higher than that of the rugby ball. This only changes for higher energy photons, where the clusters in the rugby ball get larger due to the increase in energy deposit and thus the angular resolution improves. A resolution similar to the other reconstruction methods can be achieved by using the missing mass to the forward proton as the η', as it was done previously. The η' reconstructed from the two photons is than only used for background suppression, as shown in figure 4.31. This can be done in a future analysis.

Overall this discrepancy in binning is not a huge concern, since the number of $\cos(\Theta_{\eta'}^{CMS})$ bins in the threshold energy bin, where the highest difference between the EtaMAID parametrizations is observed, does not change. Furthermore, as mentioned before, a real improvement of the resolution can only be made by using the ARGUS detector, since the $\cos(\Theta_{\eta'}^{CMS})$ resolution heavily depends on the resolution of the initial photon energy.

The drop-of in the number of entries seen towards more forward $\cos(\Theta_{\eta'}^{CMS})$ is more pronounced than the one seen in figures 4.20 and 4.26. This is because previously only some of the η' decay products were required, while now both have to be detected in the rugby ball. With the decay products from forward going η' having on average small lab angles, there is a high probability of at least one photon not hitting the rugby ball and thus the event being discarded.

Due to the worse resolution the number of angular bins for the 1477 energy bin heavily decreases, while there is one less angular bin in the 1504 energy bin.

Energy bin							
1450	-1.0	-0.010	1.0				
1477	-1.0	-0.558	0.546	1.0			
1504	-1.0	-0.784	-0.484	-0.176	-0.144	0.650	0.898	1.0

Table 4.11: $\cos(\Theta_{\eta'}^{CMS})$ bin borders for the different energy bins for $\eta' \to \gamma\gamma$.

Using the binning shown in table 4.11 the reconstruction efficiency is determined. Figure 4.33 shows the reconstruction efficiencies for the different energy bins. As before, they follow the patterns seen in figure 4.32 on the right, including the stronger dip towards forward $\cos(\Theta_{\eta'}^{CMS})$. Due to the small branching ratio of $\eta' \to \gamma\gamma$ and the strict cuts applied, the reconstruction efficiency is well below 1 %.
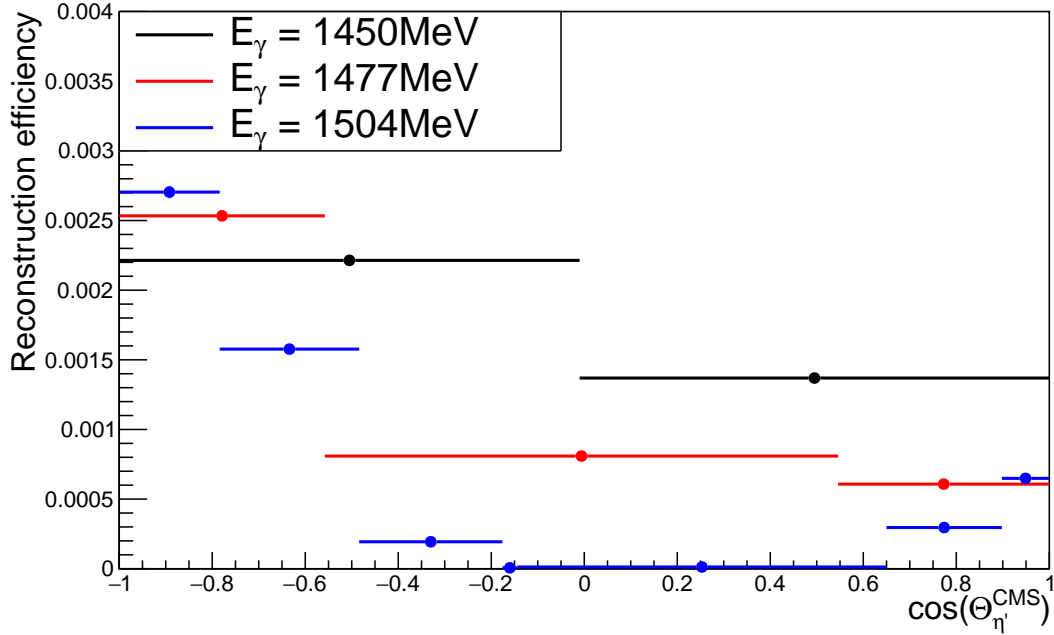
Figure 4.33: Reconstruction efficiencies for the different energy bins for $\eta' \to \gamma\gamma$.

The simulated spectra are subsequently fitted to the real data from 1 304 MeV to 1 797 MeV, while excluding the region from 1 437 MeV to 1 597 MeV. Some exemplary fits are shown in figure 4.34. All fits are found in appendix A.4.

The background is highly reduced, to the extend that some sideband bins show no entries at all. Within the statistical errors there is a good agreement between the fit and the real data in the left sideband. In the right sideband the fit overestimates the real data, but given the statistical errors, there is still a decent agreement, especially for the more backward bins.

The top left bin in figure 4.34 has significantly better statistics than the rest of the bins. This is due to the same reason already mentioned when discussing figure 4.32. The comparably big size of this bin, enhances this effect further.

Due to the overall limited statistics not many data points are available in the sidebands in the more forward bins, see figure 4.34 on the bottom right as an example. This could indicate, that there is actually no background left in those bins and all events at higher beam energies are actually $\eta'p$ events. This is supported by the fact, that the left sideband, which can not contain any $\eta'p$ events, is basically zero for all angular bins. The simulated background distributions show strong statistical fluctuations in those angular bins, which further underlines the strong background reduction.

This idea has to be carefully checked in the future, since there can still be background left under the peak, even with a strong suppression in the sidebands. Furthermore the absence of events in the left
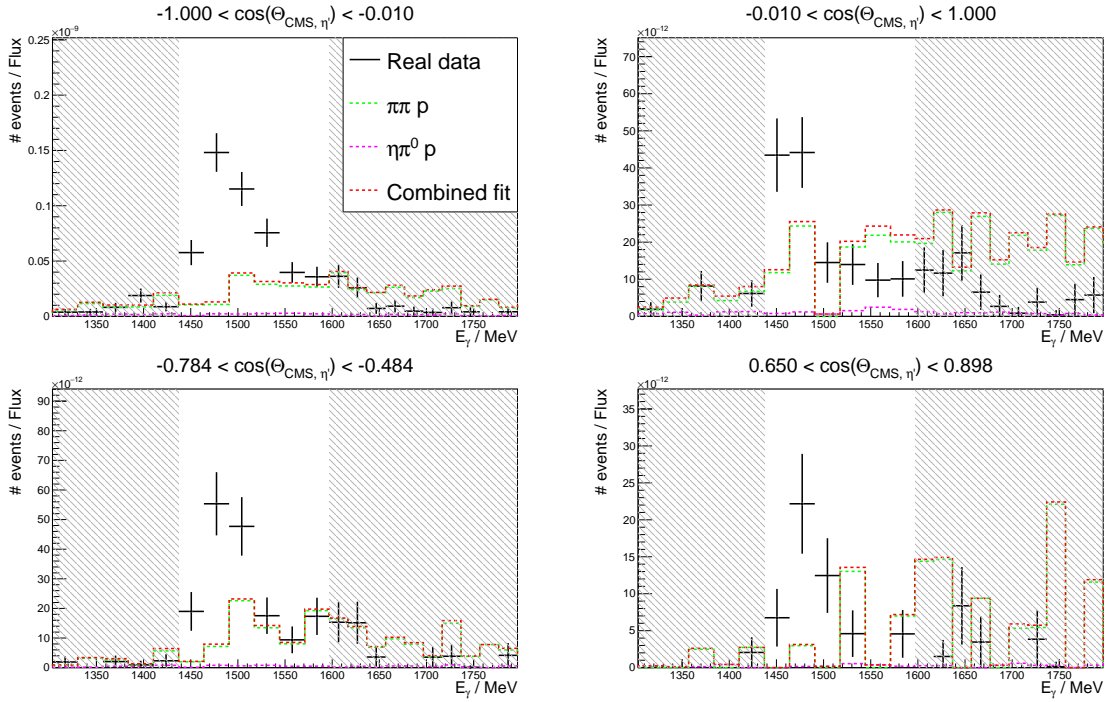
Figure 4.34: Exemplary fits for $\eta' \to \gamma\gamma$: the shaded areas indicate the two sidebands. The respective $\cos(\Theta_{\eta'}^{\text{CMS}})$ bin is given in the title of each plot, while the legend is shown in the top left plot.

sideband could be a purely statistical effect, that vanishes with higher statistics.

The effects of the proton momentum correction in the three corrected energy bins are barely visible anymore. This is because the strong statistical fluctuations mask those effects.

After the subtraction of the background from real data the differential cross sections are determined using formula 4.3, they are shown in figure 4.35. The statistical errors are calculated as mentioned in equation 4.4. The systematic errors can be found in subsection 4.3.3. Due to the good agreement of the results from this work to EtaMAID, the component concerning the background modeling is taken out of the systematic error calculation. Hence these error consist of the systematic errors from the experiment and the systematic error stemming from the reconstruction.

It can be seen, that, within their statistical errors, most datapoints agree to the two EtaMAID parametrizations. The fact, that most results lie below EtaMAID, indicates, that the background was significantly overestimated in the fit. Given how little simulated background is left under the signal peak in some more forward angular bins in figure 4.34, this further supports that there might be no background at all in those angular bins.

Nonetheless the results from this work still increase for more backward $\cos(\Theta_{\eta'}^{\text{CMS}})$ for the 1477 and 1504 bin, which is the same effect seen previously in figures 4.16, 4.23 and 4.29. This indicates that some background must be present in these bins.

Since any possible background is so heavily reduced, a problem with its description under the signal peak does not have such a strong effect on the resulting cross sections any more. This leads to the good agreement of the results from this work to EtaMAID.
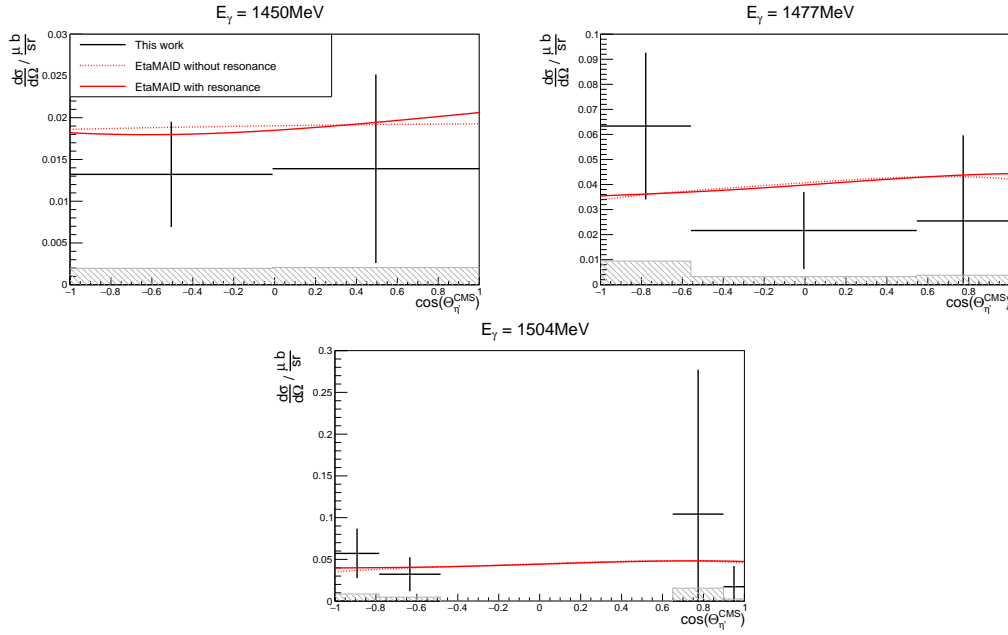
Figure 4.35: Resulting differential cross sections for $\eta' \to \gamma\gamma$ (black data points) for the chosen energy bins as well as the corresponding EtaMAID parametrizations [34, 54] with and without the S_{11} (1900) included (solid and dashed red line, respectively). The error bars indicate the statistical errors while the shaded areas show the systematic uncertainties. The legend for all plots is shown in the top left plot.

Overall the statistical errors are significantly larger than the difference between the two EtaMAID parametrizations, making it impossible to distinguish the two. To reduce these errors more data can be taken and the cuts on Ω and Δp can be loosened, see subsection 4.3.4 for more details.

The systematic errors are also larger than the difference between the two EtaMAID parametrizations, even though they do not include the component concerning the background modeling. They are now dominated by the systematic uncertainty stemming from the reconstruction, which will change with improved statistics. This is explained in more detail in subsection 4.3.3.

Reconstructing the η' fully exclusive through $\eta' \to \gamma\gamma$ thus allows for a nearly complete reduction of the background. With very little background left the EtaMAID results can be reproduced, showing that the differences between those results and results from this work observed in figures 4.16, 4.23 and 4.29 are due to the description of the background in the signal region.

At threshold the background is of the order of $10\,\%$. Assuming the beam asymmetry of $\eta' p$ is zero and the results from GRAAL [26] are purely a consequence of asymmetry in the background, this background would need an asymmetry ten times as large, as the one measured. Looking at figure 2.4, the highest measured asymmetry in the lower energy bin is about 0.12. Thus, given a background contribution of $10\,\%$, the background beam asymmetry must be approximately 1.2. This is not a physical result, as the beam asymmetry can only have values between one and minus one.

Thus the results from this reconstruction method support the results reported by the GRAAL collaboration, as a beam asymmetry of that size can not be produced with the limited background left.

4.3 Comparison

In this section the results of the different analysis methods are compared. In the end a projection is made on how much more data is still needed for each method for a successful analysis.

4.3.1 Resolution

Figure 4.36 shows a comparison of the $\cos(\Theta_{\eta'}^{CMS})$ resolution for the different reconstruction methods for the different energy bins.
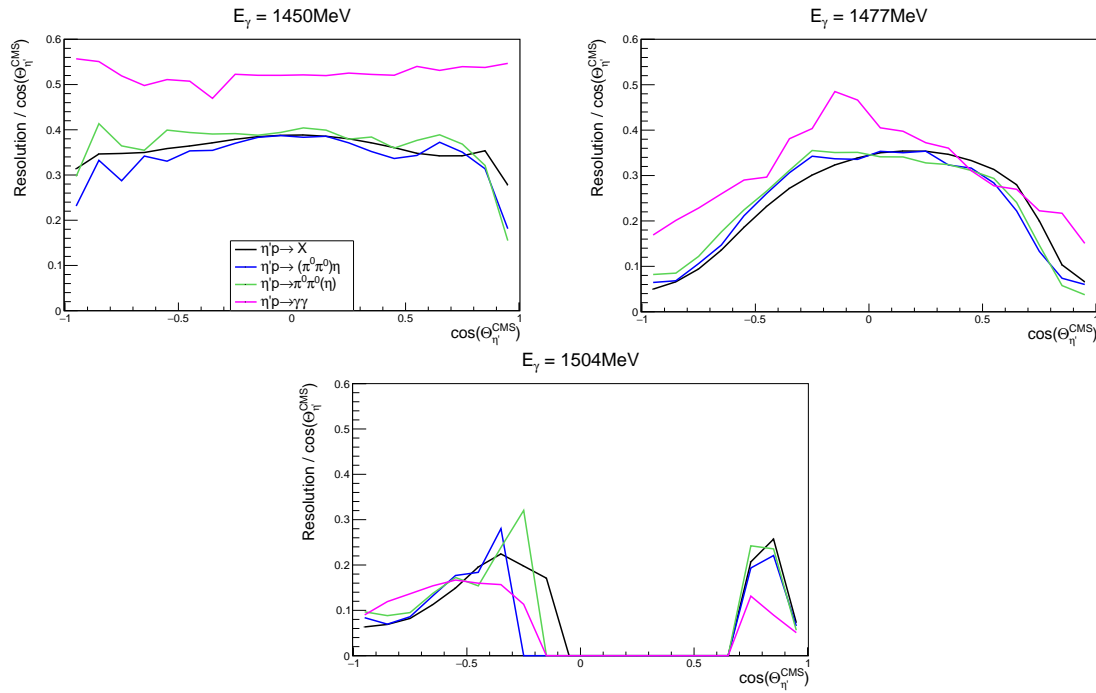
Figure 4.36: Resolutions for the different analysis methods in the three energy bins. The legend is shown in the top left plot.

As can be seen the resolutions for $\eta' \to X$, $\eta' \to (\pi^0\pi^0)\eta$ and $\eta' \to \pi^0\pi^0(\eta)$ are similar for all energies and angles. This is because the $\cos(\Theta_{\eta'}^{CMS})$ is mainly determined by the lab angle of the proton, which has the same resolution for all methods. In contrast $\eta' \to \gamma\gamma$ has a slightly worse resolution in the 1450 and 1477 energy bin. As mentioned before, for this method the η' is reconstructed through its two decay photons in the rugby ball, which then determine the η' lab angle. Since the angular resolution of the rugby ball is worse than that of the forward spectrometer for lower energy photons, this leads to a worse $\cos(\Theta_{\eta'}^{CMS})$ resolution. For higher photon energies the clusters produced by the photons in the rugby ball get larger, since more energy is deposited in the crystals. This improves the angular resolution such, that it is comparable to those of the other reconstruction methods.
The resulting binnings are similar in the 1450 Tagger energy bin as there are only two $\cos(\Theta_{\eta'}^{CMS})$ bins available, see tables 4.5, 4.7, 4.9 and 4.11. In the 1477 bin $\eta' \to \gamma\gamma$ has significantly less angular bins, due to the reason mentioned above, while the other reconstruction methods have a similar amount of bins. The amount of $\cos(\Theta_{\eta'}^{CMS})$ bins in the 1504 energy bin is similar for all reconstruction methods.

Since the strongest difference between the two EtaMAID parametrizations is observed in the 1450 bin, where the binnings are similar for all methods, none can be really favored due to its resolution. Looking at higher beam energies, $\eta' \to \gamma\gamma$ is less favorable if a finer binning is desired, especially for the 1477 bin. This can be resolved if, as mentioned in subsection 4.2.3, the η' angle is derived from the proton angle for $\eta' \to \gamma\gamma$.

4.3.2 Cross sections

Figure 4.37 shows a comparison of the cross section results from the different analysis. Except for $\eta' \to \gamma\gamma$ the results from this thesis are within their statistical errors too high compared to the two EtaMAID parametrizations. This shows, that the background in the signal region is not well described. As mentioned before this disagreement increases for more backward η', i.e. more forward going protons. This hints at a systematic issue with the determination of the proton momentum for the backgrounds.

The agreement between results from this work and EtaMAID increases with higher exclusiveness, as the problematic background gets removed. This culminates in the results from the totally exclusive reconstruction $\eta' \to \gamma\gamma$, where the results are compatible to EtaMAID within the statistical errors.

It can further be seen, that the increase in exclusiveness limits the available statistics. As a result the statistical errors for $\eta' \to \gamma\gamma$, $\eta' \to (\pi^0\pi^0)\eta$ and $\eta' \to \pi^0\pi^0(\eta)$ are far larger than those for $\eta' \to X$. Thus they are not sufficiently small enough to distinguish between the two EtaMAID parametrizations. For $\eta' \to X$ this is the case.

4.3.3 Systematic uncertainties

The systematic uncertainties stemming from the experimental side are already listed in table 4.4. They are constant and the same for each reconstruction method.

The errors related to the different reconstruction methods are shown in table 4.12. They are determined by changing all cuts made in the reconstruction and looking at the differences in yield this causes. A more detailed explanation on the determination of those errors is found in subsection 4.1.6.

Reconstruction method	% error
$\eta' \to X$	0.03
$\eta' \to (\pi^0\pi^0)\eta$	3.2
$\eta' \to \pi^0\pi^0(\eta)$	5.7
$\eta' \to \gamma\gamma$	12.8

Table 4.12: Systematic uncertainties specific to the different reconstructions.

The systematic uncertainty rises with increasing exclusiveness, since this leads to a decrease in statistics. Thus there are higher fluctuations in the values, that are cut on, leading to bigger differences in the ratio between simulation and real data for the different cut values.

$\eta' \to X$, which has great statistics, demonstrates how with sufficient data, this systematic error tends towards zero and can safely be neglected in comparison to the systematic error stemming from the experiment, shown in table 4.4.

The systematic errors concerning the background modeling are shown in table 4.13. They are estimated
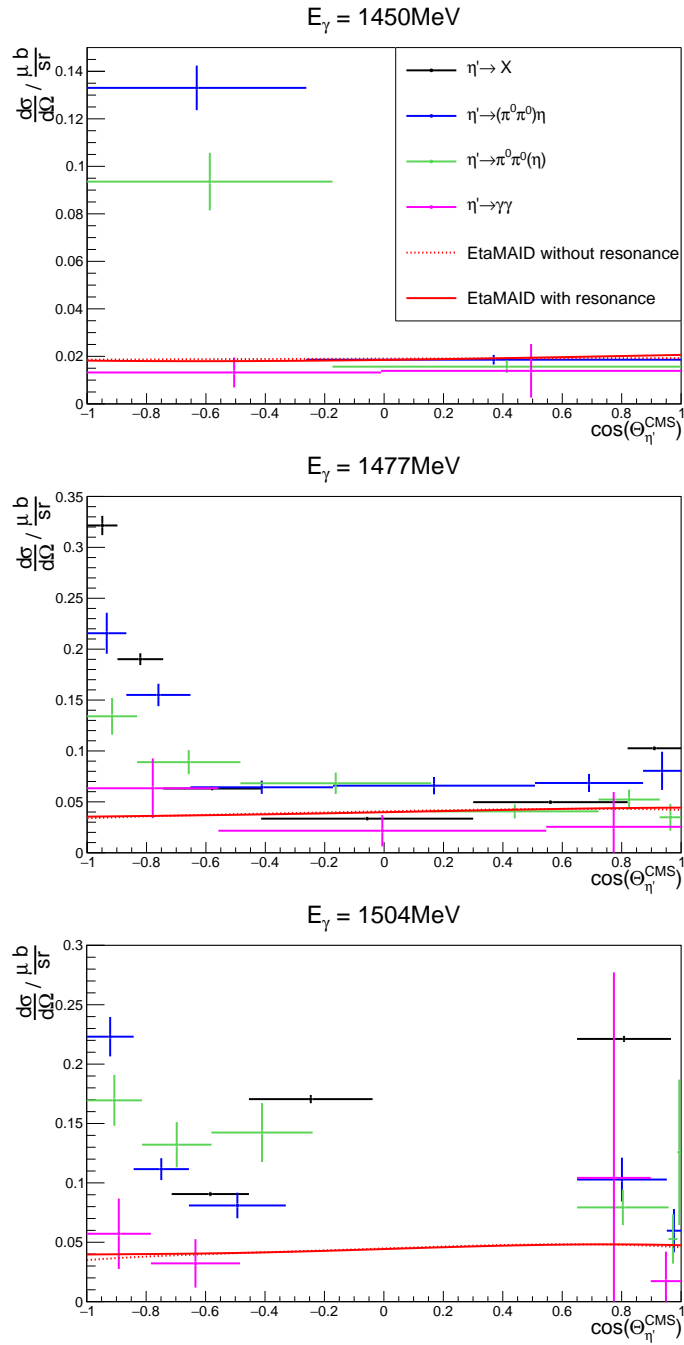
Figure 4.37: Differential cross section results obtained from the different analysis methods for the chosen energy bins, as well as the corresponding EtaMAID parametrizations [34, 54] with and without the S_{11} (1900) included (solid and dashed red line, respectively). The error bars indicate the statistical errors. The systematic uncertainties are not shown for better visibility. They can be seen in figures 4.16, 4.23, 4.29 and 4.35. Note that there are no results for $\eta' \to X$ for some bins, as mentioned in subsection 4.2.1 The legend for all plots is found in the top plot.

by determining the difference between results from this work and the EtaMAID results [34, 54]. They are explained in more detail in subsection 4.1.6.

Reconstruction method	% error
$\eta' \to X$	94.4
$\eta' \to (\pi^0\pi^0)\eta$	53.7
$\eta' \to \pi^0\pi^0(\eta)$	46.9

Table 4.13: Average systematic uncertainties related to the modeling of the background. $\eta' \to \gamma\gamma$ is not shown, due to the good agreement between the results from this reconstruction method and EtaMAID.

These uncertainties have a different value for each cross section data point, since the difference between the results from this work and EtaMAID changes. While the individual values are plotted in the respective figures, table 4.13 only shows the average of all errors for the respective reconstruction methods. This is done to give an indication of the size of these errors and how they change with increasing exclusiveness.

As can be seen, the systematic errors concerning the background modeling are large and decrease with increasing exclusiveness. This is to be expected, as figures 4.16, 4.23 and 4.29 already demonstrated, that the results from this work do not agree well to the EtaMAID parametrizations, but show a better agreement to those, with increasing exclusiveness. Due to the limited accuracy of the background description shown in these figures, the total systematic error is by far dominated by the errors concerning the background modeling.

Since the results from $\eta' \to \gamma\gamma$ show an agreement to the EtaMAID parametrizations within the statistical errors, this component of the systematic uncertainty is omitted for $\eta' \to \gamma\gamma$.

4.3.4 Future data taking

Except for $\eta' \to X$, more data is needed to get statistical errors comparable to the difference between the two EtaMAID parametrizations. To get an estimate of how much more data is needed to get reasonable statistical errors, the highest available difference between the two EtaMAID parametrizations $\Delta_{\text{MAID}} = 0.00085\mu b$, which is in the first angular bin of the 1450 bin, is determined.

Since the number of reconstructed events N in this bin, as well as the corresponding EtaMAID cross section σ_{MAID} are known, the number of reconstructed events can be calculated, under the assumption, that the EtaMAID parametrizations are successfully reproduced. For this estimation the two parametrizations are averaged and the resulting statistical error is calculated using

$$\Delta\sigma = \frac{\sqrt{\frac{\sigma_{\text{MAID}}}{\sigma_{\text{this work}}} \cdot N}}{\Delta\Omega \cdot \rho_{\text{target}} \cdot \epsilon \cdot F_\gamma}, \tag{4.10}$$

where $\sigma_{\text{this work}}$ is the cross section result from this work and the parameters in the denominator correspond to those shown in equation 4.3.

Previously the error of the fit was also considered in the statistical error, see formula 4.4. Under the assumption that the EtaMAID parametrizations are successfully reproduced, this error can be neglected, since this assumption requires a good fit. This leads to a small fit error.

By dividing $\Delta\sigma$ by Δ_{MAID}, the factor by which the statistical error must decrease, is determined.

Squaring this factor gives the total amount of data needed for an error of this size. The number of beam hours, that still need to be taken, $N_{\text{already taken}}$ is calculated using

$$N_{\text{hours}} = N_{\text{already taken}} \cdot \left(\frac{\Delta\sigma}{\Delta_{\text{MAID}}}\right)^2 - N_{\text{already taken}}, \tag{4.11}$$

where $N_{\text{already taken}}$ is the number of beam hours already taken.

Due to changes in the experimental conditions, not all beamtimes produce a similar rate of $\eta' p$ events per hour. The best conditions were reached in the 2018-12 beamtime. Thus all estimates presented from here on, were made under the assumption of 2018-12 conditions for any future data taking. While 2018-12 provides the highest rate, it is only about 6 % higher than that for 2017-04, since the beam current had to be tuned down, when using the longer target in 2018-12.

The results are shown in table 4.14. The amount of $\eta' p$ events reconstructed in the three analyzed energy bins is also given as well the corresponding rate. Note that the rate is an average over all beam times, to give an indication of the relative rates of the different reconstruction methods.

Decay channel	$N_{\eta' p}$	$\eta' p / h$	N_{hours}
$\eta' \to X$	34470	25.42	0
$\eta' \to (\pi^0\pi^0)\eta$	789	0.58	8100
$\eta' \to \pi^0\pi^0(\eta)$	1024	0.76	6600
$\eta' \to \gamma\gamma$	155	0.11	12700

Table 4.14: Beam hours still needed for each analysis method to get statistical errors comparable to the difference in the EtaMAID parametrizations. The previous beam times combine for a total of 1 356 h of beam time, see table 4.1.

As mentioned before, no additional data is needed for $\eta' \to X$. For the other reconstruction methods, the amount of additional beam hours significantly exceeds the amount of hours already taken.

These numbers can be improved, by loosening some of the very tight cuts used in the analyses of $\eta' \to (\pi^0\pi^0)\eta$, $\eta' \to \pi^0\pi^0(\eta)$ and $\eta' \to \gamma\gamma$. For this work those narrow cuts were chosen, to remove the problematic background. Assuming a better proton momentum correction and a better background description, these cuts can be made more wide, without compromising the analyses. This will result in more $\eta' p$ events passing the cuts and thus smaller statistical errors for the cross sections.

Looking at the distributions on which the cuts were performed (figures 4.18, 4.25 and 4.31), it can be estimated by how much the number of $\eta' p$ events increases for a more loose cut. The statistical error including these more loose cuts is calculated using

$$\Delta\sigma' = \Delta\sigma\sqrt{\frac{1}{x}}, \tag{4.12}$$

where $\Delta\sigma'$ is the new statistical error after the loosened cuts and x is the factor by which the number of $\eta' p$ events has improved. The additional beam hours are again calculated according to equation 4.11. Table 4.15 shows how the number of additional beam hours changes with different cut values. Releasing the cuts greatly decreases the amount of additional beam hours still needed. For $\eta' \to (\pi^0\pi^0)\eta$ and $\eta' \to \pi^0\pi^0(\eta)$ this additional time is ideally less than the combined sum of all previous beam times. For $\eta' \to \gamma\gamma$ it is of the order of three times more.

Thus a better background description under the signal peak will not only lead to a better agreement

$$\eta' \rightarrow (\pi^0\pi^0)\eta:$$

Cut on $m_{\text{miss, }\eta p}$	$\mathbf{1\sigma}$	$\frac{3}{2}\sigma$	2σ	$\frac{1}{2}\sigma$	$\frac{2}{3}\sigma$	1σ	2σ
N_{hours}	4200	3200	2800	4200	2900	1900	1100

$$\eta' \rightarrow \pi^0\pi^0(\eta):$$

Cut on $m_{\text{miss, }\pi^0\pi^0 p}$	$\mathbf{1\sigma}$	$\frac{3}{2}\sigma$	2σ	$\frac{1}{2}\sigma$	$\frac{2}{3}\sigma$	1σ	2σ
N_{hours}	3800	2800	2600	3500	2600	1700	900

$$\eta' \rightarrow \gamma\gamma:$$

Cut on Ω	$< 8°$	$< 10°$	Cut on Δp	1σ	2σ	2σ on $m_{\text{inv, }\gamma\gamma}$	all comb.
N_{hours}	12400	12100			6600	4600	9100	3300

Table 4.15: Additionally needed beam hours for each analysis method to get statistical errors comparable to the difference between the two EtaMAID parametrizations, depending on different cut values. Cut values in bold indicate asymmetric cuts. $\eta' \rightarrow X$ is not shown as it does not need more data and there are no cuts to relax. The previous beam times combine for a total of $1\,356\,\text{h}$ of beam time, see table 4.1.

with EtaMAID parametrizations. It also makes releasing some very tight cuts possible, which improves the overall statistics of all reconstruction methods. As a result significantly less additional beam time is needed to get the necessary statistical errors for $\eta' \rightarrow (\pi^0\pi^0)\eta$, $\eta' \rightarrow \pi^0\pi^0(\eta)$ and $\eta' \rightarrow \gamma\gamma$.

Given the small difference between the two EtaMAID parametrizations and the difficulty of acquiring the necessary statistics, determining the beam asymmetry might proof to be easier. The beam asymmetry is determined using

$$A = \frac{1}{P_\gamma(E_\gamma)} \frac{N^+ - N^-}{N^+ + N^-} = \Sigma(E_\gamma, \Theta_{\eta'}^{\text{CMS}})\cos(2\phi_{\eta'}), \tag{4.13}$$

where + and - refer to two perpendicular polarization planes, $N^\pm$ is the number of events in the respective polarization planes, $P_\gamma(E_\gamma)$ is the degree of polarization, $\Sigma(E_\gamma, \Theta_{\eta'}^{\text{CMS}})$ is the beam asymmetry and $\phi_{\eta'}$ is the azimuthal angle of the η'. The degree of polarization varies between the two polarization planes and the different beam times, but for this estimation, the average of the two is taken, which is $\approx 24\,\%$. Normally the event numbers must be normalized by the integrated flux for the respective planes, to account for differences in the amount of data taken. Given that this difference is small for the data used for this work, the flux is assumed to be similar for both planes, meaning it cancels out in the above equation.

A $\cos(2\phi_{\eta'})$ fit is applied to the $\phi_{\eta'}$ distribution of A in the different $\cos(\Theta_{\eta'}^{\text{CMS}})$ bins of each energy bin and the amplitude of said fit yields the beam asymmetry as a function of $\cos(\Theta_{\eta'}^{\text{CMS}})$ and energy. Assuming that the number of events from both polarization planes are roughly the same ($N^+ \approx N^- = N$) and given that the statistical error on this is $\Delta N = \sqrt{N}$, the error on A is determined using

$$\Delta A = \frac{1}{P_\gamma(E_\gamma)} \sqrt{\frac{1}{2N}}, \tag{4.14}$$

which is derived using gaussian error propagation. Solving this equation for N, yields the number of events necessary to achieve a specific ΔA using a given degree of polarisation.

The average beam asymmetry in each $\cos(\Theta_{\eta'}^{CMS})$ bin is calculated using the $f = a \cdot \sin^2(\Theta)\cos(\Theta)$ fit shown in figure 2.4. Assuming the first energy bin can be divided into two equally sized $\cos(\Theta_{\eta'}^{CMS})$ bins, those averages are -0.06 and 0.06, respectively. As a result A can have a maximum absolute value of 0.06.

Of the 34470 events reconstructed using $\eta' \rightarrow X$, about 10 700 are reconstructed in the first energy bin. Splitting this up into two equally sized $\cos(\Theta_{\eta'}^{CMS})$ bins, with seven $\phi_{\eta'}$ bins each, the amount of events per $\phi_{\eta'}$ bin per polarization plane is ≈ 380. The resulting statistical error of A is $\Delta A = 0.15$. This is significantly larger than the maximum possible value of A, meaning that more data needs to be taken for a proper fit.

Even though the results reported by the GRAAL collaboration are achieved with 12121 events [26], which is comparable to the statistics available for this work, the resulting statistical errors at GRAAL are much smaller. This is due to the fact, that GRAAL operates with a degree of polarization of 96 % [26], which is far higher than the ≈ 24 %, which were achieved at BGOOD.

Assuming a 33 % statistical error on A ($\Delta A = 0.02$), the necessary amount of events is $N = 21\,700$. Under the assumption, that there are seven $\phi_{\eta'}$ bins per $\cos(\Theta_{\eta'}^{CMS})$ bin, a total of 608 000 events is necessary in the first energy bin, to achieve a 33 % statistical error on A in every $\phi_{\eta'}$ bin. This number of events is significantly larger than the 10 700 events reconstructed in the first energy bin, using $\eta' \rightarrow X$. Assuming $\Delta A = 0.06$, the number of events needed to achieve this statistical error is 67 500 for the first energy bin.

Thus the beam asymmetry can not be determined with good statistical accuracy, given the available data. Furthermore it will be challenging to achieve the necessary statistics even with future data taking, as about six times the current data is needed for $\eta' \rightarrow X$, to achieve statistical errors of the size of the asymmetry.

Consequences for future analyses/data taking

It was shown, that fitting the real data using a simulation of all relevant background reactions does not work sufficiently well for every reconstruction method but $\eta' \to \gamma\gamma$. This is evident in the fits shown in figures 4.15, 4.22 and 4.28, where both the left and right sideband can not be consistently well described. Additionally the resulting cross sections shown in figure 4.37 indicate, that even in those bins with well-working fits, the extrapolation from sidebands to the signal region underestimates the amount of background. Consequentially all results from this work, except those for $\eta' \to \gamma\gamma$, are generally too high within their statistical errors.

There are a few key points, that can be analyzed in a future analysis, to improve the background description. For $\eta' \to \gamma\gamma$ very little background (on the order of at most 10 %) is left in the signal region. Due to the fact, that some of the cross section results from this work lie below EtaMAID, it should be investigated if, at least for some bins, no background is left after all cuts. This would make this a very clean channel, with no need for fitting.

This is consistent with what was reported by the GRAAL collaboration, which estimated their background contribution to be approximately 4 % [26]. This supports, that the beam asymmetry must stem from $\eta' p$ as an asymmetry of that size can not be a result of the small background left, see subsection 4.2.3.

Furthermore the $\eta' \to \gamma\gamma$ decay mode should be analyzed, using the polar angle of the missing mass to the proton, instead of the polar angle of the reconstructed η'. This will make this reconstruction methods consistent with the other ones and the resolution comparable to that of the other reconstruction methods.

Proper differential cross sections can be implemented for the multi-meson backgrounds, instead of the currently used phase-space distributions. This will not have a huge effect, as the CMS angle $\cos(\Theta_{\eta'}^{\mathrm{CMS}})$ is calculated under the assumption of a two-body reaction and thus smears out the cross section of a multi-body reaction.

Additionally a more detailed investigation into the normalization of the simulation should be undertaken, since it plays an important role for the simulated spectra being used in the fit.

Currently the proton momentum correction corrects the proton momentum solely based on the absolute value of the momentum and not its direction. As shown in figure 4.37 this leads to a systematic shift between the results from this work and the EtaMAID parametrizations. This shift worsens with increasing proton lab momentum, which corresponds to increasingly backward η' in the CMS. There are on-going efforts to make such a correction and implement it into the general analysis-framework.

Once this is completed, a rerun of this analysis should provide improved results.

Thus from the current analysis and fitting standpoint, only $\eta' \to \gamma\gamma$ is a viable method to get a clean $\eta'p$ signal. With the above mentioned improvements the other reconstruction methods will become viable as well.

With the strict cuts currently employed for this analysis, only $\eta' \to X$ has sufficiently high statistics, such that the statistical error is smaller than the largest difference between the two EtaMAID parametrizations and the presence of a narrow resonance close to the $\eta'p$ threshold can be verified/falsified. Additional data is needed for the other reconstruction methods.

As demonstrated in subsection 4.3.4 and shown in table 4.15, relaxing the cuts greatly reduces the amount of additional data needed. The amount of additionally needed beam hours is below that already taken in the cases of $\eta' \to (\pi^0\pi^0)\eta$ and $\eta' \to \pi^0\pi^0(\eta)$ and about three times as high for $\eta' \to \gamma\gamma$. Since more relaxed cuts decrease the amount of background being cut away, the analytical improvements mentioned above are crucial to make these statistical improvements work.

Furthermore the correct beam time conditions need to be chosen, as the rate of $\eta'p$ events is about three times as high for 2018-12 and 2017-04 than it is for 2015-11 and 2015-06. 2018-12 has a 6 % higher rate than 2017-04, but the overall resolution is slightly better for 2017-04, due to the shorter target. Due to the importance of a good angular resolution in the lab frame, the benefit of having the shorter target, likely outweighs the improved rate 2018-12 offers.

Concerning a possible determination of the beam asymmetry itself, it was shown in subsection 4.3.4, that at least six times the current amount of data is needed for $\eta' \to X$, to get statistical errors of the size of the asymmetry, assuming seven $\phi_{\eta'}$ and two $\cos(\Theta_{\eta'}^{\mathrm{CMS}})$ bin for each Tagger energy bin. For the other reconstruction methods, this number greatly increases.

Due to the significant amount of additionally needed data, it is not advised to pursue a direct beam asymmetry measurement, for any reconstruction method other than $\eta' \to X$.

As shown in subsection 4.3.1 the $\cos(\Theta_{\eta'}^{\mathrm{CMS}})$ resolution, regardless of analysis method, is only good enough for two bins in $\cos(\Theta_{\eta'}^{\mathrm{CMS}})$ in the 1450 energy bin. This limits any possible beam asymmetry determination to a forward/backwards asymmetry in this lowest energy bin, where the nodal structure observed by GRAAL is most prominent, see figure 2.4.

The poor $\cos(\Theta_{\eta'}^{\mathrm{CMS}})$ resolution furthermore limits the precision with which the differential cross section can be determined over $\cos(\Theta_{\eta'}^{\mathrm{CMS}})$. For some larger bins there are significant differences between the two EtaMAID parametrizations within the bin, but averaged over the whole bin the difference is nearly zero and thus hard to detect. This makes distinguishing between the two EtaMAID parametrizations only really feasible for the backward angular bin in the 1450 energy bin, where the difference is large over the whole range of the bin.

A kinematic fit can not improve the resolution beyond the best available detector resolution [57]. Since the best angular resolution at threshold is given by the forward spectrometer and this is used to determine the η' polar angle, a kinematic fit will not improve the results. This also holds true for the photon beam energy resolution, which is solely determined through the Tagger. As a result the $\cos(\Theta_{\eta'}^{\mathrm{CMS}})$ resolution, which depends on the η' polar angle as well as the beam energy, can not be improved with a kinematic fit for the analysis presented in this work [57].

As mentioned before, the resolution of the energy of the initial photon plays an important role in the

$\cos(\Theta_{\eta'}^{\text{CMS}})$ resolution, which is demonstrated by the difference between the resolution shown in this work and the one achieved at A2MAMI [34]. As shown in subsection 4.2.1, A2MAMI has a similar angular resolution to BGOOD, but a much improved beam energy resolution.

Thus making use of the ARGUS detector, which provides a much better energy resolution than the tagger for the initial photons, see subsection 3.2.1, the $\cos(\Theta_{\eta'}^{\text{CMS}})$ resolution can be improved significantly. Thus it is advisebale to perform a detailed analysis using the ARGUS detector for the determination of the initial photon energy. This will improve the angular resolution and as such make it easier to see any difference between the two EtaMAID parametrizations as well as possibly detect the nodal structure seen in the beam asymmetry. Furthermore the smaller ARGUS energy bins will allow the determination of differential cross sections and possible the beam asymmetry even closer to threshold, where the observed effects in cross section and beam asymmetry are strongest.

Summary and outlook

In recent years quite a number of often narrow structures has been observed near thresholds in hadronic reactions. Notable examples are X, Y, Z mesons [24, 58, 59, 60] and P_c baryons in the c-quark sector [23], or the long established $\Lambda(1405)$ in the uds sector. Today many of them are assigned a tetra- or penta-quark, possibly a meson-meson or meson-baryon type molecule-like structure.

An unexpected result for the beam asymmetry was obtained at the GRAAL experiment [26], that may hint at another such narrow state, in this case directly at threshold in $\eta' p$ photoproduction. Bonn-Gatchina [35] and EtaMAID [34] partial-wave-analyses suggest a narrow resonance close to threshold. To date, this result has not been confirmed by other experiments.

The BGOOD experiment offers a unique setup to investigate this issue. It combines a high resolution forward spectrometer with a central calorimeter. This makes it ideally suited to explore the threshold region. Due to kinematic focusing, all protons of the $\eta' p$ final state lie within the spectrometer's acceptance for a $\Delta E = 18\,\text{MeV}$ energy interval above threshold.

The goal of this work was to perform an exploratory study on how to use the BGOOD experiment to verify or falsify the GRAAL beam asymmetry results based on precise cross section measurements and distinguish between different partial-wave analyses with and without a narrow resonance close to threshold [34, 54]. It could be shown, that the reaction $\gamma p \to \eta' p$ can be reconstructed with excellent statistics by reconstructing the proton in the forward spectrometer. The statistical uncertainties for the inclusive reaction, where the decay $\eta' \to X$ remains unobserved, are sufficiently small to distinguish between EtaMAID parametrizations, that do or do not include a narrow resonance close to threshold. While close to threshold all final state protons from $\gamma p \to \eta' p$ are found within the forward spectrometer's acceptance, this is not the case for the relevant background contributions, whose thresholds are far below the $\gamma p \to \eta' p$ threshold. As a result, when looking at the energy dependence of the number of protons in forward direction, the signal shows a peak like structure at threshold, while the background exhibits a more continuous behavior. In principle signal and background can be well separated.

The advantageous feature of kinematic focusing used for the threshold measurement is, that the whole $\cos(\Theta_{\eta'}^{\text{CMS}})$ range is accessible through the protons in the forward spectrometer. On the flip side, going from the laboratory frame to the center-of-mass frame blows up the angular bins and with it the uncertainties. Those for the lab-to-CMS transformation not only include the angular resolution of the forward spectrometer, but also the energy resolution of the Tagger. In the present analysis the resolution for $\cos(\Theta_{\eta'}^{\text{CMS}})$ only permits two $\cos(\Theta_{\eta'}^{\text{CMS}})$ bins for the threshold Tagger energy bin. As

demonstrated, this resolution can be improved by making use of the ARGUS detector, which improves the energy resolution of the Tagger in the region of interest.

The $\eta' p$ cross section exhibits sensitivity to a possible narrow resonance in the extreme angles. An important aspect of an accurate measurement is a good understanding of the relevant backgrounds. While an inclusive analysis provides the highest amount of statistics, it also contains the highest amount of background. By increasing the exclusiveness of the analysis, the background can be reduced at the cost of reduced statistics. In this work the extracted cross sections were compared to EtaMAID parametrizations for varying levels of exclusiveness in well measured $\cos(\Theta_{\eta'}^{\text{CMS}})$ bins.

It was shown, that for the inclusive reconstruction an improved background description is required to get an agreement with EtaMAID parametrizations within the statistical errors. The agreement improves for the semi-exclusive analyses $\eta' \to \pi^0 \pi^0 \eta$, where either the two π^0 or the η are reconstructed from their two photon decay and the other particles are identified via the missing mass, leading to a strong reduction of the background. There is a good agreement for the totally exclusive reconstruction $\eta' \to \gamma\gamma$. This proves, that with a good understanding or a sufficient reduction of the background, the methods outlined in this work can correctly reproduce differential cross sections for $\gamma p \to \eta' p$.

Based on the current data basis, the statistical errors for the more exclusive reconstructions are too large to distinguish between EtaMAID parametrizations. However, with a reasonable amount of additional data and some modifications in the analysis, the statistical errors for the semi-inclusive $\eta' \to \pi^0 \pi^0 \eta$ reconstruction will become sufficiently small. This will be difficult to achieve for the fully exclusive $\eta' \to \gamma\gamma$ channel.

It was further demonstrated that a possible background remaining after the exclusive $\eta' \to \gamma\gamma$ reconstruction is of the order of below $10\,\%$ at threshold. This is an important result regarding the GRAAL experiment, where the background could not be characterized. Such a background level is not enough to falsely produce the large beam asymmetry observed by GRAAL.

Regardless of the reconstruction method, based on the presently available data set a direct extraction of the beam asymmetry is not possible with sufficiently small statistical errors. This will remain subject to a significantly improved future data set.

Acknowledgements

Bibliography

[1]   J. Dalton, *A New System of Chemical Philosophy*, S. Russell, 1808 (cit. on p. 1).

[2]   E. Rutherford, *The Scattering of α and β Particles by Matter and the Structure of the Atom*,
      Phil. Mag. **ser. 6, vol. 21** (1911) 669 (cit. on p. 1).

[3]   E. Rutherford, *Collision of a Particle with Light Atoms. IV. An annomalous Effect in Nitrogen*,
      Phil. Mag. **ser. 6, vol. 37** (1919) 581 (cit. on p. 1).

[4]   J. Chadwick, *Possible Existence of a Neutron*, Nature **129** (1932) 312 (cit. on p. 1).

[5]   S. Neddermeyer and C. D. Anderson, *Note on the Nature of Cosmic-Ray Particles*,
      PRJ **51** (1937) 884 (cit. on p. 1).

[6]   C. Lattes et al., *Processes involving charged mesons*, Nature **159** (1947) 694 (cit. on p. 1).

[7]   G. Rochester and C. Butler, *Evidence for the Existence of New Unstable Elementary Particles*,
      Nature **160** (1947) 855 (cit. on p. 1).

[8]   H. Anderson et al., *Total Cross Sections of Positive Pions in Hydrogen*, PRJ **85** (1952) 936
      (cit. on p. 1).

[9]   A. R. Erwin et al., *Evidence for a $\pi - \pi$ Resonance in the I = 1, J = 1 State*, PRL **6** (1961) 628
      (cit. on p. 1).

[10] B. C. Maglić et al., *Evidence for a T = 0 Three-Pion Resonance*, PRL **7** (1961) 178
      (cit. on p. 1).

[11] M. Gell-Mann, *The Eightfold Way: A Theory of Strong Interaction Symmetry*,
      Caltech Synchrotron Laboratory Report **CTSL-20** (1961) (cit. on p. 1).

[12] Y. Ne'eman, *Derivation of strong interactions from a gauge invariance*,
      Nucl. Phys. **26** (1961) 222 (cit. on p. 1).

[13] E. D. Bloom et al., *High-Energy Inelastic e-p Scattering at $6°$ and $10°$*, PRL **23** (1969) 930
      (cit. on p. 2).

[14] M. Breidenbach et al., *Observed Behavior of Highly Inelastic Electron-Proton Scattering*,
      PRL **23** (1969) 935 (cit. on p. 2).

[15] P.A. Zyla et al. (Particle Data Group), *The Review of Particle Physics*,
      Prog. Theor. Exp. Phys. **2020** (2020) 083C01, URL: http://pdg.lbl.gov
      (cit. on pp. 2, 5–7, 33, 54).

[16] PLUTO Collaboration, *Jet analysis of the $\Upsilon(9.46)$ decay into charged hadrons*,
      PLB **82** (1979) 449 (cit. on p. 2).

[17] UA1 Collaboration, *Experimental observation of isolated large transverse energy electrons
      with associated missing energy at $\sqrt{s}$ = 540 GeV*, PLB **122** (1983) 103 (cit. on p. 2).

[18]   The UA2 Collaboration, *Observation of single isolated electrons of high transverse momentum in events with missing transverse energy at the CERN $\bar{p}p$ collider*, PLB **122** (1983) 476 (cit. on p. 2).

[19]   UA1 Collaboration, *Experimental Observation of Lepton Pairs of Invariant Mass Around 95 GeV/c^2 at the CERN SPS Collider*, PLB **126** (1983) 398 (cit. on p. 2).

[20]   The UA2 Collaboration, *Evidence for $Z^0 \rightarrow e^+e^-$ at the CERN $\bar{p}p$ Collider*, PLB **129** (1983) 130 (cit. on p. 2).

[21]   The ATLAS Collaboration, *Observation of a new particle in the search for the Standard Model Higgs boson with the ATLAS detector at the LHC*, PLB **716** (2012) 1 (cit. on p. 2).

[22]   Cush, *Standard Model of Elementary Particles*, URL: https://en.wikipedia.org/wiki/Standard_Model (cit. on p. 3).

[23]   R. Aaij et al. (LHCb Collaboration), *Observation of $J/\psi\,p$ Resonances Consistent with Pentaquark States in $\Lambda_0^b \rightarrow J/\psi K^- p$ Decays*, PRL **115** (2015) 072001 (cit. on pp. 2, 75).

[24]   S.-K. Choi et al. (Belle Collaboration), *Observation of a Narrow Charmoniumlike State in Exclusive $B^\pm \rightarrow K^\pm \pi^+\pi^- J/\psi$ Decays*, PRL **91** (2003) 262001 (cit. on pp. 2, 75).

[25]   J. M. M. Hall et al., *Lattice QCD Evidence that the $\Lambda(1405)$ Resonance is an Antikaon-Nucleon Molecule*, PRL **114** (2015) 132002 (cit. on p. 3).

[26]   P. Levi Sandri et al., *First measurement of the Σ beam asymmetry in η' photoproduction off the proton near threshold*, EPJ A **51** (2015) 77 (cit. on pp. 3, 7, 9, 63, 70, 71, 75).

[27]   S. Alef et al., *The BGOOD experimental setup at ELSA*, EPJ A **56** (2020) 104 (cit. on pp. 4, 13–19, 21, 22, 27, 31, 40).

[28]   The CBELSA/TAPS Collaboration, *Double-polarization observable G in neutral-pion photoproduction off the proton*, EPJ A **53** (2017) 8 (cit. on p. 6).

[29]   V. Crede et al. (CBELSA/TAPS Collaboration), *Photoproduction of η and η' mesons off protons*, PRC **80** (2009) 055202 (cit. on pp. 7, 35).

[30]   M. Williams et al. (CLAS Collaboration), *Differential cross sections for the reactions $\gamma p \rightarrow p\eta$ and $\gamma p \rightarrow p\eta'$*, PRC **80** (2009) 045213 (cit. on p. 7).

[31]   V. L. Kashevarov et al., *Study of η and η' Photoproduction at MAMI*, PRL **118** (2017) 212001 (cit. on p. 7).

[32]   *MAID homepage*, URL: https://maid.kph.uni-mainz.de (cit. on p. 7).

[33]   P. Collins et al., *Photon beam asymmetry Σ for η and η' photoproduction from the proton*, PLB **771** (2017) 213 (cit. on pp. 7, 9).

[34]   L. Tiator et al., *Eta and etaprime photoproduction on the nucleon with the isobar model EtaMAID2018*, EPJ A **54** (2018) 210 (cit. on pp. 7, 8, 10, 11, 37, 44, 51, 57, 63, 66, 67, 73, 75).

[35] A. Anisovich et al., *Proton-η′ interactions at threshold*, PLB **785** (2018) 626 (cit. on pp. 7, 9, 11, 75).

[36] W. Hillert, *The Bonn Electron Stretcher Accelerator ELSA: Past and future*, EPJ A **28** (2006) 139 (cit. on p. 13).

[37] O. Freyermuth, *Studies of ω Photoproduction off Proton at the BGO-OD Experiment*, Universität Bonn, 2017 (cit. on p. 14).

[38] A. Bella, *Linearly polarised photon beams at the BGO-OD experiment at ELSA*, Universität Bonn, 2016 (cit. on p. 15).

[39] C. Schmidt, A. Suele, U. Thoma et al., *Extended Pluggable Objectoriented ROOT(ified) Analysis for the CBELSA/TAPS experiment*, (2011) (cit. on pp. 21, 22).

[40] R. Brun and F. Rademakers, *ROOT - An object oriented data analysis framework*, NIM A **389** (1997) 81 (cit. on pp. 21, 24).

[41] *CBELSA/TAPS at ELSA experiment homepage*, URL: https://www.cb.uni-bonn.de (cit. on p. 22).

[42] S. Agostinelli et al., *Geant4 - a simulation toolkit*, NIM A **506** (2003) 250 (cit. on p. 22).

[43] C. Wu et al., *Photoproduction of ρ^0-mesons and Δ-baryons in the reaction $\gamma p \to p\pi^+\pi^-$ at energies up to $\sqrt{s}$ = 2.6 GeV*, EPJ A **23** (2005) 317 (cit. on p. 35).

[44] J. Ballam et al., *Bubble Chamber Study of Photoproduction by 2.8- and 4.7-GeV Polarized Photons. 1. Cross-Section Determinations and Production of ρ^0 and Δ^{++} in the Reaction $\gamma p \to p\pi^+\pi^-$*, PRD **5** (1972) 545 (cit. on p. 35).

[45] The Crystal Ball at MAMI, TAPS, and A2 Collaborations, *Photoproduction of $\pi^0\eta$ on protons and the $\Delta(1700)D_{33}$ resonance*, EPJ A **42** (2009) 141 (cit. on p. 35).

[46] M. Williams et al. (CLAS Collaboration), *Differential cross sections and spin density matrix elements for the reaction $\gamma p \to p\omega$*, PRC **80** (2009) 065208 (cit. on p. 35).

[47] A. Cisek, W. Schäfer, A. Szczurek, *Exclusive photoproduction of ϕ meson in $\gamma p \to \phi p$ and $pp \to p\phi p$ reactions*, PLB **690** (2010) 168 (cit. on p. 35).

[48] SAPHIR Collaboration, *Measurement of $\gamma p \to K^0\Sigma^+$ at photon energies up to 1.55 GeV*, PLB **464** (1999) 331 (cit. on p. 35).

[49] K.-H. Glander et al., *Measurement of $\gamma p \to K^+\Lambda$ and $\gamma p \to K^+\Sigma^0$ at photon energies up to 2.6 GeV*, EPJ A **19** (2004) 251 (cit. on p. 35).

[50] M. Niiyama et al., *Photoproduction of $\Lambda(1405)$ and $\Sigma^0(1385)$ on the proton at E_γ = 1.5 − 2.4 GeV*, PRC **78** (2008) 035202 (cit. on p. 35).

[51] K. Moriya et al. (CLAS Collaboration),
Differential photoproduction cross sections of the Σ^0(1385), Λ(1405), and Λ(1520),
PRC **88** (2013) 045201 (cit. on p. 35).

[52] G. Scheluchin, *Private communication*, (2020) (cit. on p. 35).

[53] S. Alef et al., *$K^+\Lambda$ photoproduction at forward angles and low momentum transfer*,
EPJ A **57** (2021) 80 (cit. on p. 36).

[54] V. Kashevarov, *Private communication*, (2020) (cit. on pp. 37, 44, 51, 57, 63, 66, 67, 75).

[55] S. Prakhov et al. (Crystal Ball Collaboration at MAMI and A2 Collaboration),
Measurement of the slope parameter α for the $\eta \to 3\pi^0$ decay with the Crystal Ball detector at the Mainz Microtron (MAMI-C), PRC **79** (2009) 035204 (cit. on p. 40).

[56] P. Adlarson et al. (A2 Collaboration at MAMI),
Measurement of π^0 photoproduction on the proton at MAMI C, PRC **92** (2015) 024617
(cit. on p. 40).

[57] G. Scheluchin, *Private communication*, (2021) (cit. on p. 72).

[58] B. Aubert et al. (BABAR Collaboration),
Observation of a Broad Structure in the $\pi^+\pi^- J/\psi$ Mass Spectrum around $4.26\,\mathrm{GeV}/\mathrm{c}^2$,
PRL **95** (2005) 142001 (cit. on p. 75).

[59] M. Ablikim et al. (BESIII Collaboration),
Observation of a Charged Charmoniumlike Structure in $e^+e^- \to \pi^+\pi^- J/\psi$ at $\sqrt{s} = 4.26\,\mathrm{GeV}$,
PRL **110** (2013) 252001 (cit. on p. 75).

[60] Z. Q. Liu et al. (Belle Collaboration),
Study of $e^+e^- \to \pi^+\pi^- J/\psi$ and Observation of a Charged Charmoniumlike State at Belle,
PRL **110** (2013) 252002 (cit. on p. 75).

Appendix

A.1 Fits for $\eta' \to X$

All fits for $\eta' \to X$: the shaded areas indicate the two sidebands. The respective $\cos(\Theta_{\eta'}^{CMS})$ bin is given in the title of each plot, while the legend is shown in the top left plot.
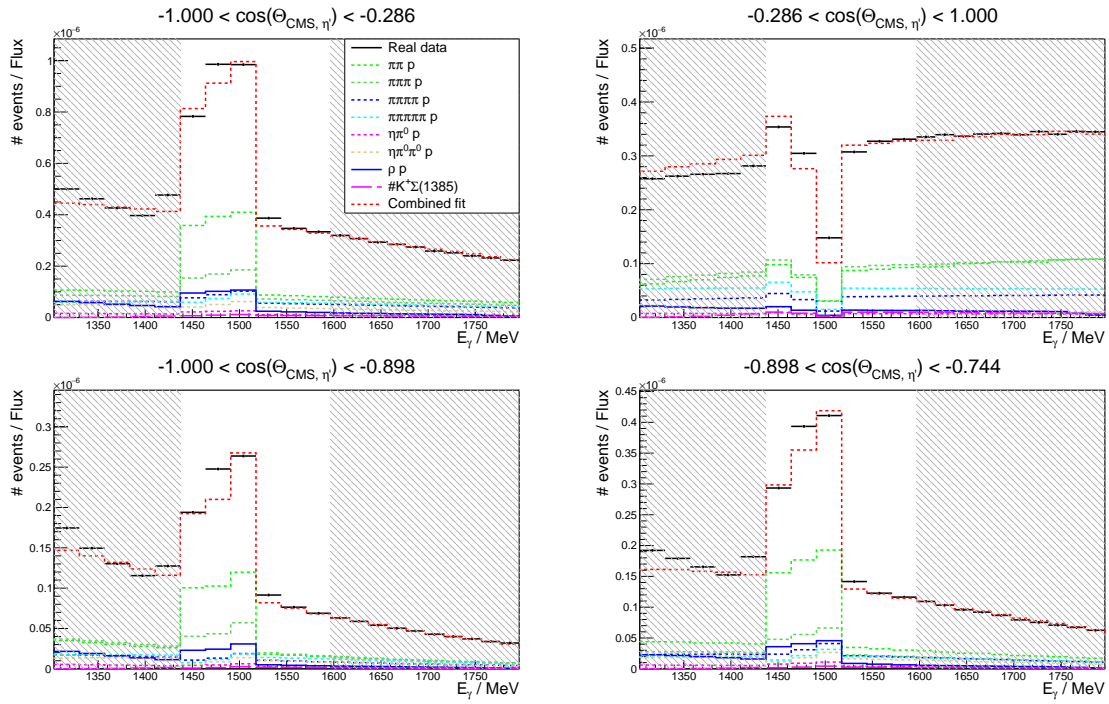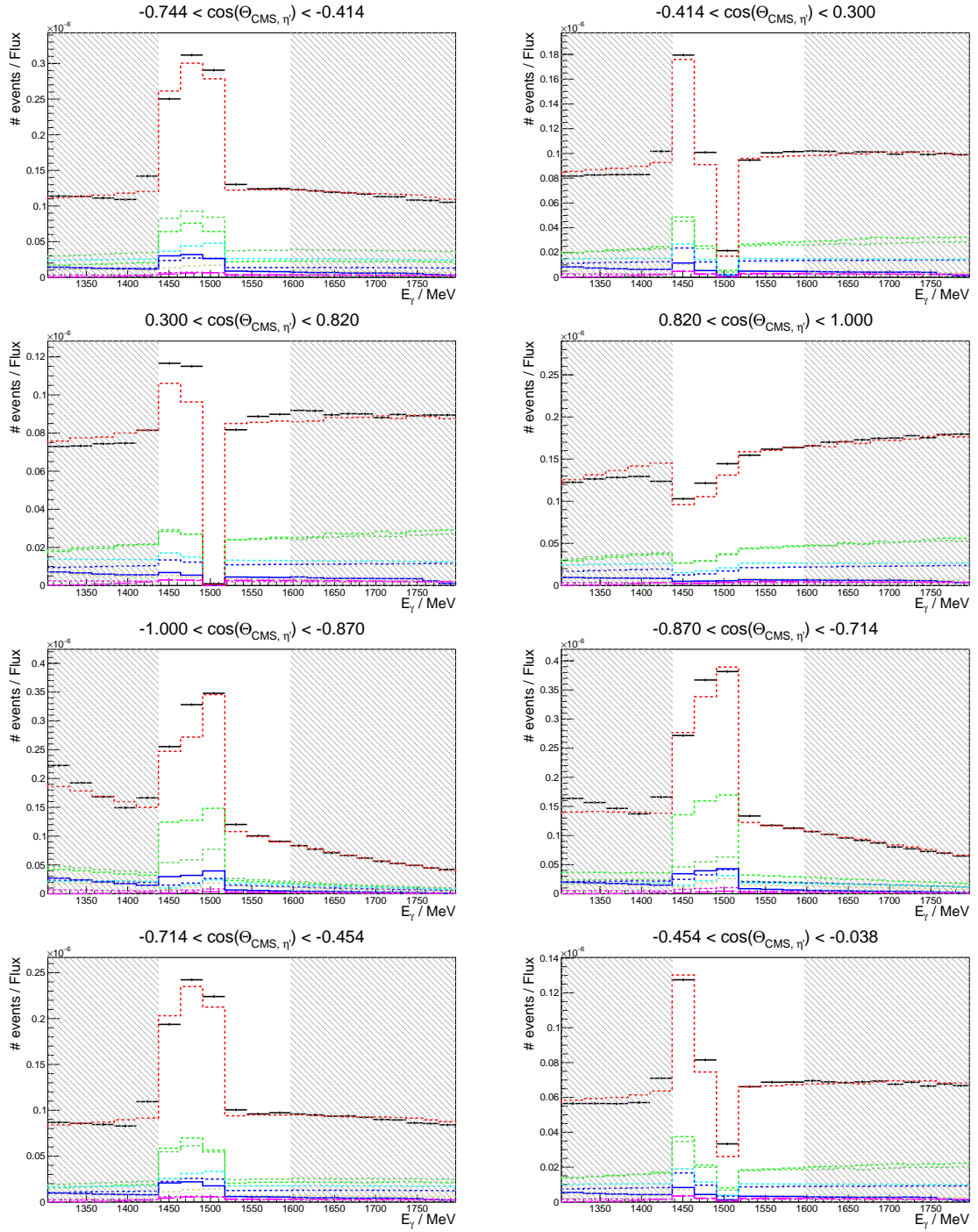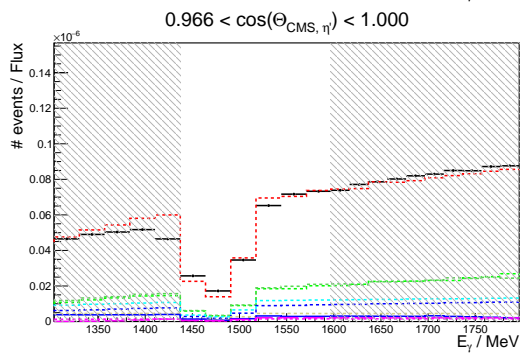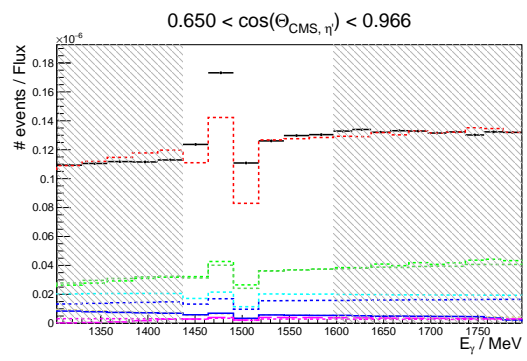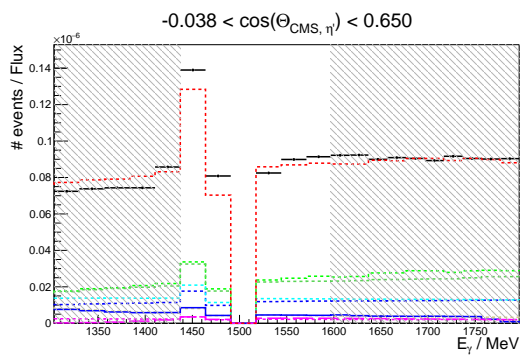
A.2 Fits for $\eta' \rightarrow (\pi^0\pi^0)\eta$

All fits for $\eta' \rightarrow (\pi^0\pi^0)\eta$: the shaded areas indicate the two sidebands. The respective $\cos(\Theta_{\eta'}^{CMS})$ bin is given in the title of each plot, while the legend is shown in the top left plot.
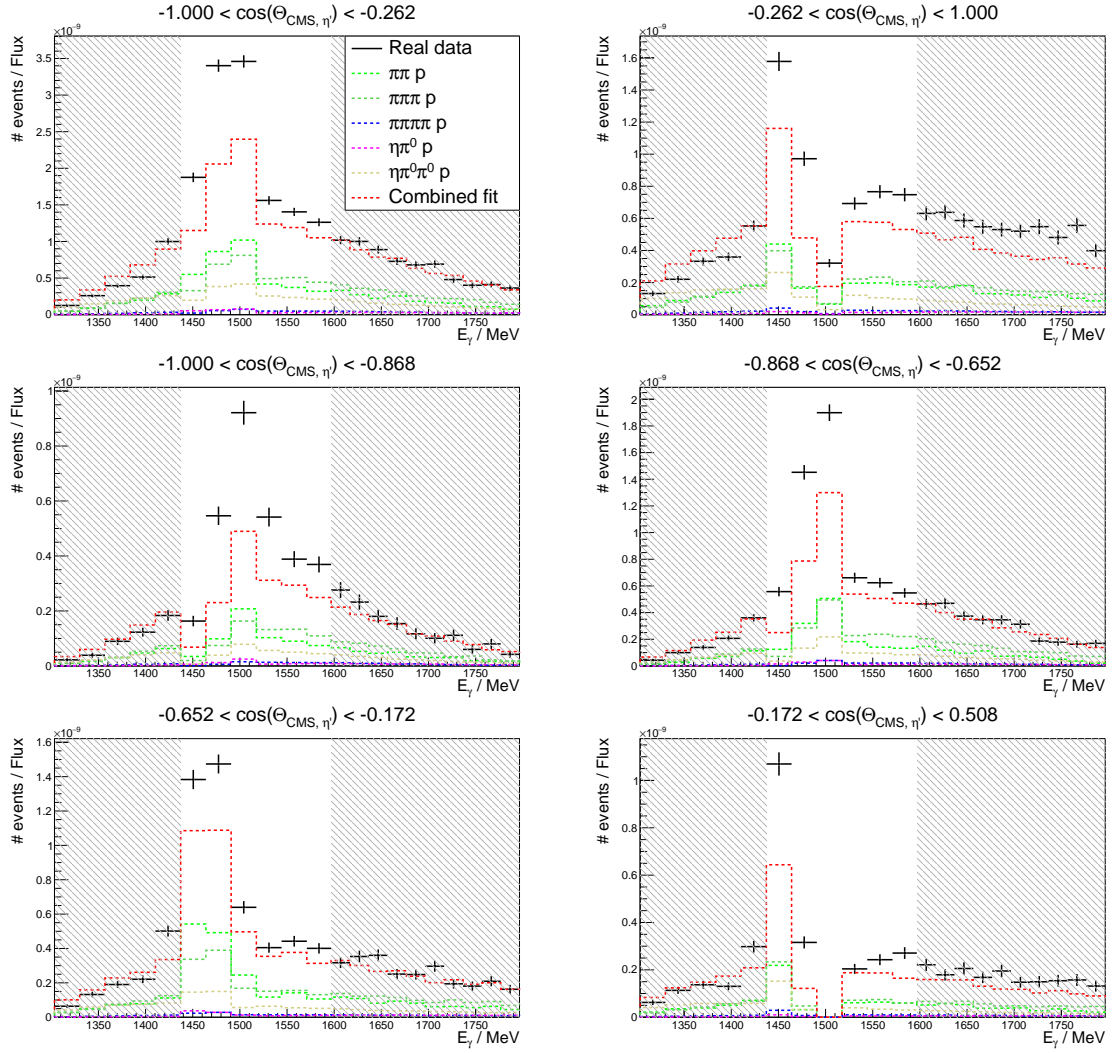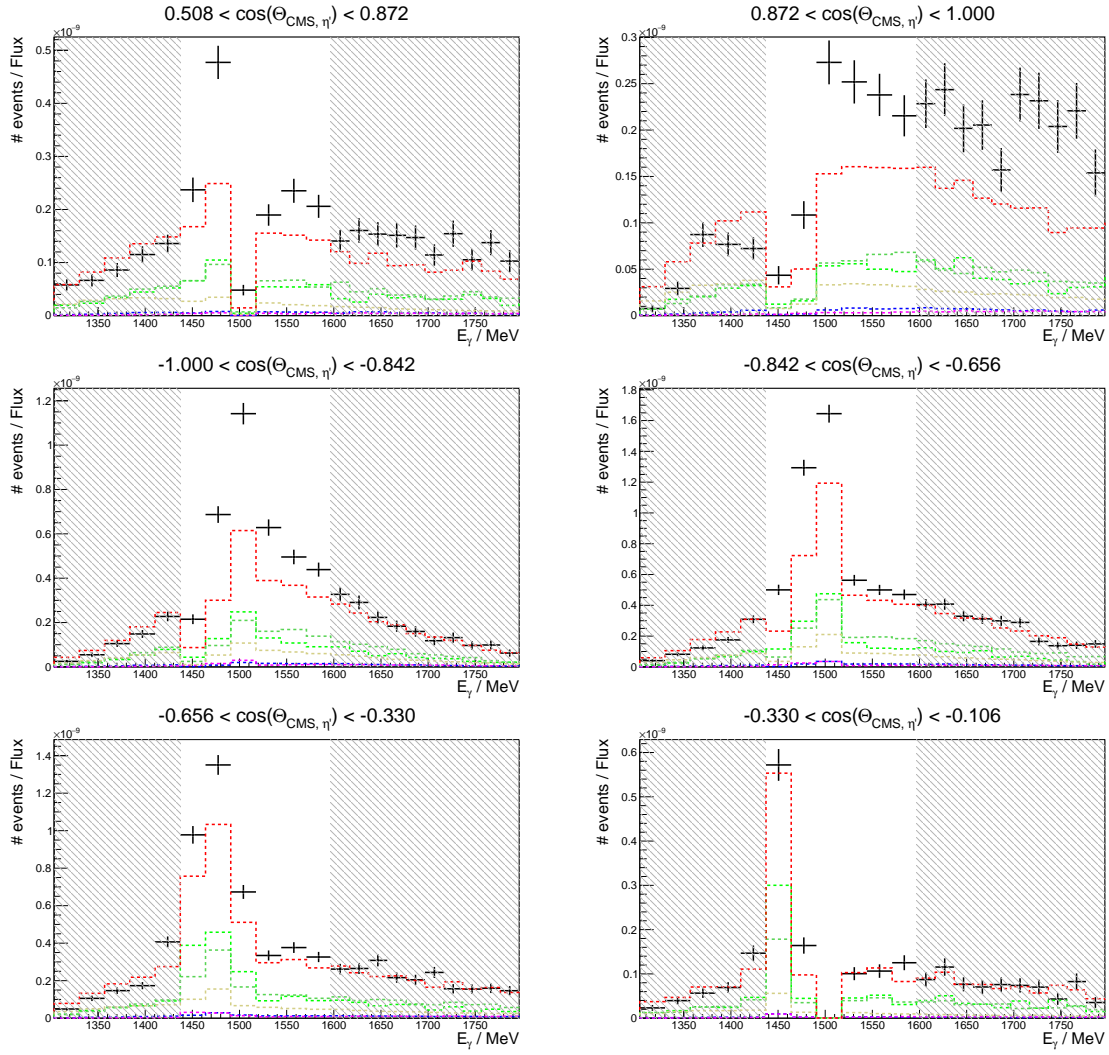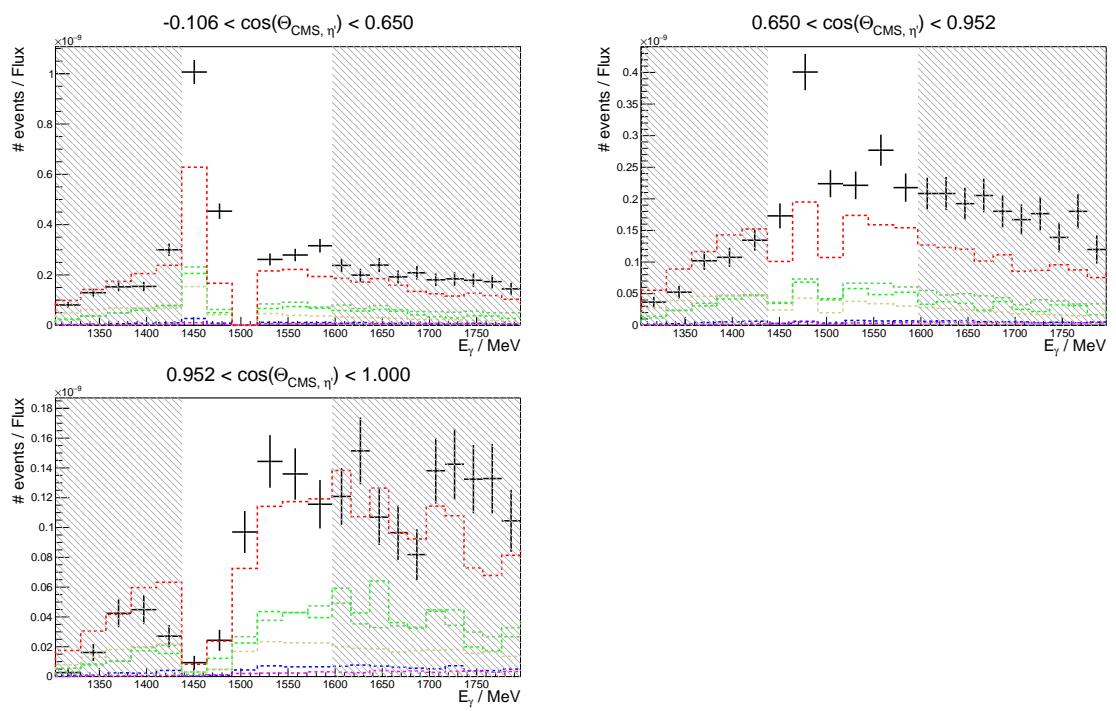
A.3 Fits for $\eta' \rightarrow \pi^0\pi^0(\eta)$

All fits for $\eta' \rightarrow \pi^0\pi^0(\eta)$: the shaded areas indicate the two sidebands. The respective $\cos(\Theta_{\eta'}^{CMS})$ bin is given in the title of each plot, while the legend is shown in the top left plot.

89
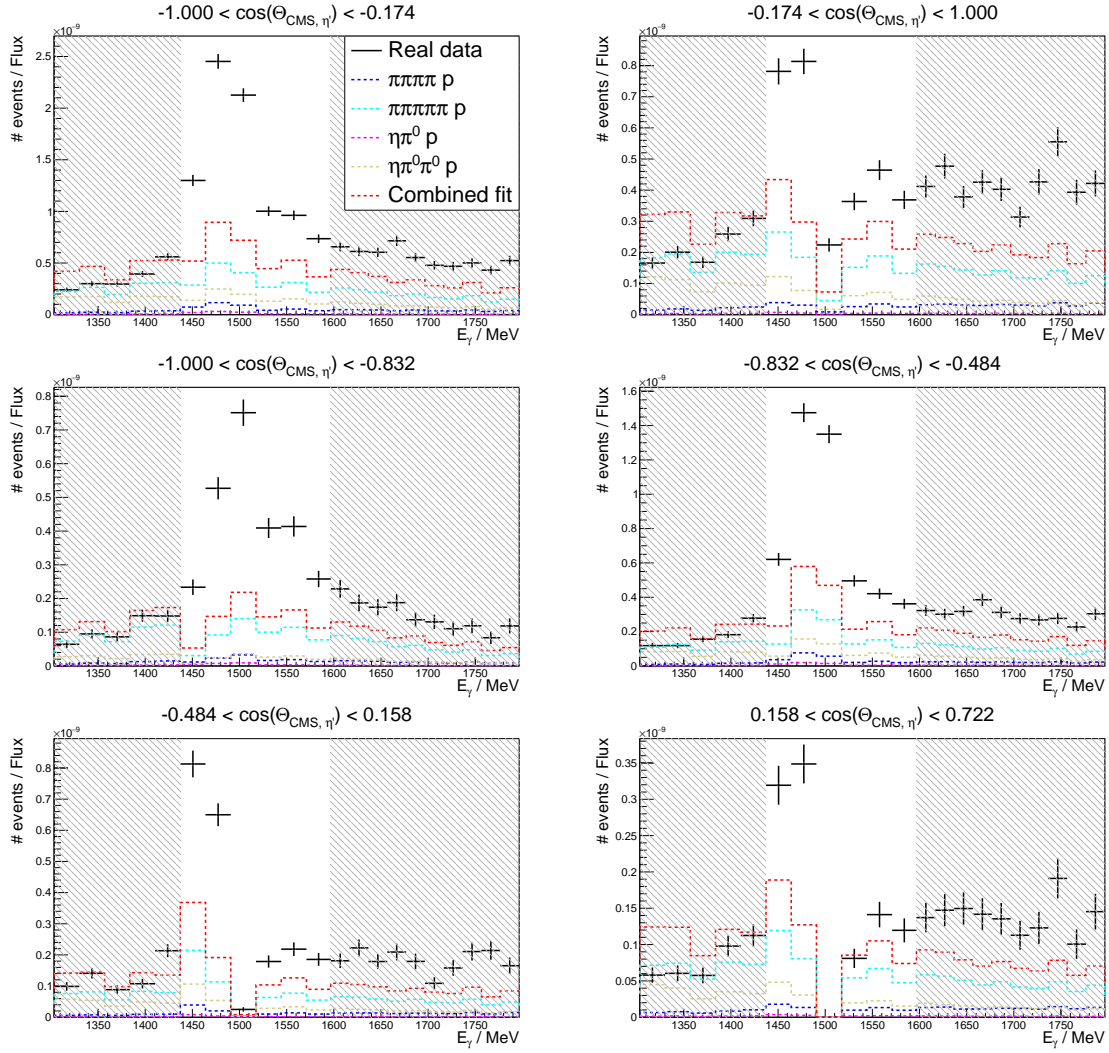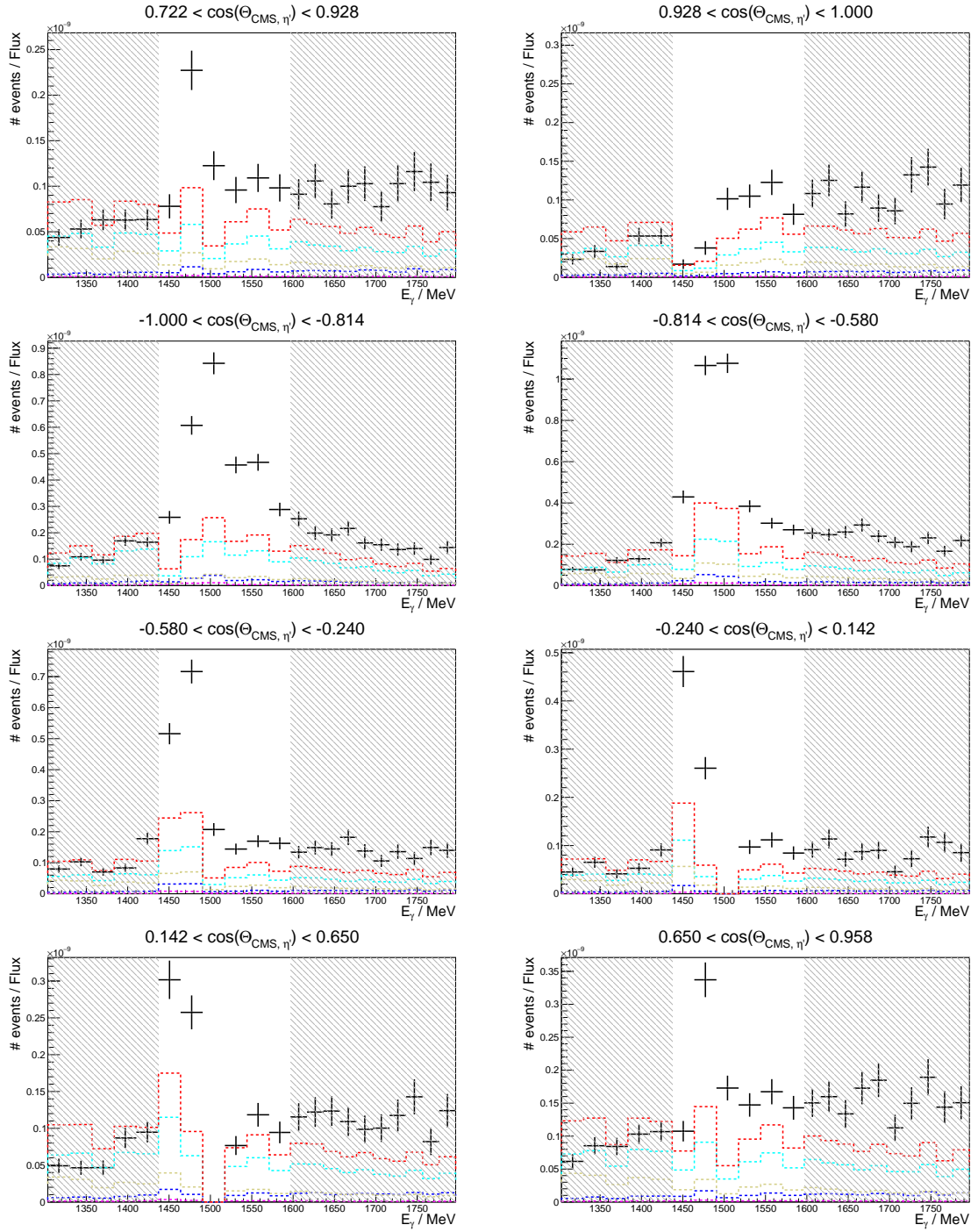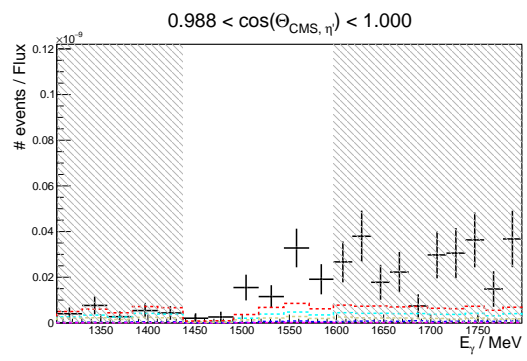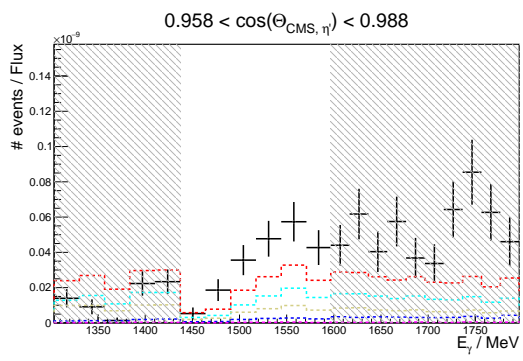
A.4 Fits for $\eta' \to \gamma\gamma$

All fits for $\eta' \to \gamma\gamma$: the shaded areas indicate the two sidebands. The respective $\cos(\Theta_{\eta'}^{CMS})$ bin is given in the title of each plot, while the legend is shown in the top left plot. The plot for the $-0.176 < \cos(\Theta_{\eta'}^{CMS}) < -0.144$ range is mostly empty, since the bin is so narrow.

List of Figures

List of Tables